DYNAMICAL SYSTEMS ANALYSIS OF PATTERNING AND ROBUSTNESS OF BURSTS IN NEURONAL MODELS

by

Sushmita Rose John

B.S., Mathematics, University of Delhi, 2015

M.S., Mathematics, Indian Institute of Technology Madras, 2017

Submitted to the Graduate Faculty of

the Dietrich School of Arts and Sciences in partial fulfillment

of the requirements for the degree of

Doctor of Philosophy

University of Pittsburgh

2023

UNIVERSITY OF PITTSBURGH

DIETRICH SCHOOL OF ARTS AND SCIENCES

This dissertation was presented

by

Sushmita Rose John

It was defended on

July 25th 2023

and approved by

Jonathan E. Rubin, Department of Mathematics

G. Bard Ermentrout, Department of Mathematics

David Swigon, Department of Mathematics

Victor V. Matveev, Department of Mathematics, New Jersey Institute of Technology

DYNAMICAL SYSTEMS ANALYSIS OF PATTERNING AND ROBUSTNESS OF BURSTS IN NEURONAL MODELS

Sushmita Rose John, PhD

University of Pittsburgh, 2023

Neurons in the brain are known to exhibit diverse bursting patterns. In this work, which combines three projects, we develop and analyze computational models to study various bursting activity displayed by respiratory neurons within the mammalian brainstem. In the first project, we examine minimal mathematical models that exhibit square wave bursting (SW) and analyze the transition of SW to other activity patterns due to parameter modifications. In particular, using these models, we analyze the robustness of SW with respect to the timescale associated with the conductance of a fast inward current. In the next project, we develop models that exhibit the "ramping" bursting pattern observed in the activity traces of neurons within the pre-Bötzinger Complex. Furthermore, we propose two mechanisms that help control the amplitude and frequency of spikes within the burst to obtain the desired ramping dynamics. In the final project, we explore the dynamics of Kölliker-Fuse nucleus (KF) which plays a role in the development of breathing abnormalities associated with Rett syndrome (RTT). We present reduced computational models of the respiratory core neurons along with the KF unit that simulate normal as well as RTT-like breathing patterns. These models provide a general framework for understanding KF dynamics and potential network interactions.

Table of Contents

List of Tables

List of Figures

Preface

First and foremost, I would like to express my heartfelt gratitude to my advisor, Dr. Jonathan Rubin for his guidance throughout my PhD journey. This thesis would not have been possible without your expertise and advice, and I am truly grateful to have had you as my advisor.

I would also like to thank my committee members, Dr. Bard Ermentrout, Dr. David Swigon, and Dr. Victor Matveev, for their valuable feedback and advice. I am also grateful to all my collaborators, Dr. Hinke Osinga, Dr. Bernd Krauskopf, Dr. William Barnett, Dr. Yaroslav Molkov, Dr. Daniel Zoccal, Dr. Ana Abdala, and Dr. Ryan Phillips, for their assistance and support on my projects, which have greatly contributed to the quality of this work.

Lastly, I would like to thank my parents, my sister and all my friends here in Pittsburgh for their unwavering love, support and encouragement. I really enjoyed this journey, and it is because of all of you. Thank you!

1.0 Introduction

1.1 Overview

Bursting is an activity pattern exhibited by neurons, including respiratory neurons, where discrete groups of spikes are fired with periods of silence in between. Mathematical models for respiratory neurons, which exhibit bursting and other spiking patterns, include components that change at different timescales. For instance, in the Hodgkin-Huxley model [41] that describes the spike generation in the squid giant axon, the transient sodium current activates rapidly and inactivates relatively slowly, while the persistent potassium current also activates slowly. Another example is the Butera model, introduced in [18], which exhibits bursting. In this model, the inactivation variable associated with persistent sodium current evolves at a significantly slower timescale compared to the other variables in the model. These models are referred to as multiple-timescale systems. This thesis is a combination of three projects based on multiple-timescale models for bursting respiratory neurons.

Most of the analysis done in this work is based on geometric singular perturbation theory (GSPT). In the next section, GSPT is explained briefly. The neurons that make up the respiratory core - Post-inspiratory (post-I), Pre-inspiratory (pre-I), augmenting expiratory (aug-E) and early-inspiratory (early-I) neurons and their network interactions are also described in this chapter.

In second chapter, we study square-wave bursting which is an activity pattern common to a variety of neuronal and endocrine cell models that has been linked to central pattern generation for respiration and other physiological functions [18, 85]. We introduce four popular reduced mathematical models for square wave bursting (SW) and analyze the effect of adding a slow inactivation gate to the fast inward current on the robustness of the bursting pattern. The second chapter and some parts of the introduction and conclusion is based on the published work : John, S. R., Krauskopf, B., Osinga, H. M., & Rubin, J. E. (2023). Slow negative feedback enhances robustness of square-wave bursting. Journal of computational neuroscience, 51(2), 239–261. https://doi.org/10.1007/s10827-023-00846-y

In the third chapter, we extend our previous work to ramping burst pattern observed in neurons in the pre-Bötzinger Complex (pre-BötC) in the brain stem. The ramping bursting pattern, which starts as slow oscillations, gradually increases in both spike frequency and amplitude as the burst progresses. Most of the current mathematical models for pre-BötC neurons do not exhibit the ramping dynamics. In this project, we explore the concept that either changing the spike height or adjusting the strength of hyperpolarization across successive spikes in the burst can help shape the burst and exhibit ramping dynamics. We present two phenomenological models developed by Dr. Ryan Phillips, Seattle Children's Research Institute, to analyze these concepts. Furthermore, we modify an exiting bursting model with an additional slow inactivation gate associated with fast inward sodium current and show that it produces ramping dynamics.

Kölliker-Fuse nucleus (KF), a part of the parabrachial complex, is involved in regulating normal breathing and controlling active abdominal expiration during increased ventilation [2, 20, 45]. In the fourth chapter, we utilize computational models for the respiratory core neurons along with KF unit to explore different dynamical regimes of KF activity and their compatibility with experimental observations. By analyzing different model configurations, the study identifies inhibitory inputs to the KF that lead to respiratory patterns associated with Rett syndrome (RTT) in which the expiratory phase duration is longer than normal and proposes potential KF local circuit organizations. Two models with different baseline KF activity are presented that simulate both normal breathing and RTT-like breathing patterns. These models provide plausible hypotheses and specific predictions for future experimental investigations, offering a general framework for understanding KF dynamics and potential network interactions. The fourth chapter and some parts of the introduction and conclusion is based on the work submitted to The Journal of Physiology : John, S., Barnett, W., Abdala, A., Zoccal, D., Rubin, J., & Molkov, Y. (2023). The role of Kölliker-Fuse nucleus in breathing variability. bioRxiv : the preprint server for biology, 2023.06.15.545086. https://doi.org/10.1101/2023.06.15.545086

1.2 Multi-timescale Systems

In its simplest form, geometric singular perturbation theory (GSPT) [46, 94] assumes that a general model is defined in terms of an explicit fast-slow decomposition of the form

$$\begin{cases} x' &= f(x,y,\epsilon), \\ y' &= \epsilon\, g(x,y,\epsilon), \end{cases} \tag{1}$$

where $0 < \epsilon \ll 1$ is a small parameter, so that the fast variable is $x \in \mathbb{R}^m$ and the slow variable is $y \in \mathbb{R}^n$. In the limit $\epsilon \to 0$, system (1) reduces to a lower-dimensional, so-called fast subsystem

$$\begin{cases} x' &= f(x,y,0) \\ y' &= 0 \end{cases} \tag{2}$$

where the slow variable y plays the role of a constant parameter vector. This system helps us analyze the fast timescale dynamics.

The equilibria of the fast subsystem (2) form a manifold $\mathcal{C}$ in (x,y)-space,

$$\mathcal{C} = \{(x,y) \in \mathbb{R}^m \times \mathbb{R}^n \;\mid\; f(x,y,0) = 0\},$$

which is called the critical manifold of system (1).

Re-scaling the system (1) to the slower timescale by setting $\tau = \epsilon t$, gives the following model :

$$\begin{cases} \epsilon \dot{x} &= f(x,y,\epsilon), \\ \dot{y} &= g(x,y,\epsilon), \end{cases} \tag{3}$$

where $\dot{x}$ and $\dot{y}$ denotes differentiation with respect to slower timescale τ. This model is equivalent to (1). However, in the limit $\epsilon \to 0$, system (3) reduces to a lower-dimensional, so-called slow subsystem

$$\begin{cases} 0 &= f(x,y,0), \\ \dot{y} &= g(x,y,0), \end{cases} \tag{4}$$

The fast and slow subsystems together describes the singular limit $\epsilon \to 0$ solutions of (1). The fast subsystem (2) describes the fast timescale dynamics of x and how the solution

moves from one stable branch of $\mathcal{C}$ to another while y remains constant. Assuming $\mathcal{C}$ is either Z-shaped or S-shaped with respect to x, parameterized by y, every branch of $\mathcal{C}$ can be expressed as $x = x(y)$. This simplifies (4) to

$$\begin{cases} 0 &= f(x, y, 0), \\ \dot{y} &= g(x(y), y, 0), \end{cases} \tag{5}$$

and gives the flow of y on the stable branch of $\mathcal{C}$. Hence, the slow subsystem (5) describes the slow dynamics of y, once the solution is at a stable branch of the critical manifold $\mathcal{C}$ with $g(x, y, 0) = 0$.

Once we understand the solution of the fast (2) and slow subsystems (4), Fenichel theory [46, 94, 31] helps us to understand the solution of (1). If the eigenvalues of the derivative of f evaluated at $\mathcal{C}$ (or an invariant subset of $\mathcal{C}$) have non-zero real parts, then Fenichel theory tells us that the critical manifold $\mathcal{C}$ perturbs to a locally invariant manifold $\mathcal{C}_\epsilon$ for ϵ small. Also, the flow along $\mathcal{C}_\epsilon$ is an ϵ perturbation of flow along the critical manifold $\mathcal{C}$. More details can be found at [46, 94, 31].

In the following chapters, we use GSPT [46, 94] to analyze different bursting patterns. We assume that $\mathcal{C}$ is either Z-shaped or S-shaped with respect to the component of x that represents voltage v. This means that $\mathcal{C}$ has (at least) three co-existing equilibrium branches, parameterized by y. Ordered with respect to their corresponding v-components, we refer to these branches as the lower (silent) branch, the middle branch, and the upper (active) branch of $\mathcal{C}$. Bursting patterns are classified depending on the bifurcations that initiate and terminate the oscillatory or active phase of the burst [69]. We study two particular bursting patterns in chapter 2. The first one is called square wave bursting (SW) or fold-homoclinic bursting (Figure 3A) since the oscillations begin once the trajectory reaches a fold bifurcation of the fast subsystem (2) with respect to the slow variable y, and the oscillations terminate after hitting the homoclinic curve. The second bursting pattern we work with is called the pseudo plateau bursting (PP) or fold-subHopf bursting. The oscillations, in this case, ends after the trajectory hits a subcritical Andronov–Hopf bifurcation. Since the Hopf bifurcation is subcritcal, there are no stable periodic orbits along the active branch of the v-nullcline. Instead, we have a branch of stable focus which cause the trajectory to spiral leading to small

amplitude spikes in the burst pattern. The trajectory also spirals outwards after hitting the subcritical Andronov–Hopf bifurcation leading to a small delay before it jumps down to the silent branch leading to the PP bursting pattern shown in chapter 2 (Figure 3B).

If a model exhibits SW or PP bursting, certain features must be present: firstly, that system (2) has a (lower) saddle-node bifurcation at some critical parameter value y_{LSN}, at which the lower and middle branches of $\mathcal{C}$ meet; and secondly, that system (2) has an Andronov–Hopf bifurcation along the upper branch of $\mathcal{C}$, which gives rise to a family $\mathcal{P}$ of periodic orbits of (2) parameterized by y. Note that this second requirement implies $m \geq 2$; that is, the fast variable x must be at least two-dimensional.

Crucially, this Andronov–Hopf bifurcation is subcritical in the PP case, which means that the orbits of $\mathcal{P}$ are unstable and, hence, system (2) does not produce stable spiking activity for initial conditions along the upper (active) branch of $\mathcal{C}$. For SW bursting, on the other hand, there exists a stable family of periodic orbits, together with a mechanism that induces a transition from the active phase to the silent phase. The originally described and most commonly considered form of SW bursting involves a supercritical Andronov–Hopf bifurcation for (2) on the upper (active) branch of $\mathcal{C}$ and a homoclinic bifurcation at which the family $\mathcal{P}$ of stable periodic orbits collides with a saddle equilibrium on the middle branch of $\mathcal{C}$ [69].

While the presence and order of specific bifurcations in the fast subsystem (2) help to predict the burst pattern exhibited by the full model, the burst pattern also depends on the relative location of the nullcline associated with the slow variable. In order for models to exhibit SW bursting, for example, it is necessary, although not sufficient, for the slow nullcline to intersect the middle branch of $\mathcal{C}$ at an equilibrium point below the homoclinic bifurcation; in particular, the full system must have a steady state that is of saddle type. We make sure this is the case over a sufficiently large range of parameters for all models considered in the second chapter.

The dynamic spike height model presented in third chapter that exhibits bursting pattern in which the spike frequency as well as the strength of hyperpolarization between spikes increases during the burst. We show that this model has components varying at three different timescales. To analyze the further, we modify the standard GSPT method described

in this section to adapt to three timescales. We divide the model into fast, intermediate and slow subsystems. We can now use the standard GSPT theory to analyze the fast-intermediate system fixing the slow variable at different values. The slow subsystem dynamics can be further analyzed using methods such averaging theory and bifurcation analysis.

1.3 Respiratory rhythm generation

Eupnea, or normal, unlabored breathing in mammals, can be considered to be a rhythmic sequence of three phases : inspiration, early expiration and late expiration is generated by the respiratory central pattern generator (CPG) located in the brainstem. The core of the CPG consists of interconnected neurons within the pre-Bötzinger Complex (pre-BötC) and the Bötzinger Complex (BötC). The pre-inspiratory (pre-I) and early-inspiratory (early-I) neurons in the pre-BötC and the post-inspiratory (post-I) and augmenting expiratory (aug-E) neuronal populations in the BötC form the respiratory core in the brain. These populations can be distinguished by their firing pattern as well as the respiratory phase when they become active [78, 19, 47, 72].

The inspiratory phase of the rhythm is controlled by the pre-I and early-I neurons in pre-BötC while the expiratory phase is controlled primarily by the post-I and aug-E neuronal populations in BötC. The pre-I population starts firing before the start of inspiration and continues to fire throughout the inspiratory phase. The activity of this neuronal population peaks near the start of inspiratory phase. The early-I population starts firing at the onset of inspiration at high frequency and reduces throughout inspiration. The aug-E and post-I neuronal populations are active during the expiratory phase. More precisely, post-I units feature a surge of activity at the onset of expiration, followed by a gradual tailing off of activity. In contrast, aug-E units gradually ramp up their activity, in an augmenting pattern, over the course of expiration [47].

[79] developed a mathematical model to reproduce the respiratory rhythm showing the interconnections between all the different neuronal populations, located in different regions of the brainstem, involved in respiration. All the different neuronal population dynamics were

modeled by Hodgkin Huxley type equations. This model was reduced to the dynamics of the main four respiratory core populations in [72]. Later work [71] added the late-expiratory (late-E) neuronal population of the lateral parafacial region (pFL), which remains inactive during resting breathing ([16]) but becomes active during active expiration. The models for respiratory neurons presented in the fourth chapter are adapted from previous models ([72, 71, 95]). These models include the four respiratory core neuronal populations as well as a late-expiratory (late-E) population.

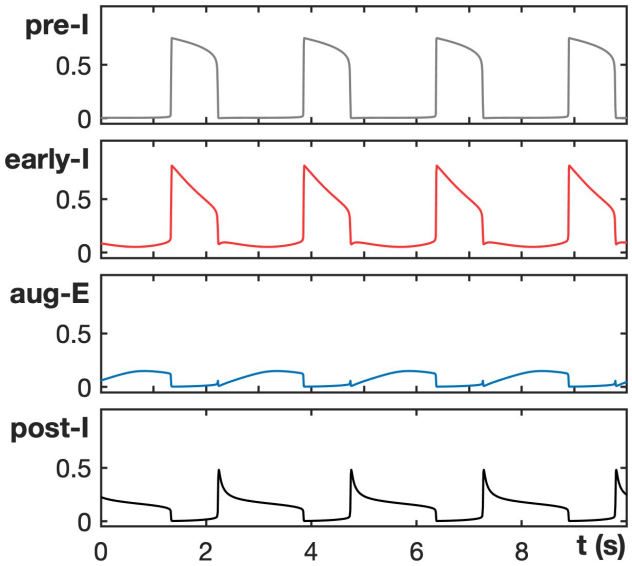

Figure 1: Normal respiratory rhythm. The integrated pre-I, early-I, aug-E and post-I output from the model introduced in [72]. The pre-I and early-I units are active during the inspiratory phase, while aug-E and post-I units are active during the expiratory phase. Notice that in this simplified model, the pre-I unit lacks the pre-inspiratory ramp, and therefore, it only activates at the onset of inspiration.

2.0 Slow negative feedback enhances robustness of square-wave bursting [1]

2.1 Introduction

In neuroscience, bursting refers to activity patterns in which a cell's membrane potential alternates repeatedly between two phases: an active phase featuring a succession of spikes separated by relatively short inter-spike intervals and/or a sustained depolarization, and a silent or quiescent phase of little or no spiking. It has long been recognized that bursting patterns are closely connected with bifurcations in an underlying dynamical system [69]. The original classification and analysis of bursting types relied on a fast-slow decomposition approach that falls within the realm of geometric singular perturbation theory [46, 23, 94]. Later work generalized the key idea of characterizing burst structure based on bifurcations associated with the transitions between active and silent phases [42] and classifying bursting patterns in terms of unfoldings of higher-codimension bifurcation points [13, 39, 48, 89]. In fact, these analyses embed bursting within a larger class of activity types that includes patterns such as relaxation oscillations (ROs; Figure 2A), which also feature abrupt transitions between phases yet lack the spikes that occur during the active phases of bursts [69, 14].

In this chapter, we focus on two specific bursting activity patterns often observed in neural and endocrine cell recordings: square-wave (SW) and pseudo-plateau (PP) bursting (Figure 2B,C), which are mathematically classified as fold-homoclinic and fold-sub-Hopf bursting, respectively [42]. These two bursting patterns stem from similar underlying bifurcation structures [88, 89]; however, in contrast to SW bursting, PP bursting does not produce reliable spiking activity, and often resembles an RO pattern (Figure 2A,C).

Even though certain models are often referred to as models for one activity pattern or another, the same model can exhibit many different activity patterns, including multiple types of bursting, as parameters are varied, as the unfolding approach to burst analysis recognizes. Indeed, some minimal models for SW bursting yield a transition to PP (and

[1] This chapter is based on published work :John, S. R., Krauskopf, B., Osinga, H. M., & Rubin, J. E. (2023). Slow negative feedback enhances robustness of square-wave bursting. Journal of computational neuroscience, 51(2), 239–261. https://doi.org/10.1007/s10827-023-00846-y

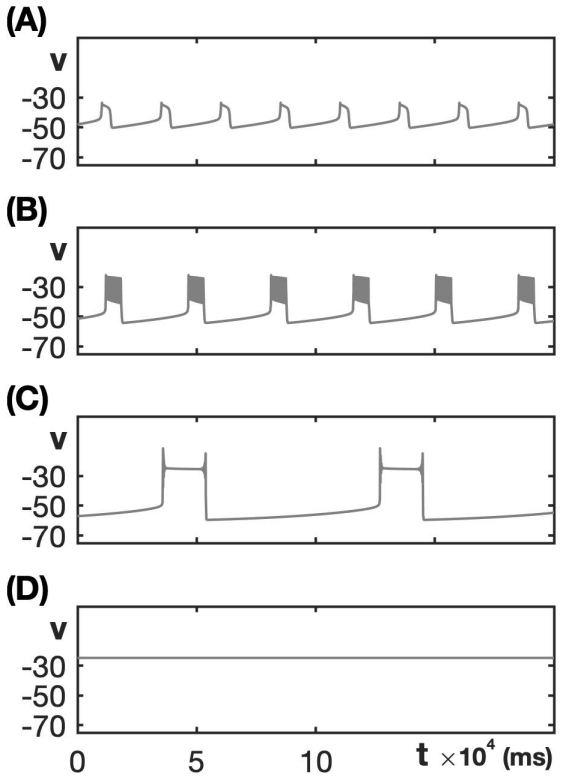

Figure 2: Non-spiking activity patterns.The voltages traces shown here are from the minimal Chay–Keizer model (10)–(11) with default parameter values. (A) Relaxation oscillations (RO) for $g_{ca} = 1.2$.(B) Square-wave (SW) bursting for $g_{ca} = 1.8$.(C) Pseudo-plateau (PP) bursting for $g_{ca} = 3.2$. Note that although each active phase features an initial spike and a terminal spike, no other significant spiking occurs. (D) Depolarization block resulting from a stable critical point at elevated voltage for $g_{ca} = 3.5$.

vice versa) under small changes in parameter values [84, 86, 85, 88, 89]. From a functional perspective, however, this effect may represent the emergence of a dysfunctional regime for a cell: the loss of spikes in the active phase associated with a transition from SW to PP bursting may result in a failure to release neurotransmitters or other signaling substances.

Since some cells are observed specifically to exhibit SW bursting, while others have been seen to produce both SW and PP patterns, we wondered if these differences could result from differences in the actual biophysical mechanisms expressed in these cells, rather than simply from observation of the dynamics within different parameter regimes. Indeed, spike production carries a significant energy cost [80, 76], which suggests that when the firing of spikes is observed, this behavior is likely to be of functional importance and we might expect mechanisms to be present that enhance the robustness of spiking across parameter modulations. Similarly, some bursting cells feature fast inward sodium currents while others express fast inward calcium currents; although these are often considered interchangeable from a dynamics perspective (e.g., [43]), which current is present may have implications for the robustness of bursting and spiking patterns that cells exhibit. The main motivation for this study is to understand what features promote the robustness of SW bursting – both to help explain the mechanisms underlying differences in observed activity across neuron types and to guide the development of future models designed to capture such data.

In this work, we investigate the utility of a specific biophysical mechanism that we have recognized as enhancing the robustness of SW bursting in computational models. Bursting models feature a voltage-dependent fast inward current that helps to sustain the active phase, because it provides a fast positive feedback to the membrane potential [43]. We explore the effect on the robustness of SW bursting of adding a slow, voltage-dependent negative feedback associated with this inward current, which is a feature of fast sodium currents in neurons of certain types [22, 57] and may also arise in fast calcium currents in some cases [26, 96].

To carry out this analysis, we consider four classical, low-dimensional SW bursting models in their original forms, as well as with adjustments either to include a slow inactivation gate as part of the fast inward current, or to modify the kinetics of an already-present inactivation gate. This collection of models was selected to allow for consideration of fast inward sodium and calcium currents with a variety of mathematical formulations. We show that,

over an appropriate range of the time constant for the respective inactivation gate, its inclusion broadens the range of maximal conductances g_{ca} or g_{na} of the fast inward current for which SW bursting — or a different form of spiking activity that can serve similar functional purposes in the context of a CPG (central pattern generator) circuit with inhibitory connections between populations [17, 73] — occurs. We also show that, outside of this optimal range of inactivation timescales, SW bursting loses robustness, and the models easily transition from SW to PP bursting and other non-spiking patterns, including ROs and depolarization block (Figure 2A,D), for which neurotransmitter release would be compromised.

The remainder of the chapter is organized as follows. We introduce the four different bursting models in Section 2.2.1 and show how GSPT is used to understand the various burst patterns exhibited by these models when g_{ca} or g_{na} is varied. In Section 2.2.2, we explain how we modify the models for our robustness analysis. The analysis of the robustness of SW bursting gained by including a slow, voltage-dependent negative feedback associated with the inward current follows in Section 2.3. The chapter concludes with a discussion in Section 2.4.

2.2 Preliminary Analysis

The geometric singular perturbation theory is briefly explained in section 1.2.

2.2.1 Models and Parameter-Dependence of Bursting Dynamics

As mentioned in the introduction, we select and study four different, low-dimensional SW bursting models with distinct formulations of the fast inward current. Each is presented in its original form and we discuss the parameter range for the maximal conductance of the fast inward current, g_{ca} or g_{na}, over which SW bursting occurs.

2.2.1.1 Generic Endocrine Model

[88] introduced a generic endocrine model in the literature that exhibits both SW and PP bursting over physiologically relevant parameter ranges. The model is a system of differential equations for the membrane potential v, the gating variable n of the K^+ channel, and the calcium concentration c in the cytosol. The equations take the form

$$\begin{cases} c_m v' &= -I_{Ca}(v) - I_K(v,n) \\ & \quad -I_{K(Ca)}(v,c), \\ n' &= (n_\infty(v) - n)/\tau_n, \\ c' &= -f_c\,(\alpha\, I_{Ca}(v) + k_p\, c), \end{cases} \tag{6}$$

for constants c_m, τ_n, f_c, α, and k_p. The expressions for the currents and steady state activation functions are given by:

$$\begin{aligned} I_{Ca}(v) &= g_{ca}\, m_\infty^2(v)\,(v - e_{ca}), \\ I_K(v,n) &= g_k\, n\,(v - e_k), \\ I_{K(Ca)}(v,c) &= g_{kca}\left(\frac{c^4}{c^4 + k_s^4}\right)(v - e_k), \\ m_\infty(v) &= (1 + e^{(v_m - v)/s_m})^{-1}, \\ n_\infty(v) &= (1 + e^{(v_n - v)/s_n})^{-1}. \end{aligned} \tag{7}$$

$I_{Ca}(v)$ in (7) is an approximation of a more complicated nonlinear expression related to the Goldman-Hodgkin-Katz equation [29]. We choose default parameter values as given in Table 1, for which the model exhibits the SW bursting pattern shown in Figure 3A. Indeed, non-dimensionalization (see the Appendix) shows that the three-dimensional system (6)–(7) readily separates into fast and slow equations, because v changes at a rate $R_v \approx 716$ that is faster than the rate $R_n \approx 33$ for n, which in turn, is significantly faster than the rate $R_c \approx 1.7$ for c. We consider v and n as two fast variables and c as one slow variable, so that system (6)–(7) has the lowest possible dimensions for SW bursting. This model can also be studied as a three-timescale system, with v having a fast timescale, n evolving at an intermediate timescale, and c being the slow variable. The model exhibits stable relaxation oscillations in the fast-intermediate subsystem for fixed c values, and the analysis

Table 1: Generic Endocrine Model (6)–(7): default parameter values.

c_m	0.00314159 nF	g_{ca}	0.81 nS
g_k	2.25 nS	g_{kca}	0.2 nS
e_k	-65.0 mV	e_{ca}	0.0 mV
v_m	-22.5 mV	v_n	0.0 mV
s_m	12.0 mV	s_n	8.0 mV
τ_n	0.03 s	k_s	1.25 μM
f_c	0.003	k_p	5.0 s^{-1}
α	14.0 μM/pC		

will follow the same approach as the model with two fast variables and one slow variable. The alternative pairing of one fast and two slow variables would be relevant for studying canard dynamics [91], but we do not consider this here. More details about the model can also be found in [88].

The fast subsystem, consisting of the (v, n)-equations in (6)–(7), and its attractors can be studied by considering the slow variable c as a bifurcation parameter. The corresponding bifurcation diagram, shown in Figure 3B, forms a scaffold for understanding the burst pattern that the full model produces. Specifically, based on this fast-slow decomposition, we can assume that any general initial position with slow variable $c = c_0$ lies on a trajectory that predominantly evolves under the fast dynamics to one of the attractors that exists in the fast subsystem for $c = c_0$. Subsequently, the sign of c' will determine whether the trajectory drifts to the left or right along the corresponding attractor branch until either this branch terminates and a transition to a new attractor occurs, the trajectory goes off to infinity, or a stable state for the full system is reached. In Figure 3B, for (6)–(7) with default parameter values, the c-nullcline (dashed curve) cuts through the middle branch of the critical manifold $\mathcal{C}$, just below HC in the bifurcation diagram. According to the equation

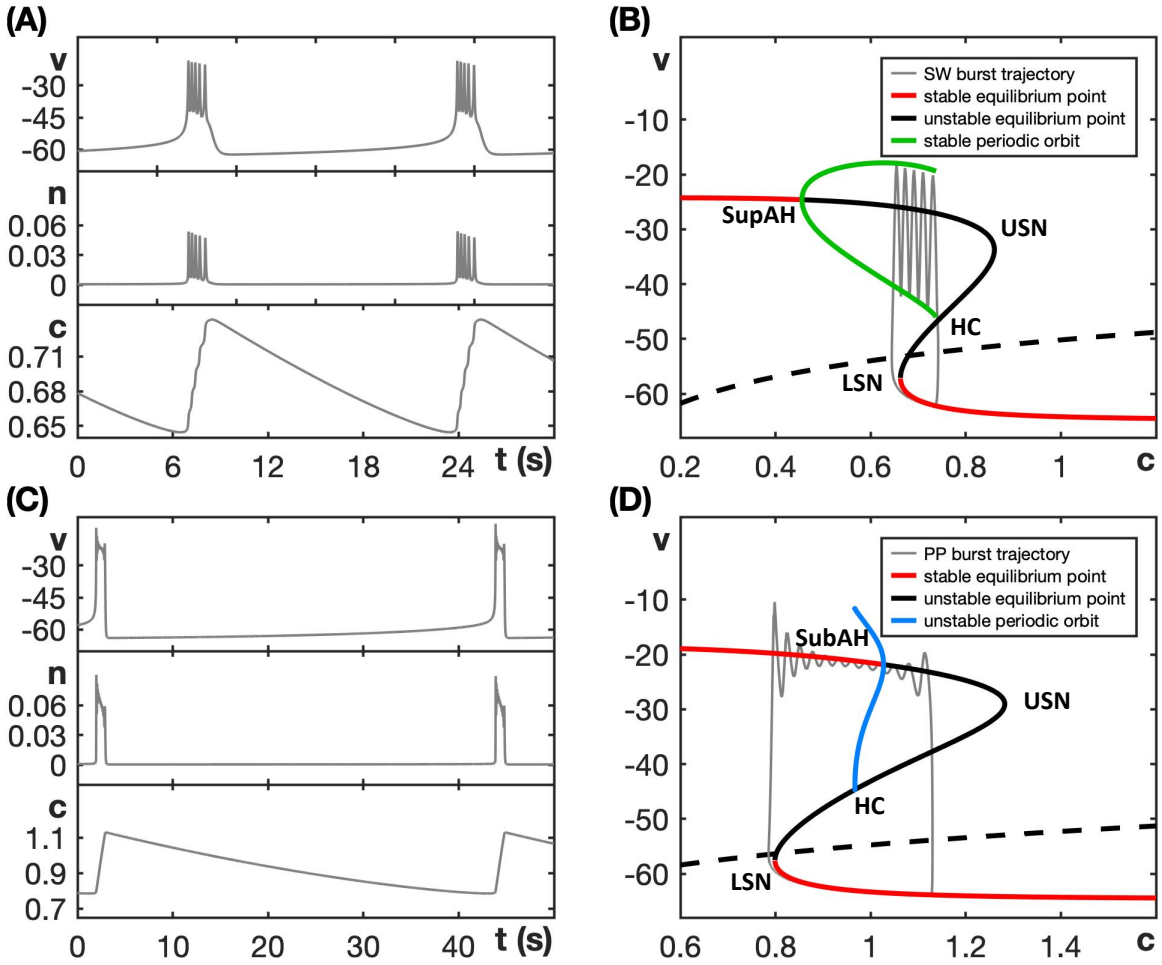

Figure 3: Fast-slow decomposition for the generic endocrine model (6)–(7). (A) SW bursting for default parameter values given in Table 1. (B) Bifurcation diagram of the model's fast subsystem with respect to the slow variable c, with bifurcation points labeled and the burst trajectory, which evolves clockwise, overlaid in grey. Oscillations start after the trajectory jumps up from the lower left saddle node (LSN) and stop when it reaches the homoclinic (HC). (C) The model exhibits PP bursting when g_{ca} is increased to 1.5; note that the ranges of c in (A) and (C) are different. (D) Bifurcation diagram as in (C) but with $g_{ca} = 1.5$; the PP burst trajectory, which also evolves clockwise, is again overlaid in grey. The labels SupAH (B) and SubAH (D) refer to supercritical and subcritical Andronov–Hopf bifurcations, respectively.

for c in (6)–(7), we have $c' < 0$ below this nullcline. Hence, c is decreasing during the silent phase and, as suggested by the bifurcation diagram of the fast subsystem, the active phase of the SW burst starts due to a jump up in potential v from the c-value at which the fast subsystem undergoes a saddle-node bifurcation (LSN). For this c-value, the attractor of the fast subsystem at elevated voltage is a periodic orbit, part of a family of such orbits that originates in a supercritical Andronov–Hopf bifurcation (SupAH). Thus, oscillations result, and they continue as c increases, according to its equation in (6)–(7), until a homoclinic bifurcation (HC) occurs. At that bifurcation, the trajectory returns to the silent phase, where it is attracted to the stable equilibria on the lower (silent) branch of $\mathcal{C}$.

When g_{ca} is increased from its default value of 0.81 to $g_{ca} = 1.5$, the model exhibits a qualitatively different PP bursting pattern (Figure 3C). The bifurcation diagram of the fast subsystem with respect to the variable c has changed correspondingly (Figure 3D). In particular, we see that the Andronov–Hopf bifurcation point has now moved to a larger c-value and has changed criticality to become subcritical (SubAH). Therefore, the fast subsystem now has a family of unstable periodic orbits. Hence, after the jump up from LSN, the trajectory is attracted to the upper branch of the critical manifold $\mathcal{C}$, which comprises stable equilibria of the fast subsystem. Since these equilibria are foci, the trajectory spirals around the upper branch of $\mathcal{C}$ while slowly moving to the right with respect to c. This behavior generates a voltage plateau in the active phase, accompanied by rapidly decaying oscillations in lieu of spikes (Figure 3C). The upper branch of $\mathcal{C}$ loses stability at SubAH, and after a small delay associated with the slow passage through an Andronov–Hopf bifurcation [62, 63, 6, 7], the trajectory jumps down to the silent phase where it flows back to LSN to complete a burst cycle.

The bifurcation diagrams in Figure 3 display SW and PP bursting patterns produced by the generic endocrine model (6)–(7) for two fixed values of g_{ca}. The robustness of these patterns and the transition between them can be studied more systematically by considering a two-parameter bifurcation diagram. Specifically, we can follow the codimension-one bifurcations labeled LSN, USN, SupAH, SubAH and HC in Figure 3B,D as curves in the two-parameter (c, g_{ca})-plane. The resulting bifurcation diagram is displayed in Figure 4A.

The two-parameter bifurcation diagram shows how the bifurcation points change, and

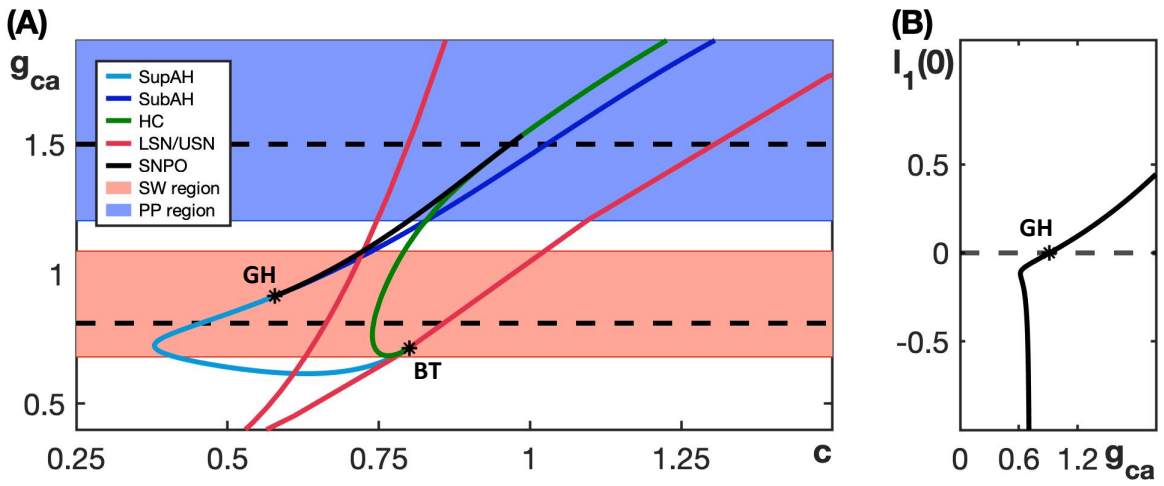

Figure 4: Dependence on g_{ca} of bifurcation curves for the fast subsystem of the generic endocrine model (6)–(7). (A) Two-parameter bifurcation diagram in the (c, g_{ca})-plane. The locus AH of Andronov–Hopf bifurcation (blue) is comprised of the two curves SupAH and SubAH that meet at the generalized Hopf point labeled GH (left black star); SupAH and the curve HC of homoclinic bifurcations merge and end at a Bogdanov–Takens point (BT; right black star) on the curve USN of saddle-node bifurcations (red). The SW and PP bursting regions are shaded red and blue, respectively.The black dashed lines correspond to the examples of SW bursting for $g_{ca} = 0.81$ and PP bursting for $g_{ca} = 1.5$ shown in Figure 3. SW bursting is lost when the curve SNPO of saddle node of periodic orbits (black) crosses the SN curve. (B) Lyapunov coefficent along the curve AH. The Andronov–Hopf bifurcation is supercritical until this coefficient increases through 0 for g_{ca} just below 1, corresponding to the point GH, and subcritical for g_{ca}-values above that.

in some cases meet and disappear, when g_{ca} varies away from its default value of 0.81 (bottom dashed line). In particular, the curves SupAH (light blue) and HC (green) of supercritical Andronov–Hopf and homoclinc bifurcations, respectively, end on the curve USN of saddle-node bifucation (red) at the codimension-two Bogdanov–Takens point BT (black star). Furthermore, the curve SupAH transitions to SubAH by changing criticality at the generalized Hopf point GH (black star just below $g_{ca} = 1$ on the curve AH in the diagram), which occurs when the first Lyapunov coefficient associated with the Andronov–Hopf bifurcation changes sign (Figure 4B); this first Lyapunov coefficient was computed numerically with MATCONT [21]. The curve subAH (dark blue) of subcritical Andronov–Hopf bifurcations then moves into the V-shaped region between the two curves LSN and USN. At the point GH, a curve of saddle-node bifurcation of periodic orbits (SNPO) originates and progresses to larger c-values as g_{ca} continues to increase, until it ends just above $g_{ca} = 1.5$ on the curve HC. In the remainder of the chapter, we will denote as AH the locus or curve of Andronov-Hopf bifurcation comprised of the components SupAH and SubAH.

The lower black dashed line in Figure 4A corresponds to the bifurcation diagram for $g_{ca} = 0.81$ in Figure 3B that gives rise to SW bursting. In the direction of increasing c, we successively encounter the supercritical Andronov–Hopf bifurcation SupAH (light blue), the saddle-node bifurcation LSN (red), the homoclinic bifurcation HC (green), and the other saddle-node bifurcation USN (red). If we use c_{X} to denote the c-value at which a bifurcation of type X occurs, then the order of bifurcations for fixed $g_{ca} = 0.81$ is $c_{\mathsf{SupAH}} < c_{\mathsf{LSN}} < c_{\mathsf{HC}} < c_{\mathsf{USN}}$. This order of bifurcations is maintained for lower values of g_{ca}, until HC disappears, just below the point BT. Hence, since $c_{\mathsf{SupAH}} < c_{\mathsf{LSN}}$, the active phase is characterized by stable periodic orbits, and persists until $c \approx c_{\mathsf{HC}}$; we conclude that these g_{ca}-values all give rise to SW bursting. Similarly, for larger g_{ca}-values, even though SubAH and LSN cross, the change in criticality at GH implies that the active phase is still characterized by stable periodic orbits until the saddle-node bifurcation of periodic orbits SNPO occurs after LSN; that is, for SW bursting, we require $c_{\mathsf{SNPO}} < c_{\mathsf{LSN}}$.

The order of the bifurcations along the black dashed line for $g_{ca} = 1.5$ in Figure 4A, which corresponds to PP bursting shown in Figure 3D, is $c_{\mathsf{LSN}} < c_{\mathsf{SNPO}} < c_{\mathsf{HC}} < c_{\mathsf{SubAH}} < c_{\mathsf{USN}}$; it is important that c_{SNPO} is only just smaller than c_{HC}, which means that this order generates

a PP pattern that is qualitatively similar to that for g_{ca}-values above the point where SNPO ends, which feature the bifurcation sequence $c_{\mathsf{LSN}} < c_{\mathsf{HC}} < c_{\mathsf{SubAH}} < c_{\mathsf{USN}}$. While we did not check all g_{ca}-values, this order of bifurcations is maintained until at least $g_{ca} = 2$.

The red and blue shaded regions in Figure 4A show the ranges of g_{ca}-values over which the generic endocrine model (6)–(7) can potentially exhibit SW and PP bursting, respectively. Choosing parameters in one of these regions is, in fact, not sufficient to ensure that the corresponding burst pattern occurs, since the actual burst pattern also depends on the position of the c-nullcline — which changes with g_{ca} due to the presence of I_{Ca} in the c-equation in (6)–(7) — and the speed at which c evolves. We conclude from this diagram, however, that SW bursting can at most be maintained for $0.65 < g_{ca} < 1.1$.

Figure 5 compares the burst patterns of the generic endocrine model (6)–(7) for different values of g_{ca}. At $g_{ca} = 0.75$, the model exhibits SW bursting (Figure 5A) that is very similar to that for the default value $g_{ca} = 0.81$ (Figure 3A). When g_{ca} is increased to 1.0, the model still exhibits SW bursting (Figure 5B), but the increase in g_{ca} strengthens I_{Ca}, which results in a more elevated v at peaks of the bursts. At this elevated v, the current I_K activates more strongly compared to the previous case, resulting in stronger hyperpolarizations between spikes and fewer spikes in the burst. When g_{ca} is increased still further to 1.6, the activity pattern transitions to PP bursting (Figure 5C). This case yields the strongest I_{Ca} activation of the three; indeed, despite the induced elevation of v and corresponding strong activation of I_K, the latter current cannot overcome I_{Ca} and cause repolarization. Thus, the equilibria on the upper branch of the critical manifold $\mathcal{C}$ stabilize and spike oscillations during the active phase are prevented.

2.2.1.2 Sodium-Potassium Minimal Model

The sodium-potassium minimal model introduced in [43] is an example of an SW burster comprised of only the basic essentials needed to burst. This model consists of the following differential equations:

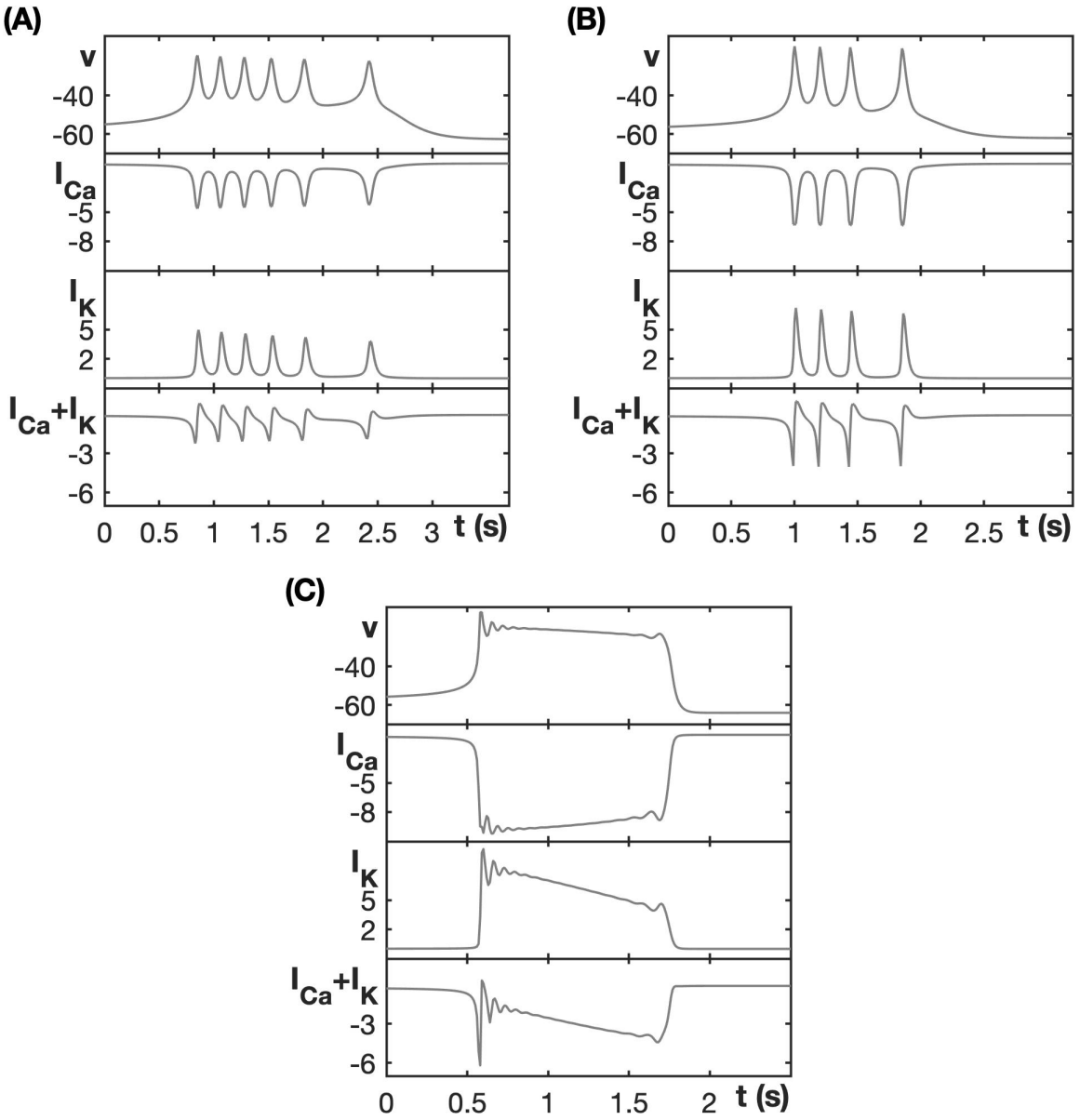

Figure 5: Burst patterns exhibited by the generic endocrine model (6)–(7) for different values of g_{ca}, along with associated currents. (A) SW bursting at $g_{ca} = 0.75$. (B) SW bursting at $g_{ca} = 1.0$ with larger amplitude spikes than in (A). (C) PP bursting for $g_{ca} = 1.6$.

$$\begin{cases} c_m\, v' &= -I_L(v) - I_{Na}(v) - I_K(v,n) \\ & \quad -I_S(v,s) + I, \\ n' &= (n_\infty(v) - n)/\tau_n, \\ s' &= (s_\infty(v) - s)/\tau_s. \end{cases} \tag{8}$$

The expressions for the currents and steady state activation functions for the model are given by:

$$\begin{aligned} I_L(v) &= g_l\,(v - e_l), \\ I_{Na}(v) &= g_{na}\, m_\infty(v)\,(v - e_{na}), \\ I_K(v,n) &= g_k\, n\,(v - e_k), \\ I_S(v,s) &= g_{km}\, s\,(v - e_k), \\ m_\infty(v) &= (1 + e^{(v_m - v)/s_m})^{-1}, \\ n_\infty(v) &= (1 + e^{(v_n - v)/s_n})^{-1}, \\ s_\infty(v) &= (1 + e^{(v_s - v)/s_s})^{-1}. \end{aligned} \tag{9}$$

Note that I_S denotes a potassium current with gating that evolves much slower than that for I_K. Again, we choose default parameter values, given in Table 2, for which the model exhibits SW bursting as shown in Figure 6A. The bifurcation diagram of the model's fast subsystem for default parameter values is shown in Figure 6B. Notice that the order of bifurcations, in the direction of increasing s, is the same as in Figure 3B, that is, $s_{\mathsf{SupAH}} < s_{\mathsf{LSN}} < s_{\mathsf{HC}} < s_{\mathsf{USN}}$. By comparing timescales after non-dimensionalization of this model (see the Appendix), we find that the timescale constants of v, n and s are approximately $R_v \approx 20$, $R_n \approx 6.57$ and $R_s \approx 0.005$, respectively. The rate $R_v \approx 20$ varies linearly with g_{na} as long as $g_{na} > 9 = g_k$; if g_{na} is decreased below this value, $R_v \approx 9$ is determined by g_k instead and any further decrease in g_{na} would not affect R_v. Hence, the variables v and n are considerably faster than s, irrespective of the value for g_{na}.

Even though the sodium-potassium minimal model (8)–(9) is designed to exhibit SW bursting, it is capable of other activity patterns. For example, Supplemental Figure 46 shows the non-spiking pattern generated for $g_{na} = 35$ in which all solutions are attracted to a stable steady state at an elevated voltage level, which corresponds to a state of depolarization block.

Table 2: Sodium-Potassium Minimal Model (8)–(9): default parameters values.

c_m	1 pF	I	5 pA
g_l	8 nS	g_{na}	20 nS
g_k	9 nS	g_s	5 nS
e_l	−80 mV	e_{na}	60 mV
e_k	−90 mV	v_m	−20 mV
v_n	−25 mV	v_s	−20 mV
s_m	15 mV	s_n	5 mV
s_s	5 mV	τ_n	0.15 ms
τ_s	200 ms		

For this large value of g_{na}, the nullcline of the slow variable s intersects the upper branch of the critical manifold, which gives rise to a stable steady state of the full system. However, SW bursting is already lost for smaller g_{na}-values. Figure 6C shows the two-parameter bifurcation diagram of the fast subsystem in the (s, g_{na})-plane. As in Section 2.2.1.1, the ordering of bifurcation curves suggests that system (8)–(9) can potentially exhibit SW bursting for g_{na}-values between 20 and 25, if the slow dynamics is tuned appropriately; this region is again shaded red. We computed the first Lyapunov coefficient associated with the Andronov-Hopf bifurcation (Figure 6D) and found that it is negative for the default g_{na} and remains so up until a much larger value, $g_{na} \approx 65$. Hence, this system does not transition to PP bursting, at least not for $s \in (0, 1)$, the physically relevant range. Instead, for $g_{na} > 32$ or so, system (8)–(9) moves into a state of depolarization block, which is the region shaded light blue in Figure 6B.

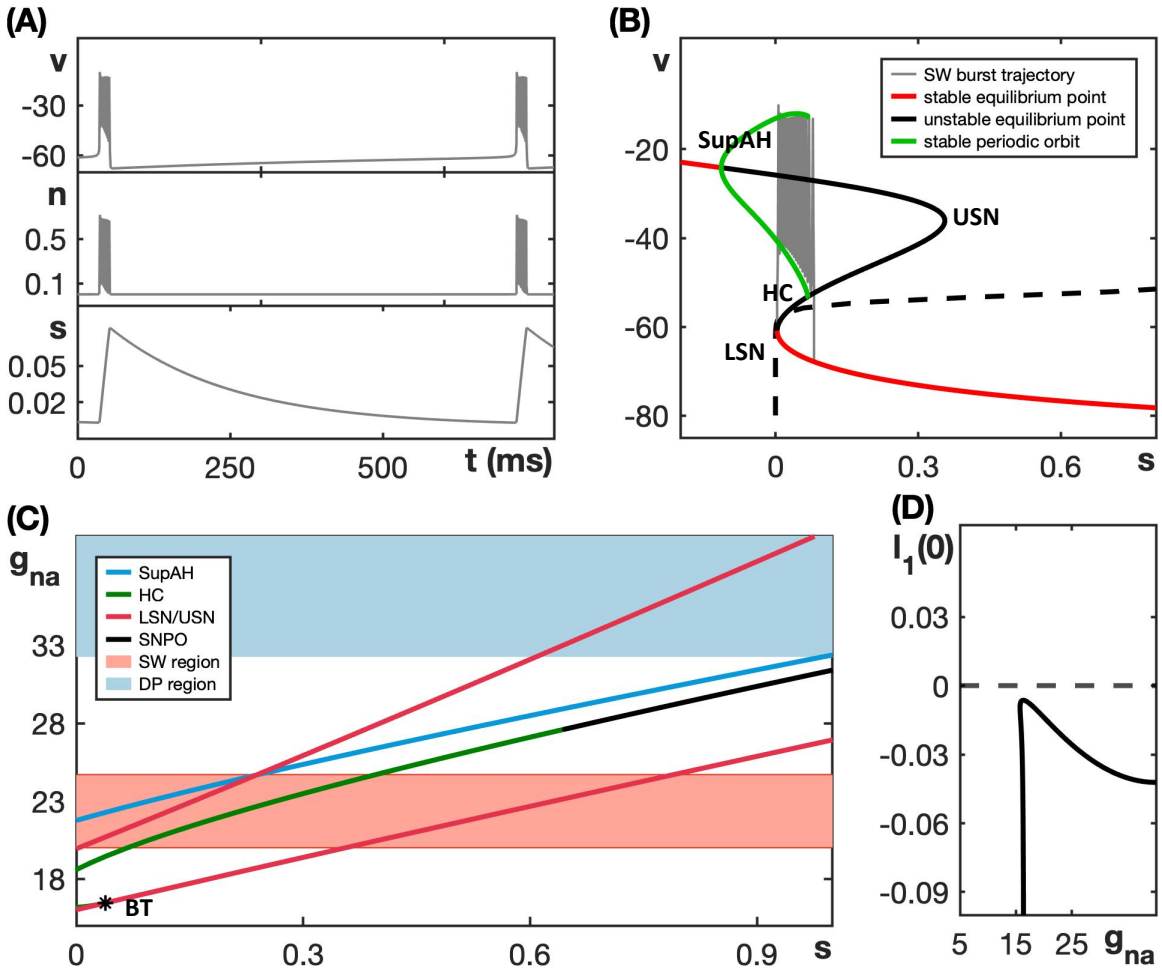

Figure 6: Dynamics and bifurcation structure for the sodium-potassium minimal model (8)–(9). (A) SW bursting for the default parameters given in Table 2. (B) Bifurcation diagram of the model's fast subsystem with respect to the slow variable s for default parameter values, with the SW burst overlaid in grey. (C) Two-parameter bifurcation diagram of the fast subsystem in the (s, g_{na})-plane; colors are as in Figure 4A and the SW bursting region is shaded red. For realistic values ($s < 1$), this model does not transition to PP. The light-blue shaded region corresponds to g_{na}-values for which the full system has a stable steady state at elevated v. (D) Lyapunov coefficient along the curve SupAH. The Andronov–Hopf bifurcation is supercritical until around $g_{na} = 65$, which lies outside the range shown in panel (C).

2.2.1.3 Minimal Chay-Keizer Model

Next, we consider the minimal Chay–Keizer model described in [70, 69]. This model takes the form :

$$\left\{\begin{array}{rcl} c_m\, v' &=& -I_L(v) - I_{Ca}(v) - I_K(v,n) \\ & & -I_{K(Ca)}(v,c)), \\ n' &=& (n_\infty(v) - n)/\tau_n(v), \\ c' &=& -f_c\,(\alpha\, I_{ca}(v) + k_p\, c). \end{array}\right. \tag{10}$$

The currents and steady state activation functions for the model are given by:

$$I_L(v) = g_l\,(v - e_l), \tag{11}$$

$$\begin{aligned} I_{Ca}(v) &= g_{ca}\, m_\infty^3(v)\, h_\infty(v)\,(v - e_{ca}), \\ I_K(v,n) &= g_k\, n\,(v - e_k), \\ I_{K(Ca)}(v,c) &= g_{kca}\,\frac{c}{1+c}\,(v - e_k), \\ a_m(v) &= \frac{0.1\,(v+25)}{1 - e^{-0.1(v+25)}}, \\ b_m(v) &= 4\, e^{-(v+50)/18}, \\ m_\infty(v) &= \frac{a_m(v)}{a_m(v) + b_m(v)}, \\ a_n(v) &= \frac{0.01\,(v+20)}{1 - e^{-0.1(v+20)}}, \\ b_n(v) &= 0.125\, e^{-(v+30)/80}, \\ n_\infty(v) &= \frac{a_n(v)}{a_n(v) + b_n(v)}, \\ \tau_n(v) &= \frac{3.33}{a_n(v) + b_n(v)}, \\ a_h(v) &= 0.07\, e^{-(v+50)/20}, \\ b_h(v) &= \frac{1}{e^{-0.1*(v+20)} + 1}, \\ h_\infty(v) &= \frac{a_h(v)}{a_h(v) + b_h(v)}. \end{aligned}$$

Table 3: Minimal Chay–Keizer Model (10)–(11): default parameters values.

c_m	1 μF/cm^2	g_l	0.006985 mS/cm^2
g_{ca}	1.79934 mS/cm^2	g_k	1.69765 mS/cm^2
g_{kca}	0.0104998 mS/cm^2	e_k	-75 mV
e_{ca}	100 mV	e_l	-40 mV
k_p	0.00513 ms^{-1}	f_c	0.0058
α	0.02591 $\mu M/nC$		

We choose the default parameter values given in Table 3, for which the model exhibits SW bursting as displayed in Figure 7A.

Non-dimensionalization (see the Appendix) shows that the timescale constants of v and c in this model are $R_v \approx 1.8$, $R_c \approx 0.004$ respectively, while the time constant R_n for n depends on v and varies between 0.05 to 0.1 over the relevant range of v values. In this model, both R_v and R_c depend on g_{ca}. We choose an upper bound of 4 on g_{ca}, which is double the default value. At this maximal value, we have $R_v \approx 4$ and $R_c \approx 0.008$, or roughly twice the default values. Even with these timescale constants, v and n can be considered fast compared to c.

The minimal Chay–Keizer model (10)–(11) exhibits SW bursting for the default parameter values given in Table 3 and PP busting when g_{ca} increases to 3.2; see Figure 7A,C. The corresponding bifurcation diagrams of the model's fast subsystem with respect to the slow variable are shown in Figure 7B,D. The two-parameter bifurcation diagram in the (ca, g_{ca})-plane shown in Figure 8A illustrates how the bifurcations of the fast subsystem depend on g_{ca}. Based on the relative order of the bifurcation curves, we conclude that the minimal Chay–Keizer model (10)–(11) can potentially exhibit SW bursting for $1.5 < g_{ca} < 2.8$ (red shaded region) and PP bursting for g_{ca} near 3.2 (narrow blue shaded region). When g_{ca} is further increased, the Andronov–Hopf bifurcation moves to larger values of c, such that the

nullcline of the slow variable c intersects the upper branch of the critical manifold at a stable equilibrium point. In doing so, the full system now has a stable steady state and, hence, for sufficiently large g_{ca}-values, the system exhibits depolarization block with voltage suspended at an elevated level (light-blue shaded region).

2.2.1.4 Butera Model

The Butera model is a seminal minimal model used to study rhythm generation in respiratory neurons [18]. This model consists of the following differential equations:

$$\begin{cases} c_m\, v' &= -I_L(v) - I_{Na}(v,n) - I_K(v,n) \\ & \quad -I_{NaP}(v,p) - I_{ton}(v), \\ n' &= (n_\infty(v) - n)/\tau_n, \\ p' &= (p_\infty(v) - p)/\tau_p(v), \end{cases} \tag{12}$$

where I_{NaP} denotes a persistent sodium current. The expressions for the currents and steady state activation functions are as follows:

$$\begin{aligned} I_L(v) &= g_l\,(v - e_l), \\ I_{Na}(v,n) &= g_{na}\, m_\infty^3(v)\,(1-n)\,(v - e_{na}), \\ I_K(v,n) &= g_k\, n^4\,(v - e_k), \\ I_{NaP}(v,p) &= g_{nap}\, m\, p_\infty(v)\, p\,(v - e_{na}), \\ I_{ton}(v) &= g_{ton}\,(v - e_{syn}), \\ m_\infty(v) &= (1 + e^{(v_m - v)/s_m})^{-1}, \\ n_\infty(v) &= (1 + e^{(v_n - v)/s_n})^{-1}, \\ mp_\infty(v) &= (1 + e^{(v_{mp} - v)/s_{mp}})^{-1}, \\ p_\infty(v) &= (1 + e^{(v_p - v)/s_p})^{-1}, \\ \tau_n(v) &= \tau_n\,(\cosh((v - v_n)/(2s_n)))^{-1}, \\ \tau_p(v) &= \tau_p\,(\cosh((v - v_p)/(2s_p)))^{-1}. \end{aligned} \tag{13}$$

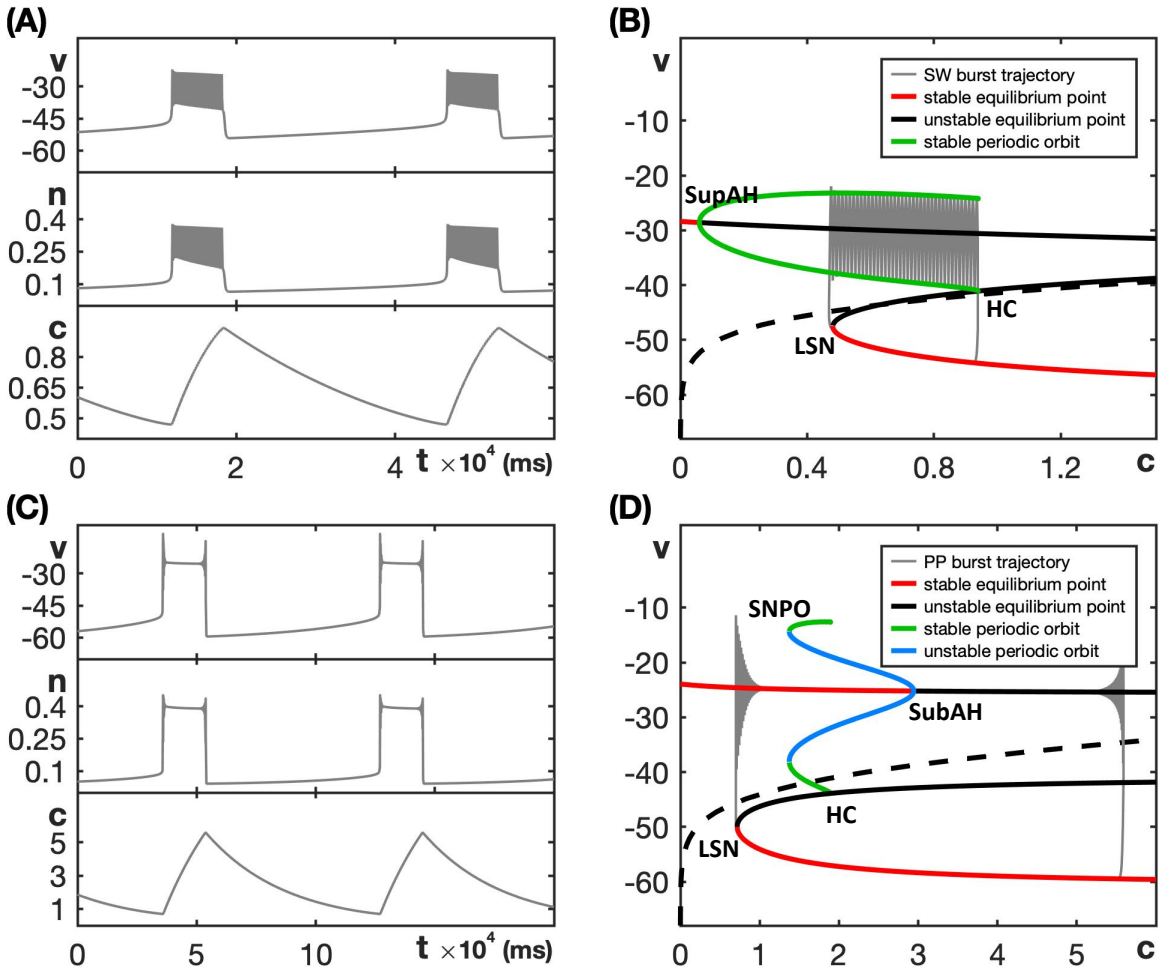

Figure 7: Dynamics and bifurcation structure for the minimal Chay–Keizer model (10)–(11). (A) SW bursting for the default parameters given in Table 3. (B) Bifurcation diagram of the model's fast subsystem with respect to the slow variable c for default g_{ca} value. The SW burst trajectory is overlaid in grey. (C) The model exhibits PP bursting for $g_{ca} = 3.2$; note the difference in c-range between (A) and (C). (D) The bifurcation diagram as in (B) but with $g_{ca} = 3.2$.

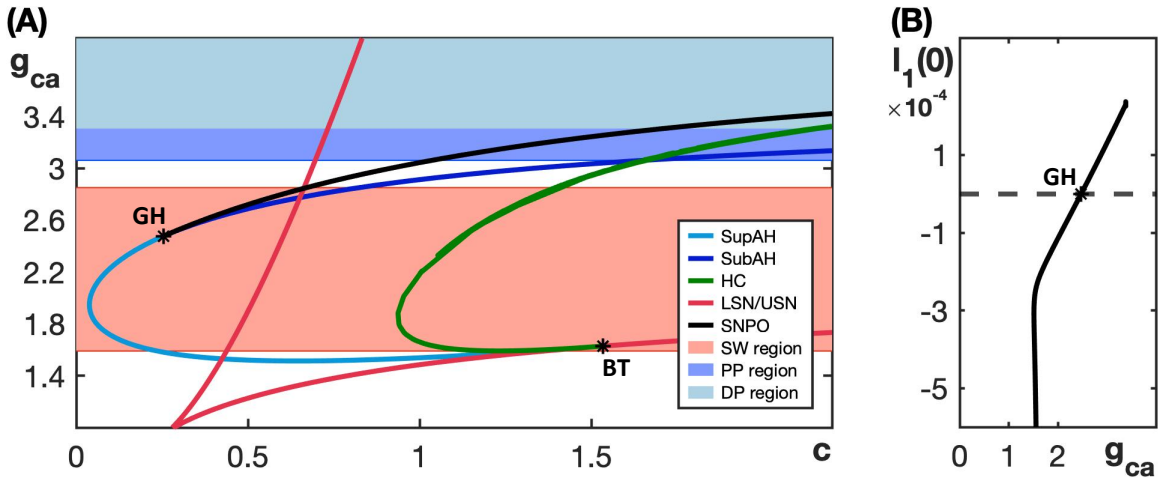

Figure 8: (A) Two-parameter bifurcation diagram of the fast subsystem of the minimal Chay–Keizer model (10)–(11) in the (c, g_{ca})-plane; colors are as in Figure 4A and the SW bursting region is shaded red, the narrow PP region is shaded blue, and the light-blue shaded region just above that corresponds to a state of depolarization block. (B) Lyapunov coefficient along the curve AH, comprised of SupAH and SubAH. The Andronov–Hopf bifurcation is supercritical for g_{ca} below the axis crossing close to $g_{ca} = 2.5$ and subcritical for larger g_{ca}. Note that the curve ends at the horizontal g_{ca}-asymptote.

Table 4: Butera Model (12)–(13): default parameters values.

c_m	21 pF	g_l	2.8 nS
g_{na}	28 nS	g_k	11.2 nS
g_{nap}	2.8 nS	g_{ton}	0.3 nS
g_{syn}	0 nS	e_l	−65 mV
e_{na}	50 mV	e_k	−85 mV
e_{syn}	0 mV	v_n	−29 mV
v_m	−34 mV	v_{mp}	−40 mV
v_p	−48 mV	s_m	−5 mV
s_n	−4 mV	s_p	6 mV
s_{mp}	−6 mV	τ_n	10 ms
τ_p	10000 ms		

We choose default parameters as given in Table 4, such that the model exhibits SW bursting shown in Figure 9A. Non-dimensionalization (see the Appendix) shows that the timescale constants of v, n and p are $R_v \approx 1.33$, $R_n \approx 0.17$ and $R_p \in [0.0001, 0.003]$, respectively. Decreasing g_{na} decreases R_v, but R_p remains much smaller than R_v and R_n. Hence, we can again consider v and n as fast variables, with p the slow variable for this model.

Figure 9B shows the bifurcation diagram of the fast subsystem for the default parameter values. Observe that, even though the Andronov–Hopf bifurcation is subcritical, a family of stable periodic orbits (blue) originates from a saddle-node bifurcation of periodic orbits (SNPO). The SW burst trajectory (grey) is overlaid in Figure 9B and evolves counterclockwise.

Figure 9C shows the two-parameter bifurcation diagram for the fast subsystem in the (p, g_{na})-plane. Notice that, in this figure, the order for the curves LSN and USN is reversed compared to the other models; compare also with Figure 9B, where USN occurs at a negative value of p and is, hence, not visible in the view that is shown. For the Butera model (12)–(13), the SW bursting region (shaded red) persists as g_{na} increases, because there always exists a family of stable periodic orbits of the fast subsystem in the region bounded by the curves HC and LSN. Indeed, even though the Andronov–Hopf bifurcation (blue) changes criticality at GH and is subcritical for $g_{na} > 7.3$ (Figure 9D), the curve SNPO of saddle-node bifurcation of periodic orbits that emanates from GH persists and stays to the right of the LSN (leftmost red curve). Hence, the fast subsystem always features a family of stable oscillations, which originate from SNPO and end (as p decreases) at HC (green). These stable oscillations support spiking in the active phase.

2.2.2 Model Modifications to Include Slow Negative Feedback

The biophysical mechanisms behind spiking for the canonical Hodgkin–Huxley model [41] include (i) a fast activating, more slowly inactivating inward sodium current that results in the upstroke of the spike and (ii) an outward, negative feedback potassium current, which activates on a timescale similar to that of the sodium inactivation, responsible for the downstroke of the spike [83]. Typical bursting models feature (i) and (ii) and also add in a

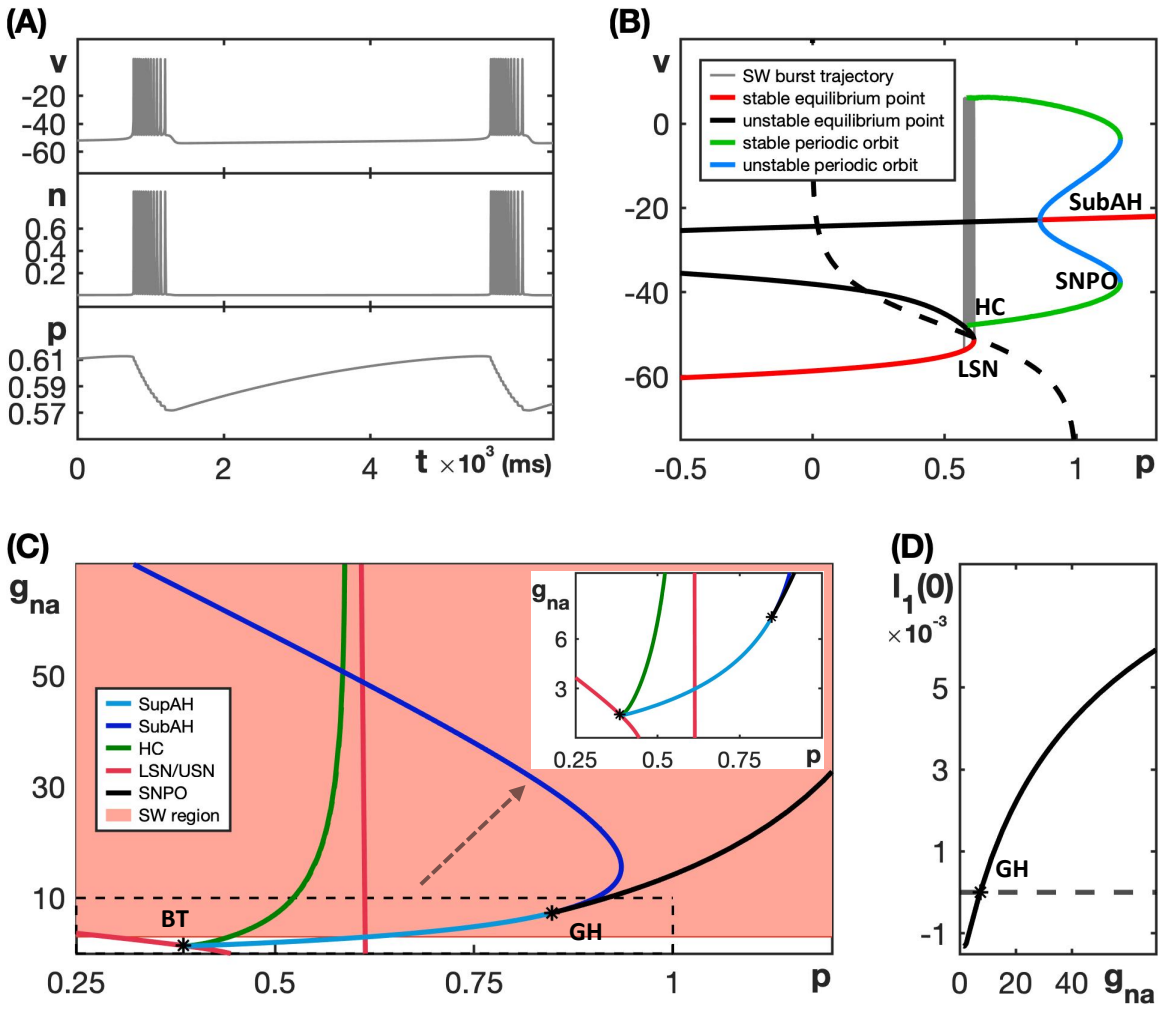

Figure 9: Dynamics and bifurcation structure for the Butera model (12)–(13). (A) SW bursting for the default parameters given in Table 4. (B) Bifurcation diagram of the model's fast subsystem with respect to the slow variable p, together with the SW burst trajectory for the default parameters given in Table 4 overlaid in grey (evolution is counterclockwise). (C) Two-parameter bifurcation diagram of the fast subsystem in the (p, g_{na})-plane; colors are as in Figure 4A and the SW bursting region is shaded red. (D) Lyapunov coefficent along the curve AH, comprised of SupAH and SubAH. The Andronov–Hopf bifurcation is supercritical only for $g_{na} < 7.3$, but a saddle-node of periodic orbits SNPO occurs at GH that generates a family of stable periodic orbits necessary for SW bursting. The inset is an enlargement of the indicated region near BT and GH.

third, slowest current or variable that helps to modulate the burst between its active and silent phases [43]. These components arise, in particular, in the neural and endocrine models presented in Section 2.2.1, which exhibit SW bursting in some region of parameter space. In the case of the generic endocrine model (6)–(7), for example, the calcium current I_{Ca} is an inward current with fast activation and, hence, provides fast positive feedback to v, while the potassium current I_K is an outward current with a slower activation gate n that provides the slow negative feedback; moreover, the slowest variable c, corresponding to the calcium concentration in the cell, modulates the burst.

Compared to the other models presented in Section 2.2.1, the Butera model (12)–(13) maintains SW bursting over a broad range of parameter values, as can be seen in Figure 9C (red shaded region). The fast current in the Butera model is a sodium current, which is different from the fast calcium currents in the generic endocrine and minimal Chay–Keizer models, as well as the sodium current in the sodium-potassium minimal model, because I_{Na} has a slow inactivation gate in this model. Past work has highlighted the roles of positive and negative feedback terms in tuning the features of neural spiking [34] and the potential importance of slow positive feedback in enhancing the robustness of bursting [33].

In this vein, we hypothesized that the robustness of SW bursting in the Butera model could relate to the fact that the additional negative feedback present in the model is slow relative to the fast activation. To test this idea, we modified each of the other three models to include a slow, voltage-dependent inactivation gate as part of the fast inward current, which allowed us to study how the inclusion of such a component alters each model's dynamics.

The modified calcium current I_{Ca} for the generic endocrine model (6)–(7) is given by

$$I_{Ca}(v) = g_{ca}\, m_\infty^2(v)\, h\, (v - e_{ca}), \tag{14}$$

and the modified sodium current I_{Na} for the sodium-potassium minimal model (8)–(9) takes the form

$$I_{Na}(v) = g_{na}\, m_\infty(v)\, h\, (v - e_{na}), \tag{15}$$

where h in equations (14) and (15) is the voltage-dependent inactivation gating variable governed by the equation

$$h' = (h_\infty(v) - h)/\tau_h \tag{16}$$

with

$$h_\infty(v) = (1 + e^{(v_h - v)/s_h})^{-1}.$$

In its original form, the minimal Chay–Keizer model (10)–(11) has a fast inactivation term $h = h_\infty(v)$ associated with I_{Ca}. So to study this model, we changed the inactivation to a slow one by modifying the calcium current to take the form

$$I_{Ca}(v) = g_{ca}\, m_\infty^3(v)\, h\, (v - e_{ca}), \tag{17}$$

where h again evolves according to equation (16).

Since h is a dimensionless variable that takes values between 0 and 1, the coupling of the h-dynamics via equations (14), (15) or (17) does not affect the timescale constants of the other variables in the models. The timescale constant for (16) is $R_h \approx Q_t/\tau_h = 1/\tau_h$, which can be derived similarly to the timescale of n (see the Appendix). For each model, we will explore how the dynamics and bifurcation structure change as τ_h is varied over a range of values. In each case, we choose this range to be roughly comparable with the model's respective τ_n-value, such that h and n evolve on similar timescales.

For the modified generic endocrine model (6)–(7), (14) and (16), the half-inactivation value v_h was selected to be -30, which is approximately in the middle of the range of v-values corresponding to the spiking phase of SW bursting in Figure 3A. For simplicity, s_h was kept constant at -1. In the Butera model (12)–(13), the inactivation of I_{Na} is approximated as $1 - n$ where n is the activation variable of I_K. Following this idea, v_h and s_h of the modified sodium-potassium minimal model (8)–(9) and (15)–(16) were chosen as -25 and -5, respectively, to match the values associated with corresponding terms for I_K in that model. For the modified minimal Chay–Keizer model (10)–(11) and (16)–(17) we retained the default definitions and parameter values for $h_\infty(v)$ given in Table 3.

2.3 Results

In this section we investigate the robustness of SW bursting to variation of the fast inward current conductance for each of the three modified models. We first analyze how

this robustness depends on the the timescale constant τ_h. For the values that we include, all of the modified models can be considered as fast-slow systems with fast variables v, n, and h and a single slow variable. Hence, we can apply a similar fast-slow analysis to these modified models to that employed in Section 1.2. We also consider the effect of varying the conductance g_k associated with the potassium current that is present in all four models and complete our results with a two-parameter analysis with respect to g_k and the inverse τ_h^{-1} of the timescale constant.

2.3.1 Bifurcation Diagrams of Modified Models

Figures 10, 11 shows two-parameter bifurcation diagrams of the respective fast subsystem for each of the three modified models for a fixed τ_h value; here, we plot the slow variable (c or s) on the horizontal and the conductance of fast inward current (g_{ca} or g_{na}) on the vertical axis. These bifurcation diagrams should be compared to Figures 4, 6, and 8, respectively. Notice that in all of these diagrams, the curve AH of Andonov–Hopf bifurcations is pushed out far to the left of the leftmost saddle-node curve LSN as g_{ca} or g_{na} increases. This arrangement of bifurcations ensures the existence of a family of stable periodic orbits in the fast subsystem over a larger range of g_{ca} or g_{na}, which prevents a transition to PP bursting. Instead, the pattern exhibited in each case is either SW bursting or slow spiking, depending on the position of the curve HC of homoclinic bifurcations. Specifically, if the curve HC does not reach the curve LSN and the Andronov–Hopf bifurcation is supercritical (or subcritical with a curve SNPO of saddle-node bifurcation of periodic orbits located even farther away from LSN), then SW bursting results. On the other hand, if the homoclinic curve reaches LSN, which induces a so-called SNIC regime (saddle-node bifurcation on invariant cycle) [27], then the model exhibits slow spiking. In all of the two-parameter diagrams shown in Figures 10, 11, the SW and slow spiking regions are shaded red and purple, respectively.

The bifurcation diagram for the modified generic endocrine model (6)–(7), (14) and (16) in the (c, g_{ca})-plane with $\tau_h = 0.033$ (Figure 10A) shows a clear expansion in the range of g_{ca}-values for which the model exhibits SW bursting relative to the original model (cf. Figure 4). Indeed, when the Andronov–Hopf bifurcation switches from supercritical to subcritical for

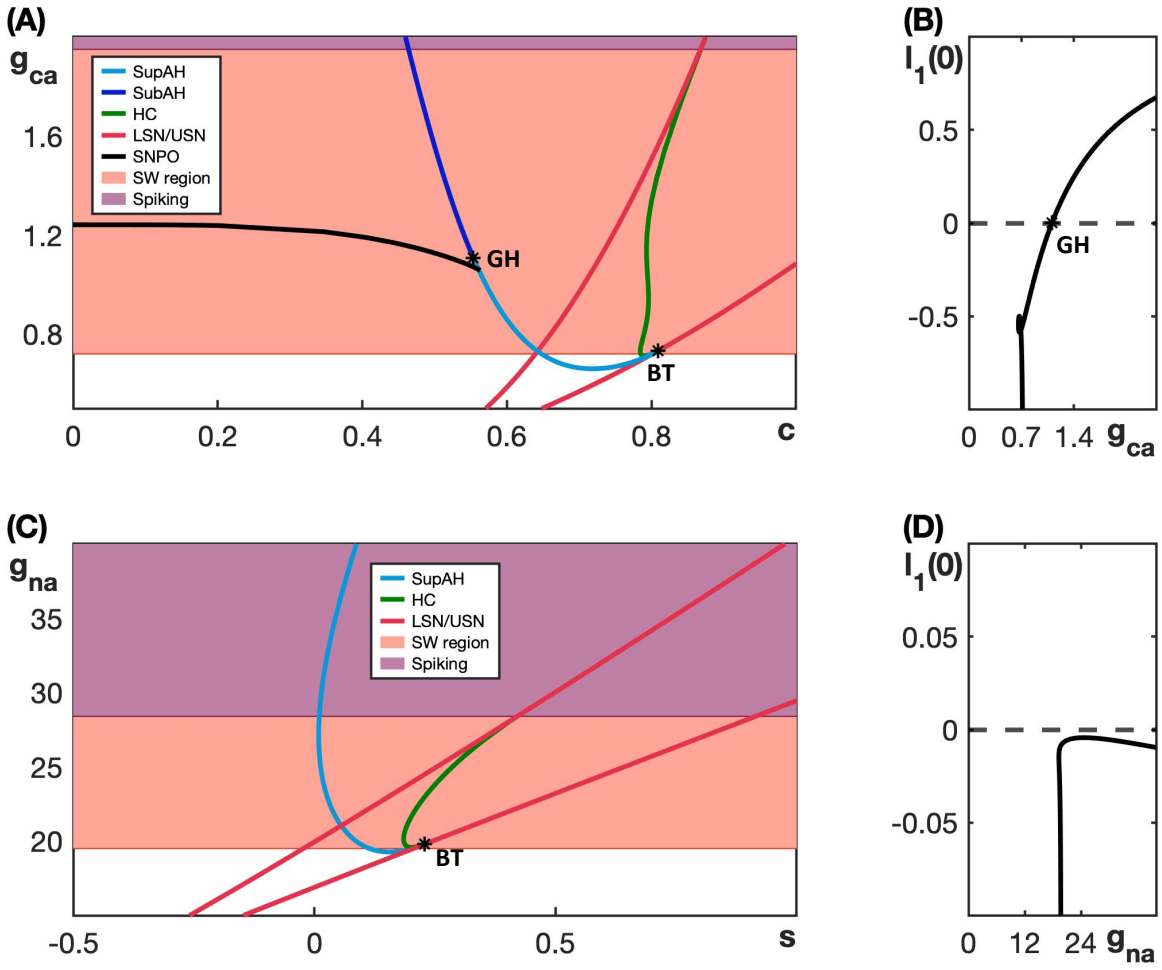

Figure 10: (A) Two-parameter bifurcation diagram of the fast subsystem for Modified generic endocrine model (6)–(7), (14) and (16) with respect to the corresponding slow variable c and conductance g_{ca}. (B) Lyapunov coefficent associated with the curve AH (comprised of SupAH and SubAH) in (A), plotted versus g_{ca} with $\tau_h = 0.033$. (C)Two-parameter bifurcation diagram of the fast subsystem Modified sodium-potassium minimal model (8)–(9) and (15)–(16) with respect to the corresponding slow variable s and conductance g_{na} for $\tau_h = 0.125$. (D) Lyapunov coefficent associated with the curve SupAH in (C), plotted versus g_{na}. The modified models show broader parameter ranges over which they exhibit SW bursting (shaded red) compared to those in Figures 4 and 6 for the unmodified models. Moreover, unlike the originals, the modified models does not yield transitions to PP bursting or depolarization block.

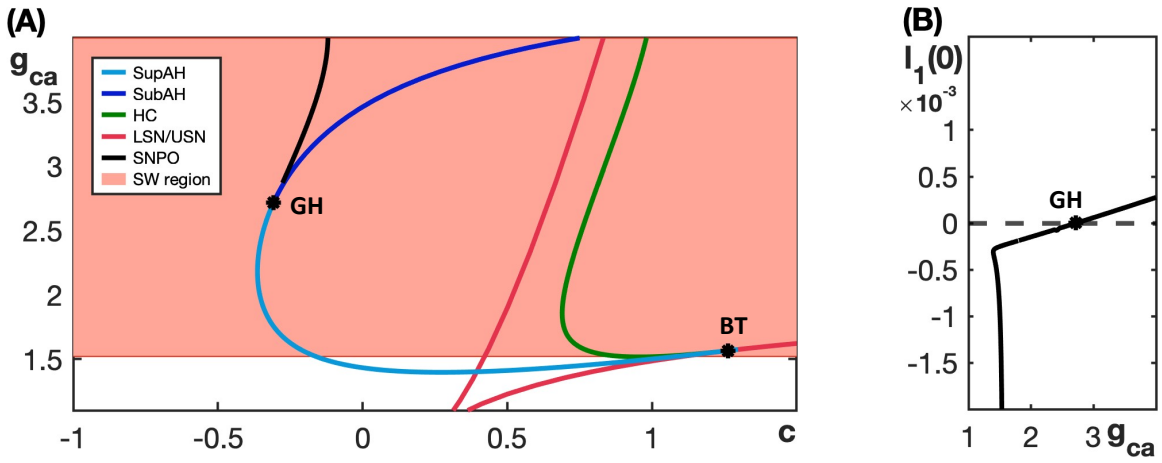

Figure 11: (E) Two-parameter bifurcation diagram of the fast subsystem for Modified minimal Chay–Keizer model (10)–(11) and (16)–(17) with respect to the corresponding slow variable c and conductance g_{ca} for $\tau_h = 1.111$. (F) Lyapunov coefficent associated with the curve AH in (E), plotted versus g_{ca}. The modified model show broader parameter ranges over which they exhibit SW bursting (shaded red) compared to 8 for the unmodified model. Moreover, the original, the modified model does not yield transitions to PP bursting or depolarization block.

g_{ca} just above 1 (Figure 10B), a saddle-node bifurcation of periodic orbits (SNPO) occurs to the left of the curve AH and therefore stable oscillations persist, extending in the direction of increasing c until the curve HC is reached. Consequently, a transition to PP bursting is now prevented. Instead, when SW bursting is lost for g_{ca} just below 2, due to the transition from the HC to the SNIC, the modified model generates slow spiking.

In the case of the modified sodium-potassium minimal model (8)–(9) and (15)–(16), the two-parameter bifurcation diagram in the (s, g_{na})-plane with $\tau_h = 0.125$ (Figure 10C) features a slightly expanded SW bursting range. Recall that SW bursting for the original sodium-potassium minimal model (Figure 6B) is not especially robust to parameter changes. Even though SW bursting never transitions to PP bursting for the original form of this model, when g_{na} is increased above the SW range, the original model exhibits some intermediate patterns and then transitions to a full-system stable steady state at elevated voltage. In the modified model, on the other hand, when SW bursting is lost, the system switches to slow spiking through the transition to a SNIC (Figure 10C). There is also no longer a change in criticality of the Andronov–Hopf bifurcation (Figure 10D) in this modified model, at least not over the range of g_{na}-values considered.

The modified minimal Chay–Keizer model (10)–(11) and (16)–(17) with $\tau_h = 1.111$ shows an expansion in its SW region in the (c, g_{ca})-plane relative to the original version of the model (compare Figure 8 with Figure 11A) and, similarly to the other modified models, it no longer supports PP bursting. Instead, the SW regime features a curve SubAH of subcritical Andronov-Hopf bifurcation (Figure 11B), with an associated family of stable periodic orbits originating at the curve SNPO. Although these bifurcation curves lie at non-physiological, negative c-values, the stable periodic orbits extend to positive c and terminate at the curve HC in the SW bursting regime. The modified model transitions directly from SW bursting to spiking as g_{ca} is increased, organized by the switch to the SNIC mechanism.

Figure 12 compares the burst patterns of the modified generic endocrine model (6)–(7), (14) and (16) for progressively increasing values of g_{ca}. The first two panels are very similar to those of Figure 5 for the unmodified model. With the modification, h can decay on each spike, but that has little qualitative impact on burst features for these g_{ca}-values. Once g_{ca} becomes large enough that PP bursting would have occurred in the original model, however, a

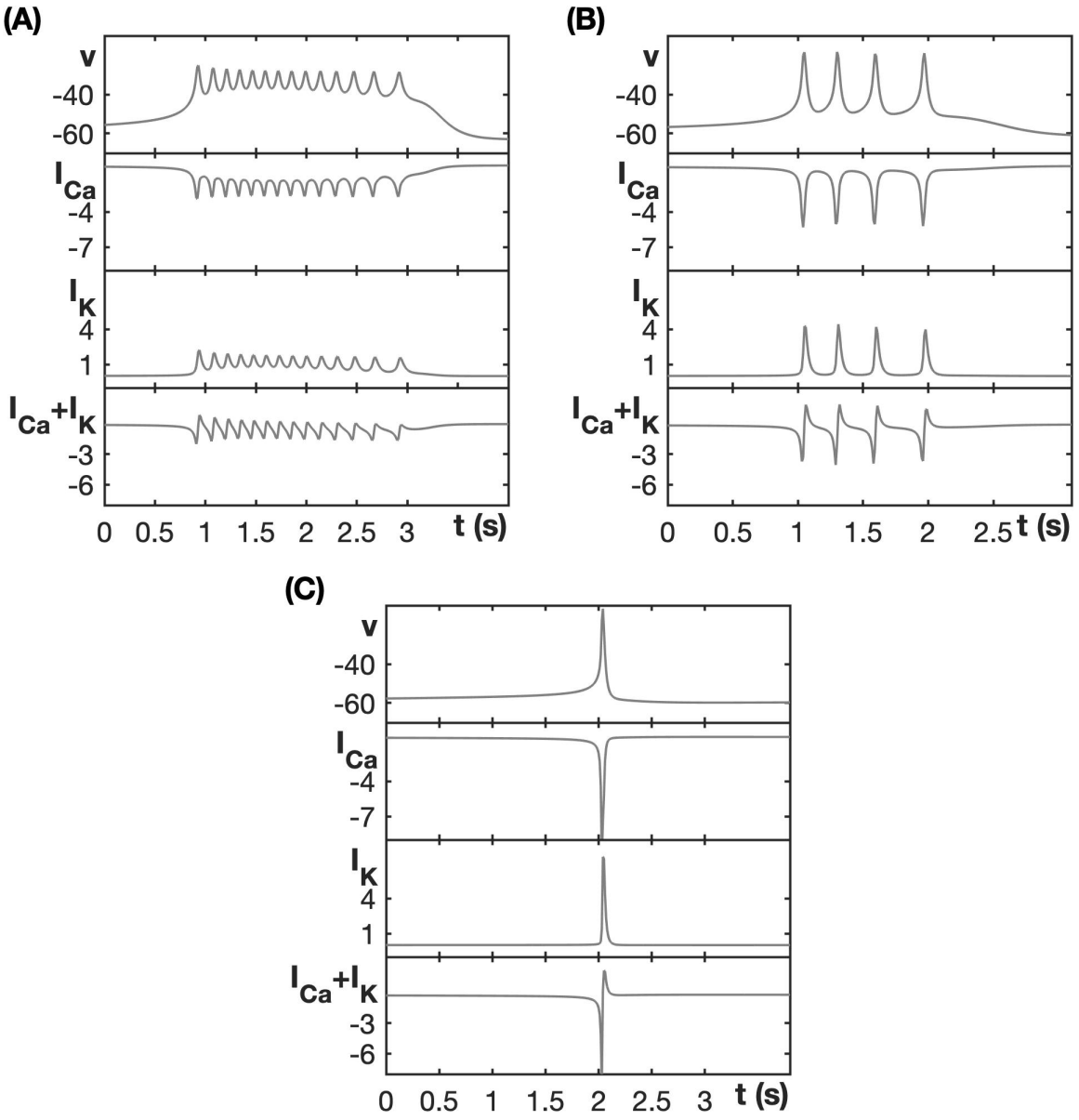

Figure 12: Burst patterns exhibited by the modified generic endocrine model (6)–(7), (14) and (16) for different values of g_{ca}, along with associated currents. (A) SW bursting at $g_{ca} = 0.81$. (B) SW bursting at $g_{ca} = 1.2$. (C) Spiking for $g_{ca} = 2.0$. Note that, as g_{ca} increases, the amplitude of the initial spike increases.

more significant difference emerges (Figure 12C). In this case, the large g_{ca} and corresponding I_{Ca} yield a strong voltage elevation and I_K activation as previously. Now, when the strong I_K activation is combined with h inactivation that weakens I_{Ca}, the outward current overwhelms the inward current, as can be seen from the positive value of $I_K + I_{Ca}$ on the tail end of the spike. Hence, v is pushed down to a hyperpolarized state, and bursting is replaced by the generation of an isolated spike.

2.3.2 Effects of Varying τ_h

As we and many others have discussed [43, 29], bursting in neuronal and endocrine models relies on a balance of voltage-dependent positive and negative feedback contributions to the voltage equation, acting on appropriate timescales. More specifically, consider SW bursting in a model for which the fast inward current does not inactivate. If the conductance of this inward current is increased sufficiently then the strengthened positive feedback disrupts the balance of currents in the system. As a consequence, the slower negative feedback current cannot overcome the fast positive current to induce the downstroke needed for a spike, so the model ceases to exhibit spiking during its active phase and, instead, transitions to a state of depolarization block or a PP burst. Therefore, we hypothesize that the enhancement of SW bursting, and the prevention of PP bursting and depolarization block, can be achieved by modifications to a model in such a way that the balance of currents is maintained as certain parameters vary. We achieved this by adding a slow inactivation gate to a positive current, such that this inward current gradually weakens, even when its maximal conductance g_{ca} or g_{na} is high. In this section, we report on achieving an optimal balance by choosing the most suitable value for τ_h, the time constant for the slow inactivation gate.

Figure 13 shows the burst patterns of the original generic endocrine model (6)–(7) as well as of its modification with (14) and (16) for $g_{ca} = 1.1$ and different values of τ_h. When $g_{ca} = 1.1$, the original model, without inactivation of the Ca^{2+}-channel, exhibits SW bursting (Figure 13A); this corresponds to setting $\tau_h = \infty$, with $h \equiv 1$ constant, in the modified generic endocrine model. Note that the value $g_{ca} = 1.1$ is at the top end of the g_{ca}-range at which the original model can potentially produce SW bursting (cf. Figure 4). We now

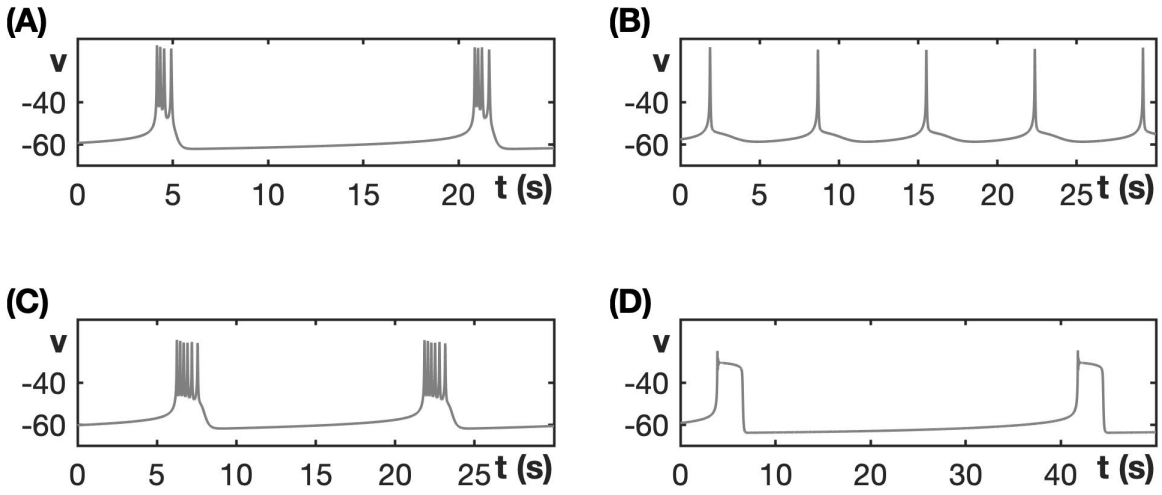

Figure 13: Activity patterns exhibited by the modified generic endocrine model (6)–(7), (14) and (16) at $g_{ca} = 1.1$ with τ_h varying. (A) SW bursting for the original model, which is equivalent to the modified model with $\tau_h = \infty$ and $h \equiv 1$. (B) Slow spiking for $\tau_h = 0.2$. (C) SW bursting for the default value $\tau_h = 0.03$. (D) PP bursting for $\tau_h = 0.01$.

impose dynamics on the inactivation gate to the calcium channel and show how the balance of voltage-dependent positive and negative feedback is controlled by the timescale constant τ_h associated with this inactivation gate.

When $\tau_h = 0.2$ (Figure 13B), the dynamics of h is not fast enough during the first spike to cause any spike attenuation. Hence, v reaches a level at which the outward current I_K turns on to full strength. As the spike terminates, the combination of the small decrease in h and corresponding decrease in I_{Ca} together with the strong I_K result in a net outward current flow that pulls the voltage back down out of the active phase into a full after-hyperpolarization. Thus, when the inactivation is slow, SW bursting is replaced by slow spiking.

Decreasing τ_h to the default value $\tau_h = 0.03$ for the modified model (as used in Figure 10A) corresponds to a faster, although still slow, rate of change of h. In this case, h reduces fast enough that the amplitude of the first spike is lowered, as seen in Figure 13C; indeed, notice that the spikes max out at a lower voltage than in Figure 13A,B. The reduced maximal voltage leads to a weaker I_K activation, which cannot induce a full hyperpolarization

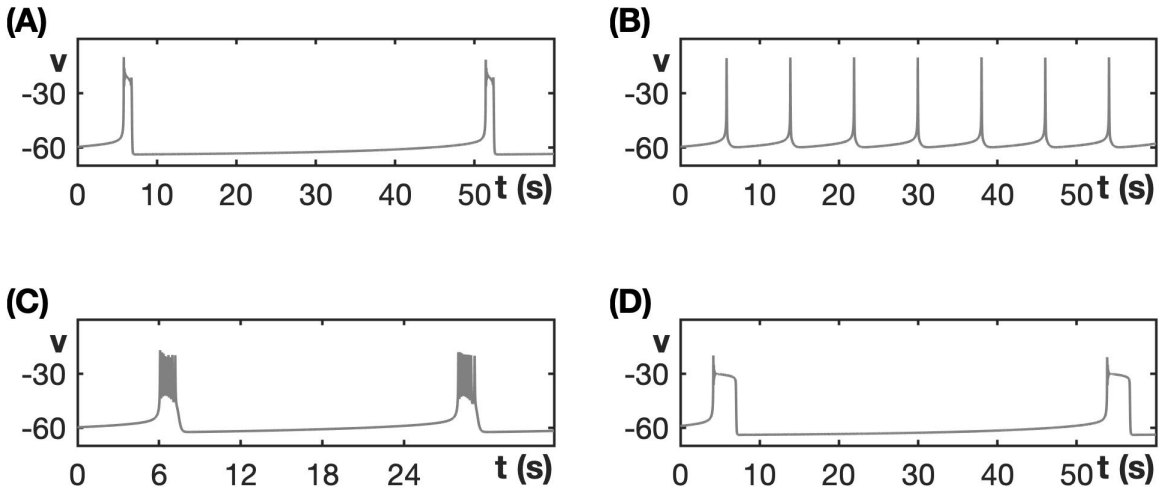

Figure 14: Activity patterns exhibited by the modified generic endocrine model (6)–(7), (14) and (16) at $g_{ca} = 1.5$ with τ_h varying. (A) PP bursting for the original model, which is equivalent to $\tau_h = \infty$ and $h \equiv 1$. (B) Slow spiking for $\tau_h = 0.2$. (C) SW bursting for $\tau_h = 0.02$. (D) PP bursting for $\tau_h = 0.015$.

or return to the silent phase. Hence, additional spikes occur, even though h is gradually decreasing, resulting in a spiking active phase and restoration of a SW bursting pattern.

Decreasing τ_h further, however, accelerates the I_{Ca} inactivation rate, which means that the amplitude of the first voltage peak is lowered even more and, consequently, I_K activation is significantly weakened. Eventually, the outward I_K current is not strong enough to pull down the voltage and form a spike. This effect corresponds to convergence to the depolarized (upper) branch of the critical manifold. Hence, voltage jumps up to the branch of $\mathcal{C}$ with stable equilibria of the fast subsystem, which leads to transient depolarization block and the emergence of PP bursting patterns (e.g., Figure 13D for $\tau_h = 0.01$), or else sustained depolarization block.

If we now increase g_{ca} to $g_{ca} = 1.5$ then the original generic endocrine model (6)–(7) exhibits PP bursting (cf. Figure 4); the burst pattern is shown in Figure 14A, with the other panels illustrating burst patterns for the modified generic endocrine model (6)–(7), (14) and (16) with $g_{ca} = 1.5$ and different values of τ_h. We select $\tau_h = 0.2$ (Figure 14B), $\tau_h = 0.02$

(Figure 14C), and $\tau_h = 0.015$ (Figure 14D), which produce a sequence of patterns that suggest a similar transition from spiking via SW bursting to PP bursting (cf. Figure 13), even though the original model exhibits only PP bursting at this higher g_{ca}-value. The explanation is entirely analogous to that detailed for Figure 13; for example, when $\tau_h = 0.2$, the inactivation gate is very slow and h does not change enough during the first spike to cause any reduction in peak spike amplitude. With the slow inactivation of I_{Ca}, however, the resulting increase in I_K is strong enough to pull the voltage back to full hyperpolarization after the first spike.

We observe the same effect when varying τ_h for different choices of g_{na} in the modified sodium-potassium minimal model and for different choices of g_{ca} in the modified Chay-Keizer model. In other words, for all three modified models, there exists an intermediate range of τ_h-values for which the SW burst regime is significantly extended into higher values for g_{ca} or g_{na} and PP bursting is prevented. Figure 15 illustrates this enlarged robustness with two-parameter bifurcation diagrams of all three modified models that show the regimes for different activity patterns with respect to the conductance of the fast inward current, g_{ca} or g_{na}, and $1/\tau_h$. We use the inverse $1/\tau_h$ rather than τ_h itself so that the activity patterns of the original generic endocrine model (6)–(7) and the original sodium-potassium minimal model (8)–(9) appear on the line $1/\tau_h = 0$. For the minimal Chay–Keizer model (10)–(11), the inclusion of $h_\infty(v)$ in I_{Ca} corresponds to an instantaneous negative feedback component of this current. Therefore, this model is represented as $1/\tau_h = \infty$ ("inf") in Figure 15C.

For each fixed value of τ_h, the activity patterns exhibited by the modified models were analyzed by considering two-parameter bifurcation diagrams with respect to the fast inward current conductance parameter and the slow variable, as in earlier figures (e.g., Figure 4). In each panel, the grey shaded region corresponds to SW bursting or fast spiking patterns, both of which would yield synaptic transmission. Fast spiking is exhibited by the modified sodium-potassium minimal model (8)–(9), (15)–(16) for τ_h values above 11 and sufficiently large g_{na}. In this case, the full model has a stable periodic orbit with $s \approx 1$; for example, see Supplemental Figure 47. Observe that, for all three modified models, the largest interval of conductances that spans this region occurs at the cross-section for an intermediate value of $1/\tau_h$ (and, thus, of τ_h). Indeed, for Figures 10, 11, we selected τ_h values near the

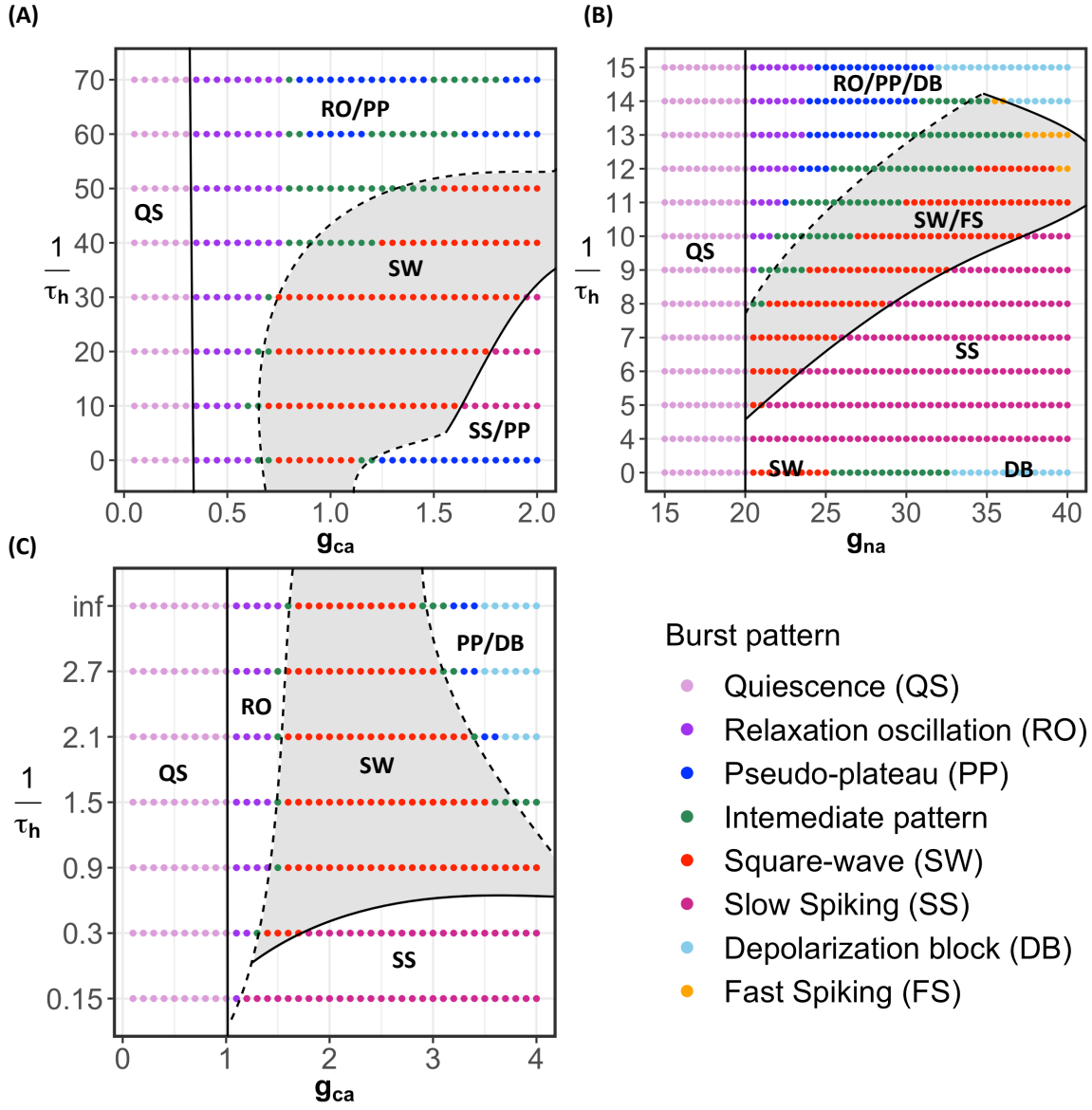

Figure 15: Two-parameter bifurcation diagrams of the modified models with respect to g_{ca} or g_{na} and $1/\tau_h$. (A) Modified generic endocrine model (6)–(7), (14) and (16). (B) Modified sodium-potassium minimal model (8)–(9) and (15)–(16). (C) Modified minimal Chay–Keizer model (10)–(11) and (16)–(17). Notice that in all the three modified models, SW is most robust over an intermediate range of $1/\tau_h$-values (and, hence, of τ_h-values).

optimum for each model. When τ_h is sufficiently small, all three modified models exhibit relaxation oscillations that transition to PP bursting as the fast inward current conductance is increased. From there, as τ_h is made larger, an interval of conductances that support SW bursting emerges and grows (Figure 15A–C) and PP bursting, over a large range of τ_h, is prevented.

We remark that the analysis of the corresponding bursting patterns for most of the range of τ_h-values considered can be done by assuming that the model has three fast and one slow variables. However, at sufficiently large values of τ_h, the timescale of h becomes comparable to that of the slow variable, which means that the models should be analyzed as systems with two fast and two slow variables. Our numerical explorations for each of the three modified models suggest that on the intermediate range of τ_h that extends the SW regime, τ_h does not yet become comparable to the timescale of the slow variable. We leave a more detailed multi-timescale analysis of the regime of large τ_h for future work.

2.3.3 Varying g_k

Varying the parameter g_k changes the timescale of v but leaves the timescales of the other variables unchanged (see the Appendix). Hence, the modified models can be analyzed for varying g_k by considering a fast-slow decomposition with three fast and one slow variables, as long as v remains fast, and also τ_h for each modified model is chosen such that the h-kinetics evolves at a significantly faster timescale than that of the slowest variable in the corresponding original model.

For a general SW bursting model, a reduction of g_k leads to a transition from SW bursting to a PP pattern; qualitatively, it has the same impact as increasing g_{na} or g_{ca} [86]. Therefore, we expect that the robustness of SW bursting with respect to changes in g_k is maximal for the modified models if τ_h is chosen from an intermediate range. This is confirmed in Figure 16, where we show two-parameter bifurcation diagrams in the $(g_k, 1/\tau_h)$-plane for each of the modified models.

Supplementary Figure 49 shows the two-parameter bifurcation diagram of the butera model (12)-(13) with respect to g_k. Notice that the model exhibits SW bursting for a large

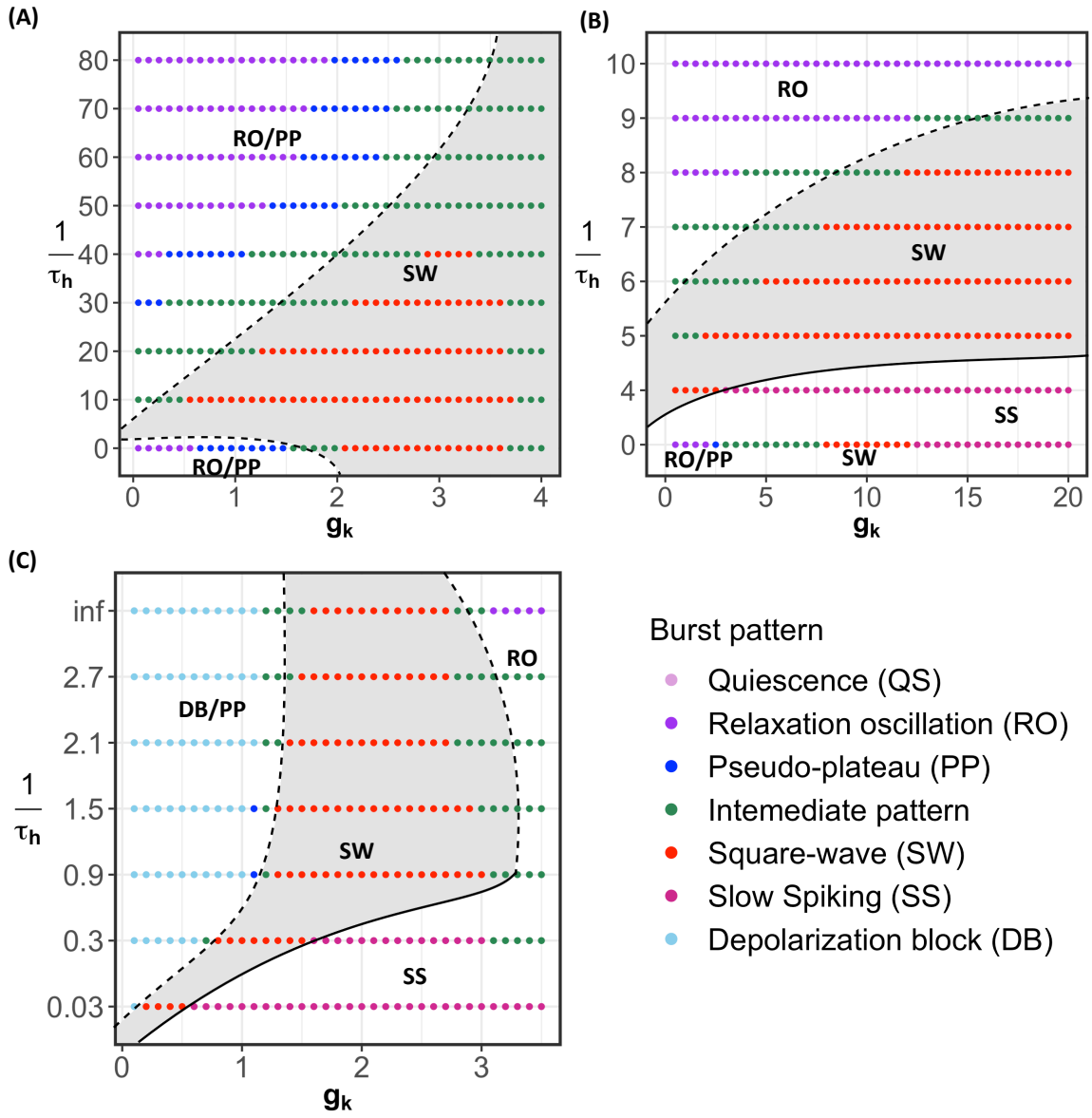

Figure 16: Two-parameter bifurcation diagrams of the modified models with respect to g_k and $1/\tau_h$. (A) Modified generic endocrine model (6)–(7), (14) and (16). (B) Modified sodium-potassium minimal model (8)–(9) and (15)–(16). (C) Modified minimal Chay–Keizer model (10)–(11) and (16)–(17).

range of g_k values. Figure 16A corresponds to the modified generic endocrine model (6)–(7), (14) and (16). Notice that in the original model, without inactivation (i.e., $1/\tau_h = 0$), the burst pattern transitions to PP (blue dots) as g_k decreases below $g_k \approx 1.7$. Over a range of $1/\tau_h$-values that are neither too large nor too small, this transition is completely prevented. The modified sodium-potassium minimal model (8)–(9) and (15)–(16) in Figure 16B yields a qualitatively similar result. Recall that the original minimal Chay–Keizer model (10)–(11), with its instantaneous I_{Ca} inactivation gate, corresponds to $1/\tau_h = \infty$ ("inf") in Figure 16C; the burst pattern transitions to depolarization block (light blue) as g_k decreases, via only a very small interval of PP activity. The modified minimal Chay–Keizer model with additional equations (16)–(17) maintains this property for large $1/\tau_h$-values, but the transition via PP to depolarization block is prevented over a much larger range of g_k for an intermediate interval of $1/\tau_h$-values.

2.3.4 Effect of slow negative feedback on the location of AH

The additional inactivation gate and associated h-dynamics affect the location of the critical manifold for the fast subsystem (2), but this location change does not fully explain the increased robustness seen at intermediate values of the timescale constant τ_h. For example, consider the modified generic endocrine model (6)–(7), (14) and (16) for the default parameters as given in Tables 1, with various choices of τ_h. Provided that τ_h remains small enough, e.g., $\frac{1}{\tau_h} > 10$, the modified model has three fast variables (v, n and h) and one slow variable (c). Then the critical manifold is defined implicitly by the equation:

$$\begin{aligned} I_{Ca}(v, h_\infty(v)) + I_K(v, n_\infty(v)) & \\ +I_{K(Ca)}(v, c) &= 0, \end{aligned} \tag{18}$$

with $n = n_\infty(v)$ and $h = h_\infty(v)$. Hence, the critical manifold does not depend on τ_h at all. Similarly, the saddle-node bifurcations LSN and USN, which are determined by the local minima and maxima of (18), respectively, when viewed as a curve in the (v, c)-plane, do not depend on τ_h. However, the Jacobian matrix of the full four-dimensional system, evaluated along the critical manifold, does depend on τ_h; this means, in particular, that the location of the Andronov–Hopf bifurcation (AH) is potentially affected by variations in τ_h.

For example, consider an equilibrium of the fast subsystem that lies on the upper, high-voltage branch $\mathcal{C}_A$ of the critical manifold on the part that coexists with $\mathcal{C}_M$ and (part of) $\mathcal{C}_S$; hence, its c-coordinate satisfies $c_{\mathsf{LSN}} \leq c \leq c_{\mathsf{USN}}$. Figure 17 shows how the real parts of a pair of complex-conjugate eigenvalues for this equilibrium point change with $1/\tau_h$ for fixed $g_{ca} = 0.81$. As can be seen from the figure, for relatively small τ_h values (i.e., for large $1/\tau_h$), the equilibrium is stable. That is, the Andronov–Hopf bifurcation, denoted AH here, that stabilizes points on $\mathcal{C}_A$ occurs at a c-value above the c-coordinate of this equilibrium point. On the other hand, as τ_h becomes larger, corresponding to a slower negative feedback, the equilibrium becomes unstable. In this case, the Andronov–Hopf bifurcation point AH must occur at a lower c value than that of this equilibrium point. For a model to exhibit PP bursting or depolarization block (DB), the point AH must lie at $c > c_{\mathsf{LSN}}$. Increasing τ_h pushes this bifurcation to c values below c_{LSN}; that is, the calcium inactivation must be sufficiently slow to move the Andronov–Hopf bifurcation AH to a location where PP bursting and DB are prevented for this value of g_{Ca}.

2.4 Discussion

In this work, we compared bursting patterns across four well-established, relatively low-dimensional mathematical neuron models of Hodgkin–Huxley type, namely, a generic endocrine model (6)–(7) [88], a sodium-potassium minimal model (8)–(9) [43], a minimal Chay–Keizer model (10)–(11) [70, 69], and the Butera model (12)–(13) [18]. Observing the distinctive robustness of SW bursting in the Butera model, which features a slow inactivation component in the fast inward current that drives spiking, we modified the three other models, which exhibit less robust SW bursting in their original forms. Specifically, we included slow inactivation dynamics in their fast inward currents, and examined the effects on the robustness of their SW bursting dynamics. Previous literature has studied the transition between SW and PP bursting patterns with changes in fast inward current conductances [84, 86, 85, 88, 89]. To our knowledge, however, this is the first time that the effect of slow negative feedback has been studied in relation to the robustness of SW bursting. The

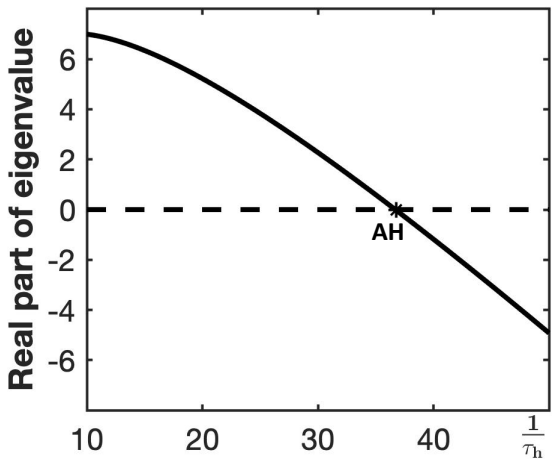

Figure 17: Dependence on τ_h of two complex-conjugate eigenvalues associated with an equilibrium of the fast subsystem with $c > c_{\mathsf{LSN}}$ on the branch $\mathcal{C}_A$ of the critical manifold for the modified generic endocrine model (6)–(7), (14) and (16) with $g_{ca} = 0.81$. Shown are their real parts versus $1/\tau_h$. The stability changes at an Andronov–Hopf bifurcation (AH) for an intermediate value of $1/\tau_h$. Hence, below this value, the system will not exhibit DB or PP bursting.

point of this analysis is not to propose an adjustment to these bursting models; rather, we use the comparison of the original and modified models as a tool to explore the role of the slow inactivation of the inward current. Our results provide insight into why some neurons in biological systems might have slowly inactivating inward currents — despite these seemingly being redundant, because of the presence of outward currents that activate on similar timescales.

We employed standard dynamical systems methods of fast-slow decomposition and bifurcation analysis for this investigation. Our analysis shows that the addition of slow inactivation dynamics expands the ranges of parameter values over which the modified models exhibit SW bursting, while eliminating or curtailing PP bursting, depolarization block, and relaxation oscillations. This finding led us to the novel hypothesis that inward currents featuring slow inactivation should be prevalent for neurons that rely on bursts with spikes for synaptic transmission and the activation of associated calcium currents (e.g., [66]).

The bifurcation techniques and fast-slow analysis used in this work depend heavily on the timescale separation of the variables in these models. We showed that the modified models exhibit optimally robust SW bursting if the timescale constant associated with the inward current inactivation lies in a range that is similar to that of the activation variable for a primary outward current (e.g., I_K). When the slow inactivation is too fast in these relative terms, we observed that the inward current can become too weak to recruit the outward current and induce the corresponding hyperpolarization needed to sustain repeated spiking, in which case patterns such as PP bursting are more likely (e.g., Figure 15A, large $1/\tau_h$). This finding is analogous to the result that a fast-activating negative feedback provided by a BK potassium current promotes PP bursting in pituitary cells [92]. When the slow inactivation is too slow, the inward current can become too strong, so that even with full outward current activation, the cell does not repolarize. Thus, there is a "Goldilocks zone" for tuning the timescale of the inward current inactivation where it is most effective at sustaining spiking and associated synaptic transmission.

We linked these ideas with specific mathematical properties of the models by studying how this inactivation rate affects the stability of equilibria in the fast subsystem at elevated voltage and the location in parameter space of the Andronov–Hopf bifurcation points at

which these equilibria change stability. Here we made use of the fact that there is generally a single slow variable for the considered values or ranges of the relevant system parameters. It remains an interesting subject of future mathematical work to calculate bounds on the optimal range of inactivation timescales for maximal robustness of SW. This will likely require the consideration of parameter ranges where one finds two slow variables, in addition to ranges where there is just one. Another direction for future analysis would be to consider effects on robustness due to variation of other model parameters that are affected by neuromodulation or are relevant to pathologies involving alterations to neural bursting; for example, see [38, 54, 50, 81]).

The values for the half-inactivation parameters v_h and s_h in (16) for the models that we studied were chosen to match analogous values used in other models with inactivation gates for the inward current [18, 70, 69]. Changing these values yields a quantitatively different optimal timescale range over which SW bursting is most robust, but our numerical explorations suggest that this does not change the phenomenon that we revealed (e.g., see Supplemental Figure 50). We considered only four models that were known to exhibit SW bursting, two with a fast inward sodium current and two with a fast inward calcium current. Despite our focus on a small selection of models, the mechanistic aspects of the results that we have explained strongly suggest that our results will naturally generalize beyond these specific examples.

We note that, depending on the location of the slow nullcline, the same fast subsystem bifurcation structure that supports SW bursting can also yield sustained, fast, tonic spiking, depending on the position of the slow nullcline (e.g., Supplemental Figures 47, 48). However, we found that the occurrence of this type of spiking is quite rare in the models that we studied, although it does show up in one case (Fig. 15 B, orange dots). In other models that include a slow negative feedback on the fast inward current, SW bursting could be lost to this fast spiking more commonly under parameter variation. In a CPG circuit, however, this activity could serve a similar function as SW bursting. To see this, suppose that two or more intrinsically spiking neurons are coupled by synaptic inhibition and one is actively spiking, leading to the inhibition of the others. If one of these other neurons becomes active, such as through recovery from adaptation, and starts spiking, then it could inhibit and shut

off the formerly spiking neuron. When this process occurs repeatedly, it results in bursting spike patterns (cf. [73]). Interestingly, CPG circuits with reciprocal inhibition can exhibit phase transitions based on a release mechanism, controlled by neurons in the active phase, or an escape mechanism, controlled by neurons in the silent phase. In the former case, the synaptic threshold is likely to be elevated, such that spiking is important for circuit oscillation properties, whereas in the latter case, the synaptic threshold is likely to be lower, such that the presence of spikes within each phase of depolarized membrane potential becomes less important [74]; hence, our work suggests that the presence of inward currents with slow inactivation might be an indicator that a circuit operates in release mode.

Ideally, in future work, a more general theory can be developed that will cast our results in terms of assumptions on a general Hodgkin–Huxley type model. For the time being, we can at least observe that the results of this study are consistent with past work on neuronal bursting [43] in that we also find that, for a neuron with slow inward current inactivation, it is not important whether sodium or calcium ions are carried in this current. Interestingly, however, a key prediction emerges: fast currents with slow inactivation, which are usually sodium currents, will represent the dominant, fast inward current in rhythmic neurons for which spiking is important; non-inactivating sodium currents and calcium currents or the presence of fast negative feedback [92], on the other hand, will tend to be associated with neurons for which spiking is less important than simple depolarization. Correspondingly, in neurons for which function is unknown, the characterization of the dominant, fast inward current gives us a prediction about the importance of spiking for these cells.

3.0 Ramping dynamics in neurons of the pre-Bötzinger Complex [1]

3.1 Introduction

Respiration is a rhythmic activity that has three phases: inspiration, post-inspiration, and late-expiration. Among these phases, the inspiratory output is primarily determined by the activity of the pre-Bötzinger complex (pre-BötC) located in the brain stem [78, 19, 47]. Experimental results show that the neurons in pre-BötC often exhibit bursting patterns characterized by an increase in spike frequency during the active phase, accompanied by a gradual rise in the underlying plateau potential (See Figure 18A). The burst begins with slow tonic oscillations during the pre-inspiratory phase. As the burst progresses into the inspiratory phase, the spike frequency increases while the hyperpolarization between spikes weakens [3]. However, many existing respiratory mathematical models fail to capture this "ramping effect" observed in bursting neurons. (See Figure 18B)

[3] shows that modifying existing pre-BötC model with potassium ion concentration dynamics produces ramping effect. However, in this model, the ramping dynamics occur within a narrow region of the parameter space. We aim to show the ramping effect by incorporating a second slow inactivation component associated with the inward sodium current. In this project, we develop two phenomenological models that exhibit ramping bursts. Through these models, we present two mechanisms that help control burst shape and spike frequency - (1) a slow potassium current that controls the strength of hyperpolarization after each spike and (2) a slow sodium current that controls the spike height in burst. Based on the observations from these models, we develop and analyze a more biologically relevant model that exhibits bursts with the ramping pattern. We show that adding an additional slow inactivation gate to the sodium current of existing pre-BötC neuronal model produces ramping dynamics. We use dynamical systems methods such as bifurcation analysis and phase plane analysis to study the various activity patterns exhibited by the model when parameter values change. Using these methods, we explain the mechanisms that give rise to the observed

[1] Collaborator : Dr. Ryan Phillips, Seattle Children's Research Institute

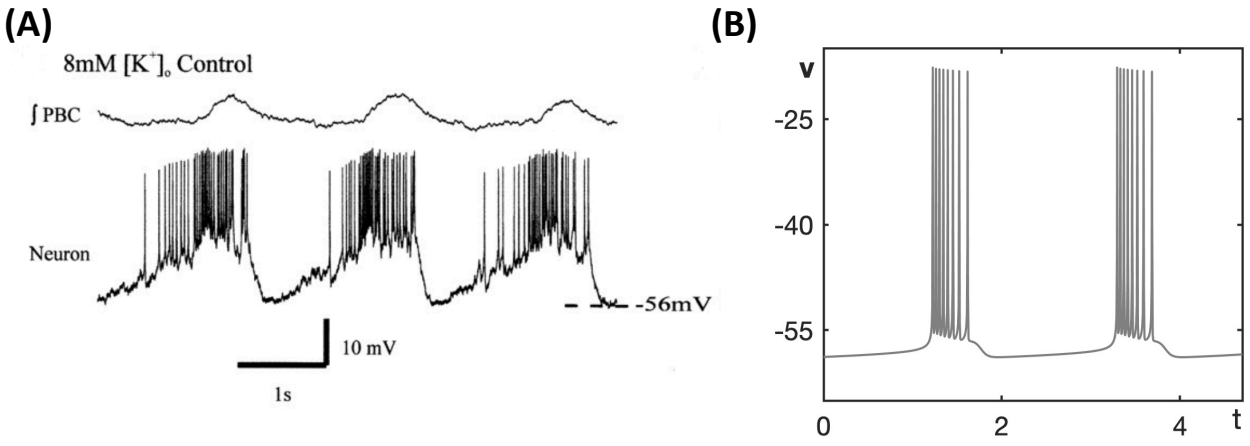

Figure 18: (A) Ramping burst pattern exhibited by the inspiratory pacemaker neurons for external potassium concentration $[K^+]_o$ = 8mM. This figure was reprinted from Tryba, A. K., Peña, F., & Ramirez, J. M. (2003). Stabilization of bursting in respiratory pacemaker neurons. *The Journal of Neuroscience*, 23(8), 3538–3546. https://doi.org/10.1523/JNEUROSCI.23-08-03538.2003 [87]. Copyright [2003] Society for Neuroscience. (B) The bursting pattern exhibited by the model for inspiratory neurons presented in [4].

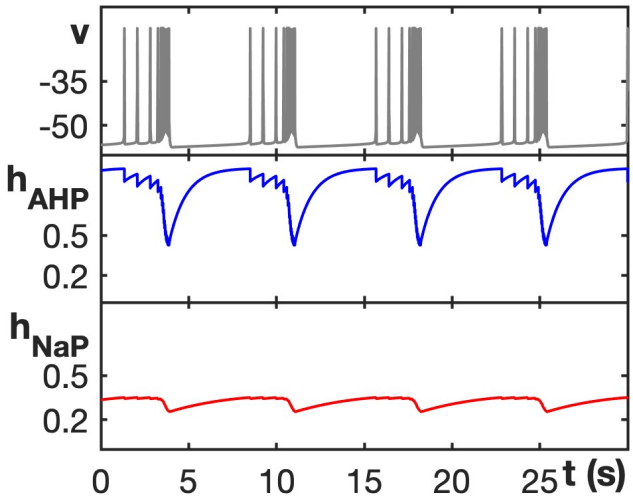

Figure 19: Ramping burst pattern exhibited by the AHP model (19)-(21) for default parameter values given in Table 6

ramping bursting pattern.

3.2 AHP model

We modified the model presented in [4] by introducing an additional slowly inactivating potassium current, denoted as I_{AHP}, to the model. This current decreases during the burst, thereby reducing the strength of the hyperpolarization after each spike, while simultaneously increasing the spike frequency, generating the ramping bursting pattern illustrated in the Figure 19.

The model dynamics are defined by the following equations :

$$\begin{cases} cv' &= -(I_{Na}(v,h_{Na},m_{Na}) + I_K(v,n) + I_{NaP}(v,h_{NaP},m_{NaP}) \\ & \quad + I_{AHP}(v,h_{AHP},m_{AHP}) + I_L(v) + I_{syn}(v)), \\ h'_{Na} &= (h_{Na\infty}(v) - h_{Na})/\tau_{h_{Na}}(v), \\ m'_{Na} &= (m_{Na\infty}(v) - m_{Na})/\tau_{m_{Na}}(v), \\ h'_{AHP} &= (h_{AHP_\infty}(v) - h_{AHP})/\tau_{h_{AHP}}(v), \\ m'_{AHP} &= (m_{AHP\infty}(v) - m_{AHP})/t_{m_{AHP}}(v), \\ h'_{NaP} &= (h_{NaP\infty}(v) - h_{NaP})/\tau_{h_{NaP}}(v), \\ m'_{NaP} &= (m_{NaP\infty}(v) - m_{NaP})/\tau_{m_{NaP}}(v), \\ n' &= (n_\infty(v) - n)/\tau_n(v) \end{cases} \tag{19}$$

where I_{Na} is the fast sodium current with activation variable m_{Na} and inactivation variable h_{Na}, I_{NaP} is the persistent sodium current with activation variable m_{NaP} and inactivation variable h_{NaP}, I_K is the delayed rectifier potassium current with activation gate variable n, I_L denotes the leak current and I_{syn} is the synaptic current. The constructed I_{AHP}, or after-hyperpolarization current has activation variable m_{AHP} and slow inactivation variable h_{AHP}.

The expressions for the currents in (19) are given by:

$$\begin{aligned} I_{Na}(v,h_{Na},m_{Na}) &= g_{Na}\, m_{Na}^3\, h_{Na}\, (v - e_{Na}), \\ I_K(v,n) &= g_k\, n^4\, (v - e_K), \\ I_{NaP}(v,h_{NaP},m_{NaP}) &= g_{NaP}\, h_{NaP}\, m_{NaP}\, (v - e_{Na}), \\ I_{AHP}(v,h_{AHP},m_{AHP}) &= g_{AHP}\, m_{AHP}\, h_{AHP}\, (v - e_K), \\ I_L(v) &= g_L\, (v - e_L), \\ I_{syn}(v) &= g_{syn}\, (v - e_{syn}), \end{aligned} \tag{20}$$

The steady state activation functions in (19) are given by:

$$
\begin{aligned}
h_{Na\infty}(v) &= (1+e^{-(v_{h_{Na}}+v)/s_{h_{Na}}})^{-1}, \\
\tau_{h_{Na}}(v) &= t_{h_{Na}}\ \cosh((k_{h_{Na}}+v)/p_{h_{Na}})^{-1}, \\
m_{Na\infty}(v) &= (1+e^{-(v_{m_{Na}}+v)/s_{m_{Na}}})^{-1}, \\
\tau_{m_{Na}}(v) &= t_{m_{Na}}\ \cosh((k_{m_{Na}}+v)/p_{m_{Na}})^{-1}, \\
h_{AHP\infty}(v) &= (1+e^{-(v_{h_{AHP}}+v)/s_{h_{AHP}}})^{-1}, \\
\tau_{h_{AHP}}(v) &= t_{h_{AHP}}\ \cosh((k_{h_{AHP}}+v)/p_{h_{AHP}})^{-1}, \\
m_{AHP\infty}(v) &= (1+e^{-(v_{m_{AHP}}+v)/s_{m_{AHP}}})^{-1}, \\
h_{NaP\infty}(v) &= (1+e^{-(v_{h_{NaP}}+v)/s_{h_{NaP}}})^{-1}, \\
\tau_{h_{NaP}}(v) &= t_{h_{NaP}}\ \cosh((k_{h_{NaP}}+v)/p_{h_{NaP}})^{-1}, \\
m_{NaP\infty}(v) &= (1+e^{-(v_{m_{NaP}}+v)/s_{m_{NaP}}})^{-1}, \\
\tau_{m_{NaP}}(v) &= t_{m_{NaP}}\ \cosh((k_{m_{NaP}}+v)/p_{m_{NaP}})^{-1}, \\
k_1(v) &= (0.011*(44.0+v))(1-e^{(-44.0-v)/5.0})^{-1}, \\
k_2(v) &= 0.17*e^{(-v-49.0)/40.0}, \\
n_\infty(v) &= k_1(v)(k_1(v)+k_2(v))^{-1}, \\
\tau_n(v) &= (k_1(v)+k_2(v))^{-1}
\end{aligned}
\tag{21}
$$

The default parameter values used in the AHP model (19)-(21) are given in Table 6.

Non-dimensionalization shows that variables h_{NaP} and h_{AHP} change at a significantly slower timescale compared to the other variables in the model. Hence, this model can be analyzed with h_{NaP} and h_{AHP} being considered as slow variables (slow subsystem), while all the other variables can be regarded as fast variables (fast subsystem). We can use fast-slow systems methods, such as bifurcation analysis, to study this model.

It is seen in Figure 19 that h_{AHP} slowly reduces during the burst. As first step towards understanding the ramping dynamics, we begin by analyzing the activity patterns exhibited by the AHP model at various h_{AHP} levels (See Figure 20). When h_{AHP} is fixed at 1, the model exhibits tonic spiking. However, when h_{AHP} reduces, the strength of the outward current I_{AHP} also reduces and it is not strong enough to fully hyperpolarize the voltage. This leads to more spikes and tonic spiking transitions to bursting. When h_{AHP} is reduced further, I_{AHP} decreases even more, resulting in weaker hyperpolarizations between spikes

Table 5: Default parameter values for AHP model (19)-(21) :

g_{Na}	150.0 nS	g_{NaP}	3.0 nS	g_K	220.0 nS
g_{syn}	0.285 nS	e_{Na}	55.188 mV	e_K	−69.829 mV
e_{syn}	−10.0 mV	c	36.0 pF	$v_{h_{Na}}$	67.5 mV
$k_{h_{Na}}$	67.5 mV	$p_{h_{Na}}$	−12.8 mV	$v_{h_{NaP}}$	60.0 mV
$k_{h_{NaP}}$	60.0 mV	$p_{h_{NaP}}$	9.0 mV	$v_{h_{AHP}}$	27.5 mV
$k_{h_{AHP}}$	60.0 mV	$p_{h_{AHP}}$	8.43 mV	$v_{m_{Na}}$	43.8 mV
$k_{m_{Na}}$	43.8 mV	$p_{m_{Na}}$	14.0 mV	$v_{m_{NaP}}$	47.1 mV
$k_{m_{NaP}}$	47.1 mV	$p_{m_{NaP}}$	6.2 mV	$v_{m_{AHP}}$	27.5 mV
$t_{h_{Na}}$	8.46 mS	$t_{h_{NaP}}$	5000.0 mS	$t_{m_{Na}}$	0.25 mS
g_L	4.0 nS	e_L	−62.587 mV	$s_{h_{Na}}$	−11.8 mV
$s_{h_{NaP}}$	−9.0 mV	$s_{h_{AHP}}$	−1.0 mV	$s_{m_{Na}}$	6.0 mV
$s_{m_{NaP}}$	3.1 mV	$s_{m_{AHP}}$	1.0 mV	$t_{m_{NaP}}$	1.0 mS
$t_{h_{AHP}}$	1000.0 mS	$t_{m_{AHP}}$	5.0 mS		

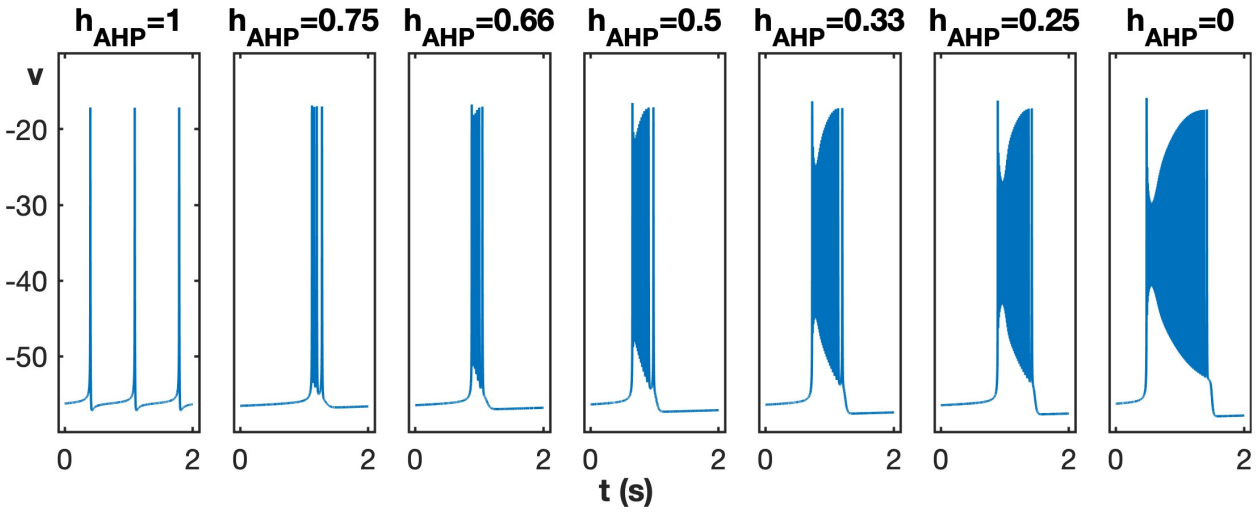

Figure 20: The activity patterns exhibited by the AHP model (19)-(21) for different fixed h_{AHP} values.

and an increase in the number of spikes within the burst. These transitions are shown in Figure 20.

Next, we study the fast subsystem and analyze how the activity patterns change for changing h_{AHP} using h_{NaP} as the bifurcation parameter. Shown in Figure 21A, B, C are the one parameter bifurcation diagrams of the fast subsystem with respect to h_{NaP} for different values of h_{AHP}. The spiking trajectory is overlaid in each figure, depicted in grey. The attractors of the fast subsystem are the stable equilibrium points, colored red, and the stable periodic orbits, colored green, respectively. Since, h_{NaP} evolves at a slower rate compared to the fast variables, the trajectory will always move rapidly towards the fast subsystem attractors. Once on these attractors, it will follow the slow variable nullcline. Hence, h_{NaP} drifts to the right if it is below the nullcline (dashed black curve) and drifts to the left if it is above the nullcline. When h_{AHP}=1 in Figure 21A, we have a SNIC bifurcation and the stable oscillations end at the saddle node. The trajectory in this case stabilizes to the periodic orbit at the SNIC. This is because there is zero net drift in h_{NaP} along this orbit. However, when h_{AHP} reduces (Figure 21B,C, first notice that the homoclinic point (h_{NaP}=h_{HC}) shifts more

to the left of the saddle node (h_{NaP}=h_{SN})and there are stable oscillations for $h_{NaP} < h_{SN}$. Second, the reduction in h_{AHP} also reduced the amplitude of oscillations and the stable oscillations are mostly above the h_{NaP} nullcline. Hence, h_{NaP} drifts to the right on the lower stable branch of the v-nullcline since its below the h_{NaP} nullcline. Once it hits the saddle node, its quickly attracted to top branch of the v-nullcline with stable periodic orbits where overall drift of h_{NaP} is to the left. The oscillations end at the homoclinic point and falls back to the lower stable branch of the v-nullcline giving a burst.

The one parameter bifurcation diagrams shown in Figure 21A, B, C are summarized in the two-parameter bifurcation diagram of the fast subsystem with respect to h_{NaP} and h_{AHP} (Figure 21D). The ramping burst trajectory is overlaid in grey. The burst starts with slow tonic spiking corresponding to high h_{AHP} value (black asterisks). When h_{AHP} reduces, it transitions to a fast spikes on the top branch of the v-nullcline. It eventually hits the homoclinic curve (red asterisks) and fall to the lower branch of the v-nullcline. It traverses this branch till it hits the saddle node (black asterisks again), loses stability and jumps to the upper branch to start oscillations again.

3.3 SPK model

In the model presented in this section, we use a contrasting concept in comparison to the AHP model. Here, we modify the bursting model in [4] with an additional slowly inactivating sodium current, which we call I_{SPK}.

The equations of the model are :

$$\begin{cases} cv' &= -(I_{Na}(v,h_{Na},m_{Na}) + I_K(v,n) + I_{NaP}(v,h_{NaP},m_{NaP}) \\ & \quad + I_{SPK}(v,h_{SPK},h_{2SPK},m_{SPK}) + I_L(v) + I_{syn}(v)), \\ h'_{SPK} &= (h_{SPK\infty}(v) - h_{SPK})/t_{h_{SPK}}, \\ h'_{2SPK} &= (h_{2SPK\infty}(v) - h_{2SPK})/\tau_{h_{2SPK}}(v), \\ m'_{SPK} &= (m_{SPK\infty}(v) - m_{SPK})/t_{m_{SPK}}, \end{cases} \tag{22}$$

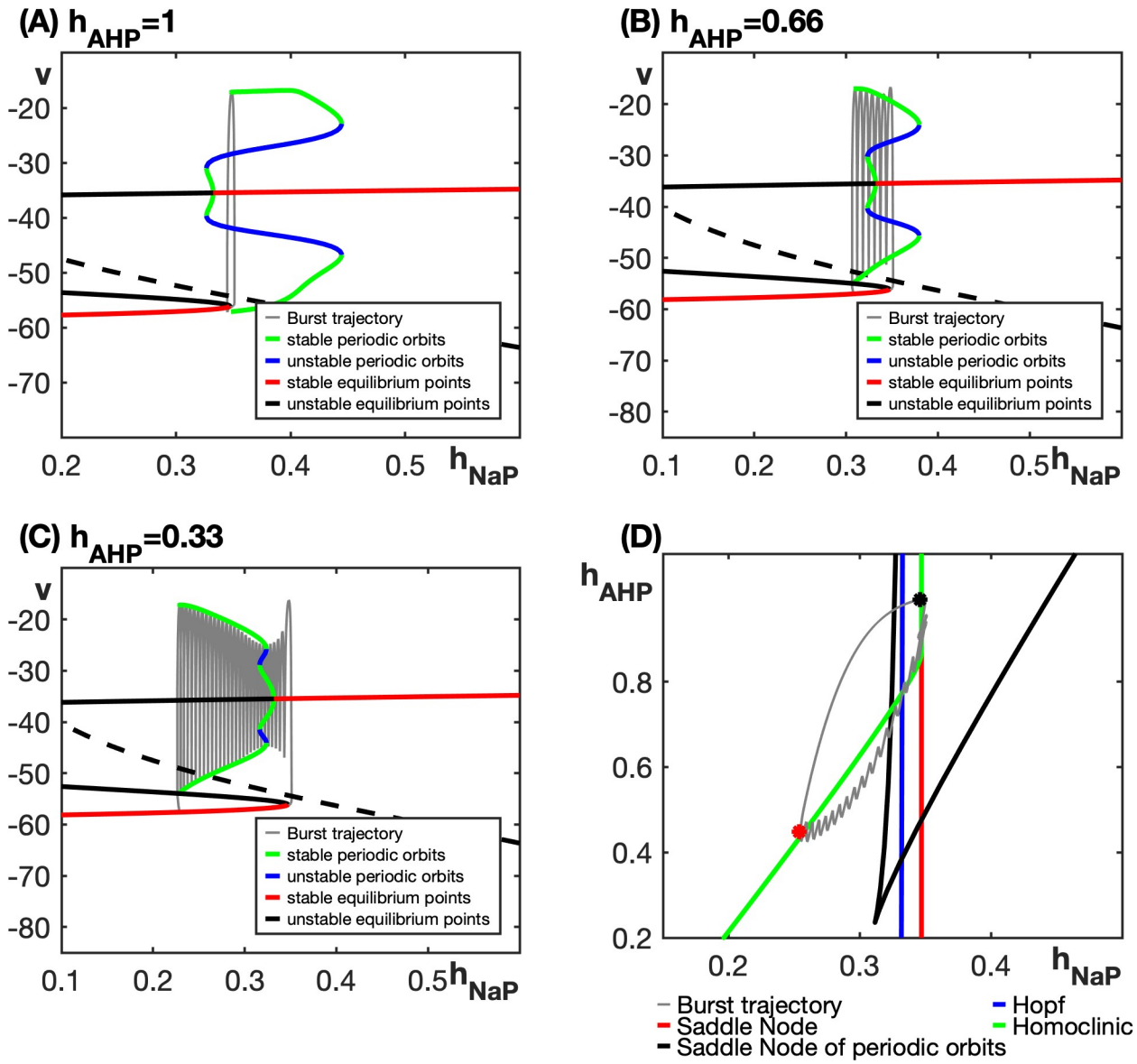

Figure 21: (A)-(C) Bifurcation diagrams of fast subsystem of the AHP model (19)-(21) with respect to h_{NaP} for different values of h_{AHP}. (A) h_{AHP}=1 (B) $h_{AHP} = 0.66$ (C) $h_{AHP} = 0.33$ (D) The two-parameter bifurcation diagram of fast subsystem of the AHP model (19)-(21) with respect to h_{NaP} and h_{AHP}.

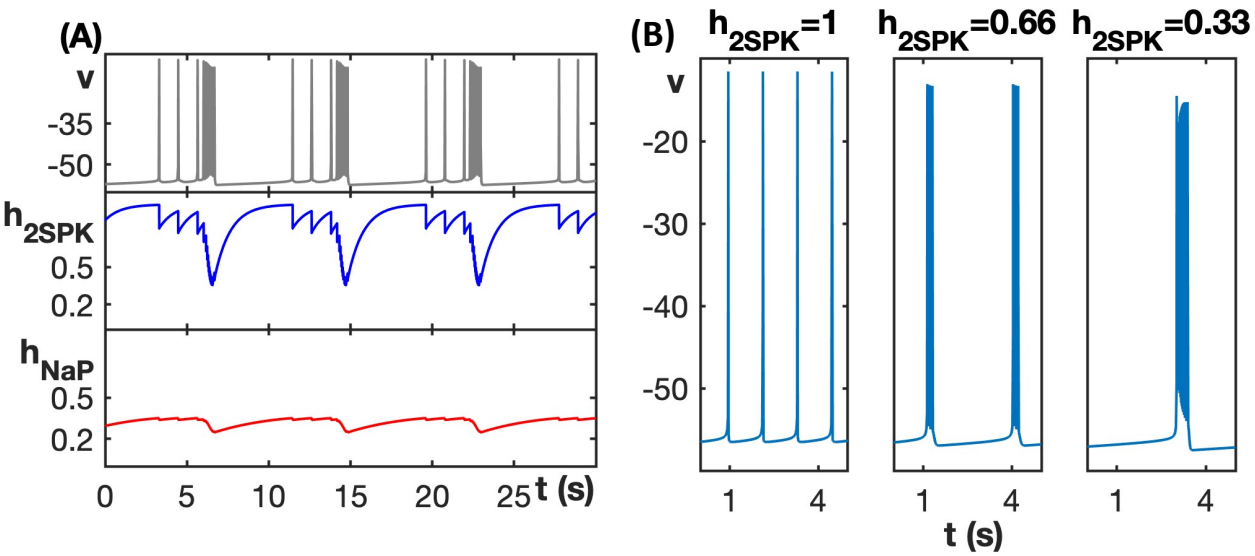

Figure 22: (A) Ramping burst pattern exhibited by the SPK model (22), (23) for default parameter values given in Table 5 (B) The activity patterns exhibited by the SPK model for different fixed h_{SPK} values.

where the I_{SPK}, or the spike current has an activation variable m_{SPK} as well as two inactivation variables h_{SPK}, which evolves at a fast timescale, and h_{2SPK}, which inactivates at a slower rate. The fast inactivation of sodium current is needed to terminate the spikes and to produce bursting pattern while h_{2SPK} is an additional slow inactivation gate we added to help shape the burst pattern. The equations for $h_{Na}, m_{Na}, h_{NaP}, m_{NaP}$ and n are same as the AHP model.

The expressions for the currents and activation functions in (22) are given by:

$$\begin{aligned} I_{SPK}(v, h_{SPK}, h_{2SPK}, m_{SPK}) &= g_{SPK}\, m_{SPK}\, h_{SPK}\, h_{2SPK}\, (v - e_K), \\ h_{SPK_\infty}(v) &= (1 + e^{-(v_{h_{SPK}} + v)/s_{h_{SPK}}})^{-1}, \\ h_{2SPK_\infty}(v) &= (1 + e^{-(v_{h_{2SPK}} + v)/s_{h_{2SPK}}})^{-1}, \\ \tau_{h_{2SPK}}(v) &= t_{h_{2SPK}}\, \cosh((k_{h_{2SPK}} + v)/p_{h_{2SPK}})^{-1}, \\ m_{SPK_\infty}(v) &= (1 + e^{-(v_{m_{SPK}} + v)/s_{m_{SPK}}})^{-1}, \end{aligned} \tag{23}$$

All the other currents and activation functions are the same as the AHP model. The default parameter values are given in Table 5 for which the SPK model (22),(23) exhibits the ramping pattern shown in Figure 22A.

In the SPK model we added a slowly inactivating sodium current I_{SPK}. The h_{2SPK} variable reduces slowly during the burst as seen in Figure 22A. When h_{2SPK} is near 1, the model exhibits slow tonic spiking (Figure 22B). When h_{2SPK} decreases, it weakens the inward current I_{SPK}, thereby reducing the voltage peak, v_{max}, of the spike. Since v_{max} is lower, the outward current turns on with less strength. The results in weaker hyperpolarization and more spikes transitioning to a burst. When h_{2SPK} is reduced further, we see that the spike height reduces more, leading to the weaker hyperpolarization between spikes and an increase in the number spikes in the burst. Hence, when dynamic h_{2SPK} reduces during the burst, it starts off as slow tonic spiking and then progresses to a full burst with decreased hyperpolarization between spikes producing the ramping bursting pattern. The bifurcation analysis of the model, which is identical to the AHP model is shown in the Appendix (Figure 51).

Table 6: Default parameter values for SPK model (22),(23):

g_{Na}	150.0 nS	g_{NaP}	3.0 nS	g_K	220.0 nS
g_{syn}	0.285 nS	e_{Na}	55.188 mV	e_K	−69.829 mV
e_{syn}	−10.0 mV	c	36.0 pF	$v_{h_{Na}}$	67.5 mV
$k_{h_{Na}}$	67.5 mV	$p_{h_{Na}}$	−12.8 mV	$v_{h_{NaP}}$	60.0 mV
$k_{h_{NaP}}$	60.0 mV	$p_{h_{NaP}}$	9.0 mV	$v_{h_{SPK}}$	27.5 mV
$v_{h_{2SPK}}$	27.5 mV	$s_{h_{2SPK}}$	−1.0 mV	$k_{h_{2SPK}}$	60.0 mV
$v_{m_{SPK}}$	27.5 mV	$s_{m_{SPK}}$	−1.0 mV	$v_{m_{Na}}$	43.8 mV
$k_{m_{Na}}$	43.8 mV	$p_{m_{Na}}$	14.0 mV	$v_{m_{NaP}}$	47.1 mV
$k_{m_{NaP}}$	47.1 mV	$p_{m_{NaP}}$	6.2 mV	$t_{h_{Na}}$	8.46 mS
$t_{m_{Na}}$	0.25 mS	$t_{m_{NaP}}$	1.0 mS	$t_{h_{SPK}}$	5.0 mS
$t_{m_{SPK}}$	0.5 mS	g_L	4.0 nS	e_L	−62.587 mV
$s_{h_{Na}}$	−11.8 mV	$s_{h_{NaP}}$	−9.0 mV	$s_{h_{SPK}}$	−1.0 mV
$p_{h_{2SPK}}$	8.5119 mV	$s_{m_{Na}}$	6.0 mV	$s_{m_{NaP}}$	3.1 mV
$t_{h_{NaP}}$	5000.0 mS	$t_{h_{2SPK}}$	1000.0 mS		

3.4 Dynamic spike height model (DSPK)

The biologically relevant model associated with the AHP model is already presented in [3]. The potassium ion concentration dynamics help control the strength of hyperpolarization between spikes in the burst in [3]. In this section, we present an relevant model associated with the SPK model concept. We modify the model presented in [4] by adding an additional inactivation gate associated with the sodium current I_{Na} [56, 57, 68]. The differential equations for the model dynamics are given by:

$$\begin{cases} cv' &= -(I_{Na}(v, h_{Na}, h_{2Na}, m_{Na}) + I_K(v, n) + I_{NaP}(v, h_{NaP}, m_{NaP}) \\ & \quad + I_L(v) + I_{syn}(v)), \\ h'_{2Na} &= (h_{2Na\infty}(v) - h_{2Na})/\tau_{h_{2Na}}(v), \end{cases} \tag{24}$$

Notice that we added an additional inactivation gate h_{2Na} to the sodium current I_{Na} in (24). The equations for the other variables, $h_{Na}, m_{Na}, h_{NaP}, m_{NaP}$ and n are same as in.

The expressions for the I_{Na} current and steady state activation functions for h_{2Na} in (24) are given by:

$$\begin{aligned} I_{Na}(v, h_{Na}, h_{2Na}, m_{Na}) &= g_{Na}\, {m_{Na}}^3\, h_{Na}\, h_{2Na}\, (v - e_{Na}), \\ h_{2Na\infty}(v) &= (1 + e^{-(v_{h_{2Na}} + v)/s_{h_{2Na}}})^{-1}, \\ \tau_{h_{2Na}}(v) &= t_{h_{2Na}}\, \cosh((k_{h_{2Na}} + v)/p_{h_{2Na}})^{-1}, \end{aligned} \tag{25}$$

All the other currents and activation functions are same as in .

The default parameter values are given in Table 7 for which the model exhibits a ramping bursting pattern shown in Figure 23. The parameter values in Table 7 were obtained from an optimization routine in MATLAB and we can vary them away from these values without significantly affecting the ramping pattern. Notice that the burst starts as relatively slow oscillations and then continues to a full burst.

Table 7: Default parameter values for DSPK model (24)-(25) :

g_{Na}	108.271 nS	g_{NaP}	3.7666 nS	g_K	250.148 nS
g_{syn}	0.3921 nS	e_{Na}	55.0 mV	e_K	−73.0 mV
e_{syn}	−10.0 mV	c	36.0 pF	$v_{h_{Na}}$	68.0 mV
$k_{h_{Na}}$	67.5 mV	$p_{h_{Na}}$	−12.8 mV	$v_{h_{NaP}}$	60.8242 mV
$k_{h_{NaP}}$	63.5594 mV	$p_{h_{NaP}}$	9.41933 mV	$v_{h_{2Na}}$	44.3497 mV
$k_{h_{2Na}}$	−49.2889 mV	$p_{h_{2Na}}$	4.5524 mV	$v_{m_{Na}}$	43.8 mV
$k_{m_{Na}}$	43.8 mV	$p_{m_{Na}}$	14.0 mV	$v_{m_{NaP}}$	47.1 mV
$k_{m_{NaP}}$	47.1 mV	$p_{m_{NaP}}$	6.2 mV	$t_{h_{Na}}$	8.46 mS
$t_{m_{Na}}$	0.25 mS	$t_{m_{NaP}}$	1.0 mS	$t_{h_{2Na}}$	1010.0 mS
e_L	−62.5 mV	$s_{h_{Na}}$	−11.9 mV	$s_{h_{NaP}}$	−9.3338 mV
$s_{h_{2Na}}$	−1.92387 mV	$s_{m_{Na}}$	6.0 mV	$s_{m_{NaP}}$	3.1 mV
$t_{h_{NaP}}$	5250.0 mS	g_L	4.0 nS		

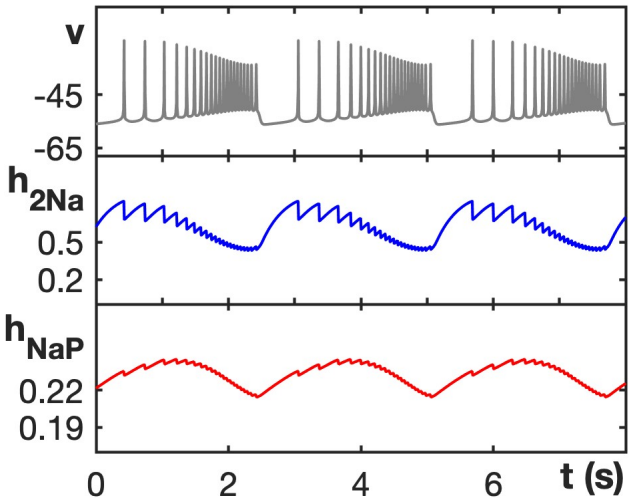

Figure 23: Ramping burst pattern exhibited by the DSPK model (24)-(25) for default parameter values given in Table 7

3.5 Robustness of DSPK model

To study the robustness of the ramping burst pattern to parameter changes, we examine the activity patterns exhibited by the model across a range of g_L and g_NaP values, as shown in Figure 24A. Figure 24B shows the bifurcation diagram of the full model (24)-(25) with respect to g_L. As g_L increases, we see that the model undergoes a Hopf bifurcation, resulting in stable oscillations which terminates at a SNIC bifurcation. For a fixed h_{NaP} value, the activity pattern transitions from depolarized stable equilibrium point to spike/burst and eventually settles to a stable equilibrium as g_L increases. In Figure 24A, the spiking region is shown in black, while the bursting region is shown in blue. The red shaded region corresponds to ramping bursts. We see that the ramping effect of bursts is observed only within small region of parameter space.

A comparison of the inter-spike intervals within the bursting patterns exhibited by the models : Model presented in [4], AHP model (19)-(21), SPK model (22), (23) and DSPK model (24), (25) is shown in Figure 25. Notice that in the original unmodified model shown in (A), ISI is increasing, and spike frequency is decreasing, whereas the opposite is true for

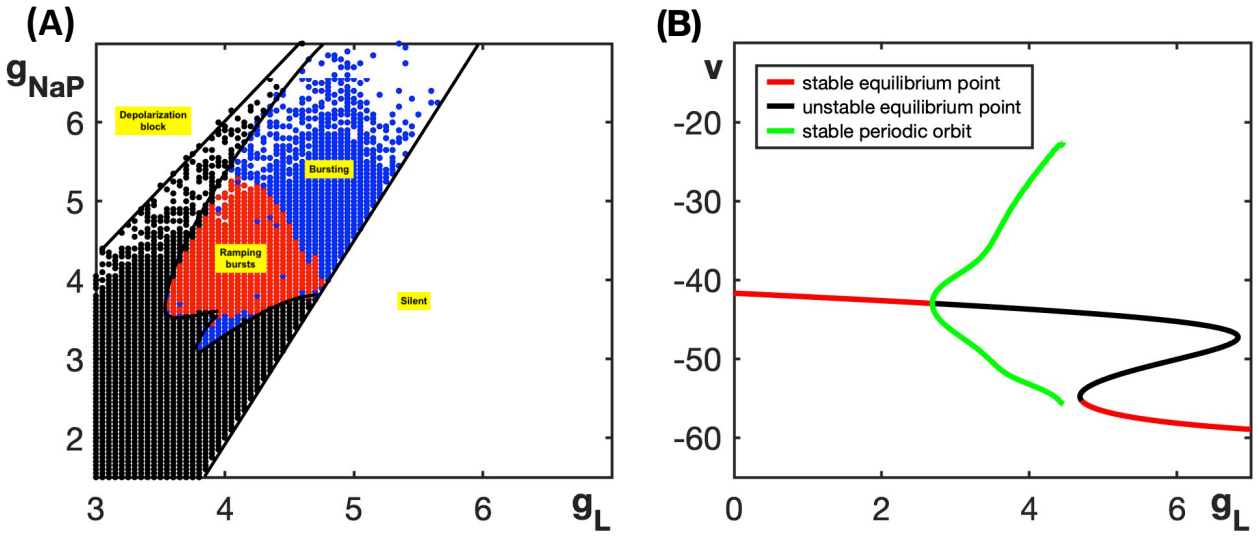

Figure 24: (A) The different activity patterns exhibited by model (24), (25) for different g_{NaP} and g_L values. (B) Bifurcation diagram of the full model (24), (25) with respect to g_L.

the modified models in shown (B)-(D).

To analyze the model further, we look at the different activity patterns exhibited by the model (24)-(25) for $g_{NaP} = 3.7666$ and varying g_L. In Figure 24A, its shown that the activity pattern changes from spiking for low g_L values to bursting for g_L around 4, and then turns to spiking again for higher g_L values. In fact, numerical simulations show that before transitioning to spiking, the model also exhibits amplitude modulated fast spiking for a very small range of g_L values near 3.54. Therefore, in the rest of this section we analyze in detail the four patterns exhibited by the model for $g_{NaP} = 3.7666$.

When g_L is increased, the membrane potential is more hyperpolarized and requires higher range of values of m_{Na} and m_{NaP} to start oscillations. This, in turn, causes the v_{max} of the spike/burst to be higher. Similarly, when g_L increases, the model does not require the inactivation variables h_{Na}, h_{2Na} and h_{NaP} to reduce much to again hyperpolarize the voltage. Hence, when g_L increases, the h_{Nap}, h_{2Na}, and h_{Na} also have higher range of values. Since v_{max} is higher, I_K turns on more strongly causing the voltage to hyperpolarize more. This, in turn, causes v_{min} to the lowered. Hence, to conclude, when g_L is increased, the amplitude of oscillations increases. Since the rate of change of h_{2Na} depends on v in (24), the increase in range of v results in increase in the timescale of h_{2Na} (See Appendix for non-dimensionalization process).

Non-dimensionalization of the DSPK model for different values of g_L is shown in the Appendix. h_{NaP} has a slow timescale for all values of g_L. For $g_L = 3.5$, its clear that h_{2Na} can also be considered as slow. However, when g_L is increase to 4 and then to 4.6, the timescale of h_{2Na} is less clear. We analyze h_{2Na} as having an intermediate timescale for $g_L = 4$ and having fast timescale for $g_L = 4.6$. This is after considering timescale difference between h_{2Na} and h_{NaP} as well as h_{2Na} and the other fast variables in the model (primarily, n which is the slowest variable in the fast subsystem). Supplementary Figure 52 shows the absolute values of the derivatives of h_{NaP}, h_{2Na} and n in DSPK model (24), (25) along the activity pattern for different values of g_L. We indeed see that the rate of change of h_{2Na} is closer to h_{NaP} for $g_L = 3.5$ and closer to n for $g_L = 4.6$.

We now analyze the activity pattern for different g_L values below.

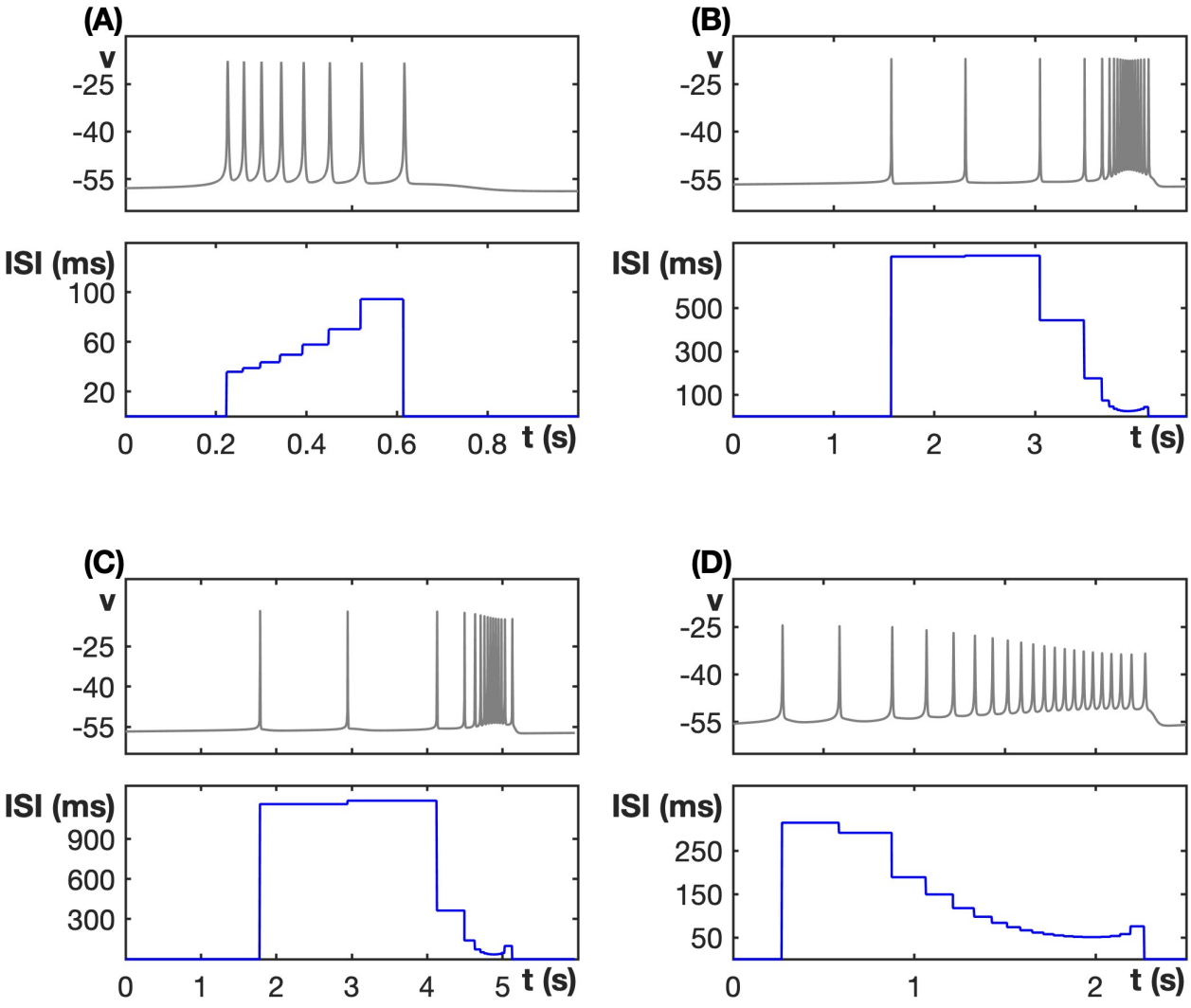

Figure 25: ISI of different models (A) Model presented in [4] (B) AHP model (19)-(21) (C) SPK model (22), (23) (D) DSPK model (24), (25).

3.5.1 $g_L = 3.5$

In this case, when g_L=3.5, the model generates fast spiking. See Figure 26A. From non-dimensionalization process, we see that in this case, both h_{NaP} and h_{2Na} can be considered to be slow variables. Therefore, the model for g_L=3.5 can be studied as a 5-fast and 2-slow system.

During the spike, we notice that $h_{NaP} \approx 0.163$ throughout the spike. Since h_{2Na} is also much slower than the other fast variables in the model, we can look at the bifurcation diagram of the fast subsystem with respect to h_{2Na} with h_{NaP} fixed at 0.163. This is shown in Figure 26B with the spiking trajectory at $g_L = 3.5$ superimposed in grey. Notice that the spiking trajectory corresponds to a stable periodic orbit in the fast subsystem. This implies that there is zero net drift of h_{2Na} at $h_{2Na} \approx 0.45$ with $h_{NaP} \approx 0.163$. It looks like spiking trajectory corresponds to a fixed point in the slow system.

To verify our observations in Figure 26B and to further analyze the slow subsystem, we plot the two parameter bifurcation diagram of the fast subsystem with repesct to h_{2Na} and h_{NaP} (Figure 26C). We also calculate the slow averaged nullclines for the slow subsystem averaged over the fast subsystem oscillations. When averaging over the fast spikes, the slow averaged system of equations are given by :

$$\begin{aligned} h'_{NaP} &= \frac{1}{T(h_{NaP},h_{2Na})} \int_0^{T(h_{NaP},h_{2Na})} (h_{NaP\infty}(v(h_{NaP},h_{2Na})) - h_{NaP})/\tau_{h_{NaP}}(v(h_{NaP},h_{2Na})) \\ h'_{2Na} &= \frac{1}{T(h_{NaP},h_{2Na})} \int_0^{T(h_{NaP},h_{2Na})} (h_{2Na\infty}(v(h_{NaP},h_{2Na})) - h_{NaP})/\tau_{h_{2Na}}(v(h_{NaP},h_{2Na})) \end{aligned} \tag{26}$$

where $v(h_{NaP}, h_{2Na})$ is the stable periodic orbit of the fast-subsystem for fixed h_{NaP} and h_{2Na} having period $T(h_{NaP}, h_{2Na})$.

The equations (26) are valid over the range of h_{2Na} - h_{NaP} values where there are stable oscillations in the fast subsystem. In fact, in Figure 26C, this correspond to the parameter range to the right side of the HC curve (shown in green) and to the left side of AH curve (shown in blue). We see in Figure 26C that the slow averaged nullclines intersect at a fixed point very near $h_{2Na} \approx 0.45$ with $h_{NaP} \approx 0.163$. Averaging theory tells us that this fixed point corresponds to a stable periodic orbit in the full system. However, there is an ϵ error

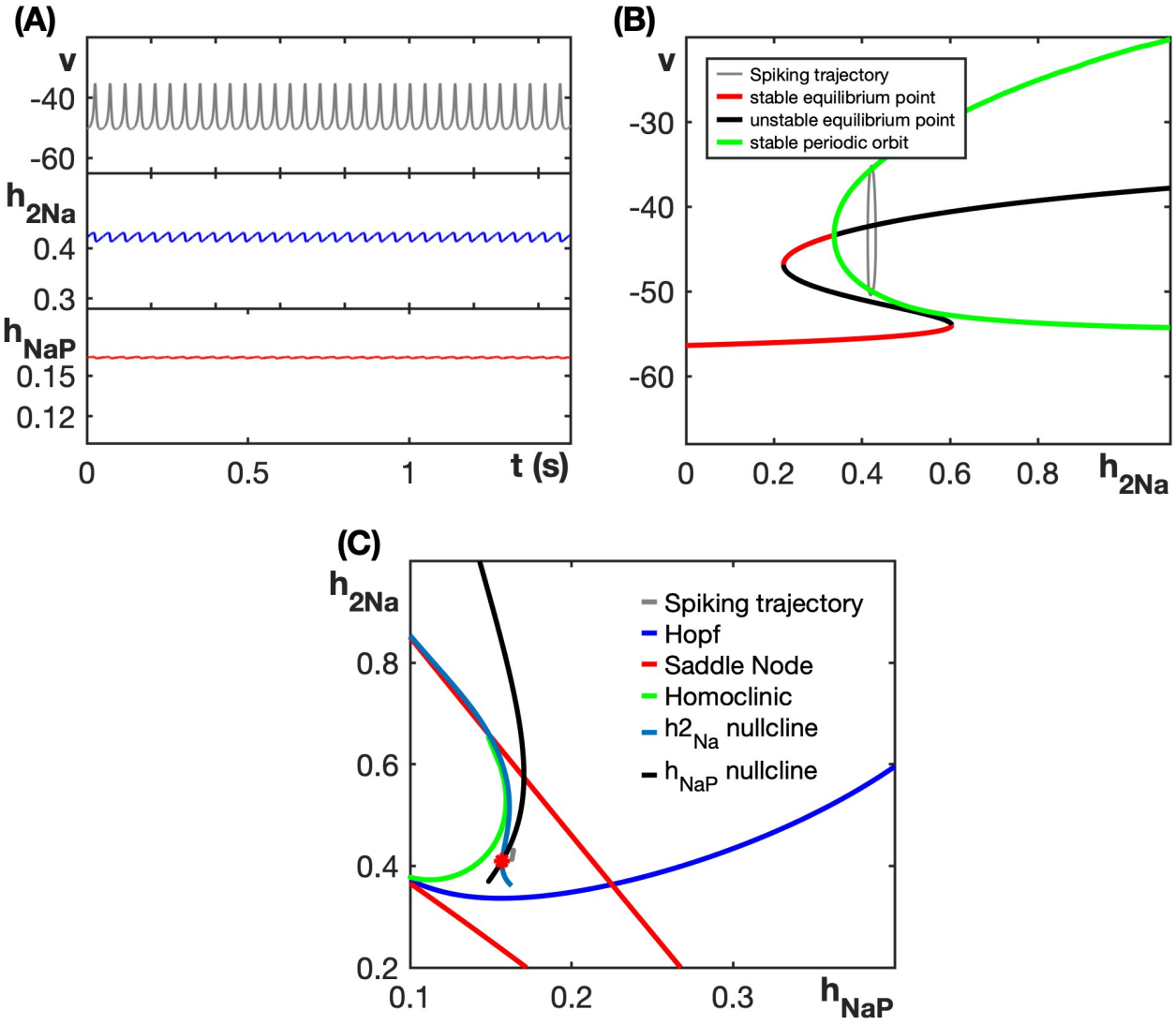

Figure 26: (A) Spiking pattern exhibited by the DSPK model (24), (25) for $g_L = 3.5$. (B) Bifurcation diagram of the fast subsystem with respect to h_{2Na} for $h_{NaP} = 0.163$ (C) The two-parameter bifurcation diagram of the fast subsystem with respect to h_{2Na} and h_{NaP}. The slow averaged nullclines of h_{2Na} and h_{NaP} are shown in blue and black respectively. In both (B) and (C), the spiking trajectory is overlaid in grey. Notice that the spiking trajectory is very close to the fixed point of the slow averaged system shown in red asterisks.

in the fixed point and averaged nullcline calculation since they are calculated assuming h_{NaP} and h_{2Na} to be fixed. Hence, combining figures we now have the full analysis of the fast spiking trajectory for g_L=3.5.

3.5.2 $g_L = 3.54$

When g_L is increased to 3.54, the model exhibits amplitude modulated spiking (AM) shown in Figure 27A. The timescale of h_{2Na} does not vary much from the previous case since the increase in g_L is very small. Hence, in this case, the model can again be analyzed as a 5-fast and 2-slow model.

Fixing h_{NaP}= 0.168, we first look at the 1-parameter bifurcation diagram with respect to h_{2Na}(See Figure 27B). Note that, compared to the previous case, we no longer have a stable oscillation in the full system. The trajectory, depicted in grey, initially drifts to the right through the stable periodic orbits of the fast subsystem and subsequently reverses its direction, drifting to the left. From this its clear that there is a drift in h_{NaP} as well since the trajectory reverses its direction. To analyze this further we look at the two parameter bifurcation diagram (See Figure 27C) with respect h_{2Na} and h_{NaP}.

Since we are assuming both h_{2Na} and h_{NaP} to be slow, the slow averaged equations given in (26) are valid for this case as well. The two parameter bifurcation diagram (See Figure 27C) superimposed with the slow nullcline for h_{2Na} and h_{NaP}, shows that even though the slow averaged nullclines intersects at a fixed point, it's unstable with a stable periodic orbit around it. Hence, when increasing g_L from 3.5 for 3.54, the stable fixed point in the slow averaged system destabilizes and we have a stable periodic orbit instead. In fact, numerical simulations show that at a g_L value close to 3.54, the full system undergoes a torus bifurcation.

3.5.3 $g_L = 4$

The bursting pattern exhibited by the model (24), (25) for $g_L = 4$ is shown in Figure 23. Non-dimensionalization shows that for $g_L = 4$, the timescale constant of h_{2Na} is higher than that of the previous cases (See Appendix and Supplementary Figure 52). In this case,

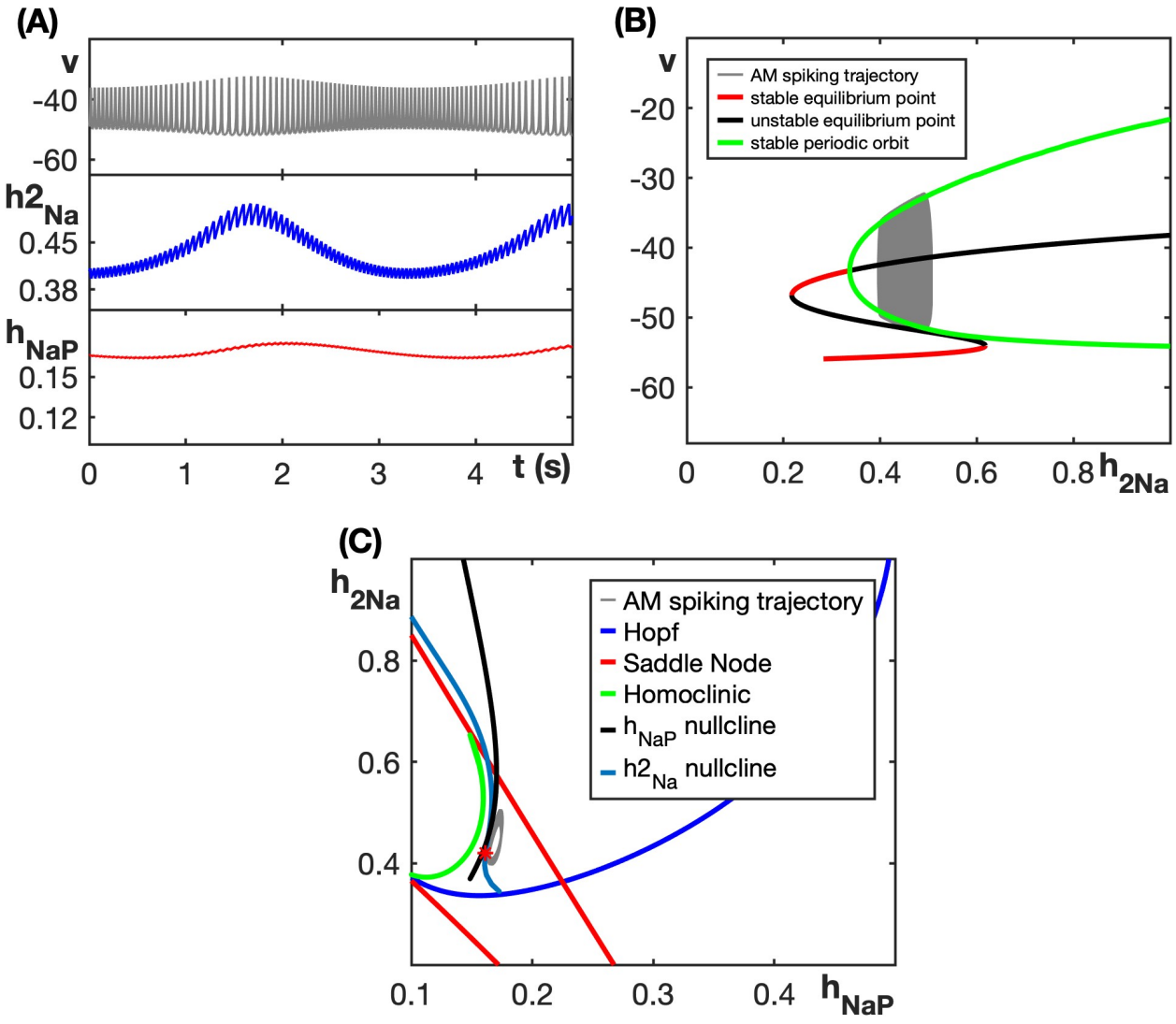

Figure 27: (A) Amplitude modulated (AM) spiking pattern exhibited by the DSPK model (24), (25) for $g_L = 3.54$. (B) Bifurcation diagram of the fast subsystem with respect to h_{2Na} for $h_{NaP} = 0.168$ (C) The two-parameter bifurcation diagram of the fast subsystem with respect to h_{2Na} and h_{NaP}. The slow averaged nullclines of h_{2Na} and h_{NaP} are shown in blue and black respectively. The fixed point in the slow averaged system is shown in red asterisks. In both (B) and (C), the AM spiking trajectory is overlaid in grey.

we analyze h_{2Na} as having an intermediate timescale with h_{Nap} being slow and the other variables being fast.

Let us analyze the case with $g_L = 4$ in parts. We divide the bursting region in four parts as shown in Figure 28A and analyze each region separately. The bifurcation diagrams of the fast subsystem with respect to h_{2Na} for different h_{NaP} corresponding to the different regions are shown in 28B,C,D.

Since h_{2Na} and h_{Nap} are still slower than the other variables in the system, we plot the two-parameter bifurcation diagram (See Figure 29). However, keep in mind that all curves have epsilon error to them since we keep h_{Nap} and h_{2Na} fixed while calculating it. Similarly, since h_{2Na} has an intermediate timescale between the slow h_{Nap} and other fast variables in the model, we can calculate the slow averaged nullcline for h_{2Na} with h_{Nap} fixed. This is shown in blue in Figure 29. This nullcline is valid (up to an epsilon error) for the all the analysis below.

Since h_{2Na} is assumed to be faster than h_{NaP}, we cannot compute the averaged slow equation for h_{Nap} with h_{2Na} fixed, as we have done in previous cases. We can however, calculate it, if h_{2Na} values are close to its slow nullcline and average flow in h_{2Na} is almost zero. The other option is for us to average over the fast-intermediate system. This is again only possible for those h_{Nap} values where there are stable oscillations in the fast-intermediate system.

Let us now analyze each of the different regions:

Region I : The burst starts at the cyan diamond marker. The bifurcation diagram of the fast subsystem with respect to h_{2Na} for $h_{NaP} = 0.22$ is shown in Figure 28B. Note that within this region, the fast-intermediate subsystem exhibits stable oscillations. Hence, we can calculate the average slow drift of h_{Nap} using the equation :

$$h'_{NaP} = \frac{1}{T(h_{NaP})} \int_0^{T(h_{NaP})} (h_{NaP\infty}(v(h_{NaP})) - h_{NaP})/\tau_{h_{NaP}}(v(h_{NaP})) \tag{27}$$

where $v(h_{NaP})$ is the stable periodic cycle of the fast-intermediate system for fixed h_{NaP} with period $T(h_{NaP})$.

For each fixed h_{NaP} value in this region, we can successively fix h_{2Na} at various values, average over the fast subsystem oscillation for each (h_{NaP}, h_{2Na}) pair, and determine the

location of the h_{2Na} averaged nullcline. We find that the burst is to the right of the h_{2Na} slow averaged nullcline, and hence h_{2Na} shows a net decrease on average during each oscillation that occurs within this region.

Next, we average over the fast-intermediate oscillation for each fixed h_{NaP}, using equation (27). The right hand side of this equation is positive, and hence, h_{NaP} increases slowly in this region. Therefore, in region I, we observe slow tonic oscillations with h_{2Na} exhibiting an intermediate timescale and decreasing trend, while h_{Nap} has a slow, increasing drift. This continues until we hit the red diamond.

Region II : In this region, with increase in h_{NaP}, we lose the homoclinic curve, and consequently lose the stable oscillations in the fast-intermediate subsystem. Instead, in this case, we have a stable oscillations in the fast subsystem. Since h_{2Na} is faster than h_{NaP}, h_{2Na} is gradually attracted to its nullcline (on intermediate timescale) while the fast variables engage in fast periodic cycles and h_{NaP} remains roughly constant. Therefore, in this case, we get fast oscillations with h_{2Na} having decreasing trend and h_{NaP} almost constant. This continues till the black diamond marker. The bifurcation diagram with respect to h_{2Na} for $h_{NaP} \approx 0.245$ is shown in 28C.

Region III: After the black diamond, h_{2Na} is close to its nullcline (average drift is approximately zero in every cycle) making its timescale comparable to that of h_{NaP}. Hence, in this region we can calculate the average slow drift of h_{NaP} using the equation

$$h'_{NaP} = \frac{1}{T(h_{NaP}, h_{2Na})} \int_0^{T(h_{NaP}, h_{2Na})} (h_{NaP\infty}(v(h_{NaP}, h_{2Na})) - h_{NaP})/\tau_{h_{NaP}}(v(h_{NaP}, h_{2Na})) \tag{28}$$

where $v(h_{NaP}, h_{2Na})$ is the stable periodic orbit of the fast-subsystem for fixed h_{NaP} and h_{2Na} having period $T(h_{NaP}, h_{2Na})$. The equation (28) is valid since the average drift of h_{2Na} in this region is approximately zero, that is,

$$h'_{2Na} = \frac{1}{T(h_{NaP}, h_{2Na})} \int_0^{T(h_{NaP}, h_{2Na})} (h_{2Na\infty}(v(h_{NaP}, h_{2Na})) - h_{NaP})/\tau_{h_{2Na}}(v(h_{NaP}, h_{2Na})) \approx 0$$

.

We see that the right hand side of (28) is negative. Therefore, in this case, h_{NaP} and h_{2Na} have comparable timescales with both h_{NaP} and h_{2Na} decreasing. Continuing forward,

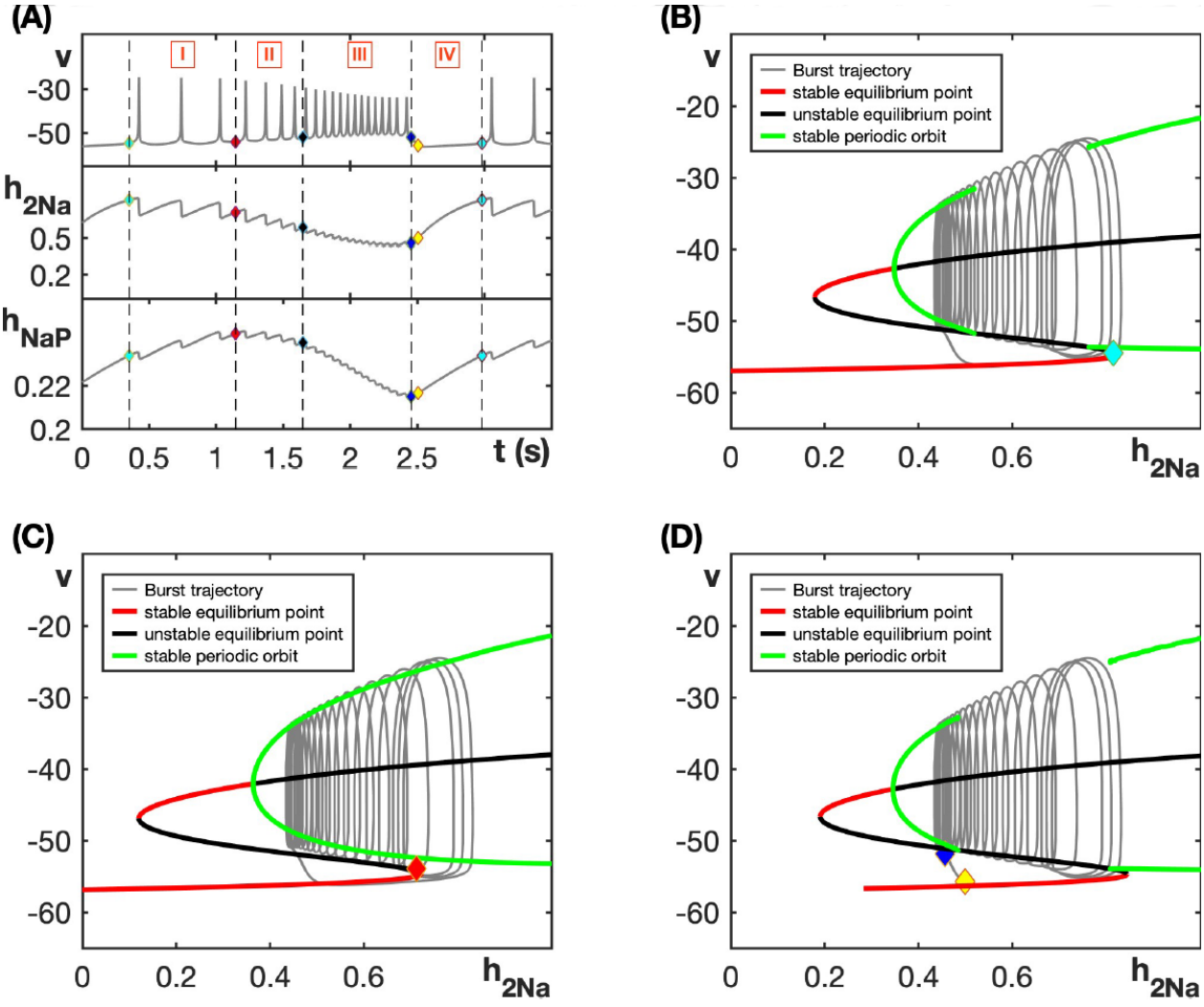

Figure 28: (A) Ramping bursting pattern exhibited by the DSPK model (24), (25) for $g_L = 4$. To analyze the burst further, we divide it into different regions as shown (B) Bifurcation diagram of the fast subsystem with respect to h_{2Na} for $h_{NaP} = 0.22$. (C) Bifurcation diagram of the fast subsystem with respect to h_{2Na} for $h_{NaP} = 0.245$. (D) Bifurcation diagram of the fast subsystem with respect to h_{2Na} for $h_{NaP} = 0.215$. In all (B)-(D), the bursting trajectory is overlaid in grey.

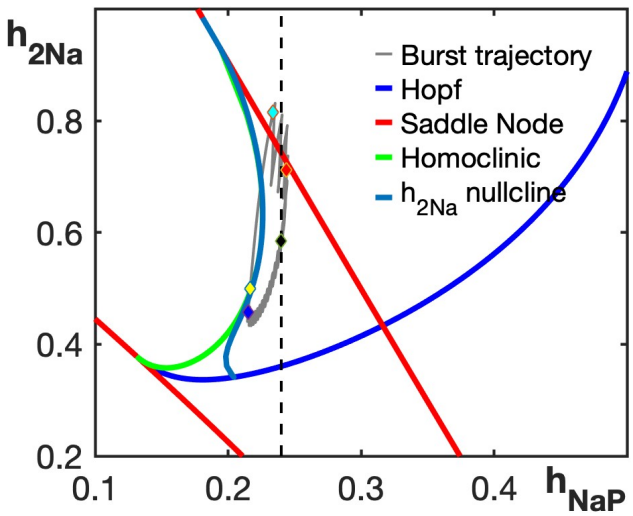

Figure 29: The two-parameter bifurcation diagram of the fast subsystem of DSPK model (24), (25) with respect to h_{2Na} and h_{NaP} for $g_L = 4$. The slow averaged nullcline of h_{2Na} averaged over the oscillations in the fast subsystem is shown in blue. The slow averaged nullcline of h_{NaP} averaged over the stable oscillation in fast-intermediate subsystem is shown as dashed black line. The bursting trajectory is overlaid in grey.

h_{2Na} hits its nullcline at blue diamond, and starts increasing, causing it to intersect the homoclinic curve, lose the stable oscillations and fall to the lower branch of the v nullcline.

Region IV: In this region, the burst traverses the lower branch of the v-nullcline till it hits the SN at cyan diamond marker and jumps up to start slow oscillations in Region I.

We have now analyzed the full burst. Like previously mentioned, slow average nullcline of h_{2Na} (shown in light blue in 29) is valid through the burst. From cyan to black asterisks (region I and II) h_{2Na} is considered to have intermediate timescale. Here, we only know the drift in h_{NaP} in region I where there are stable oscillation in fast intermediate subsystem. From black to cyan asterisks (region III and IV), h_{2Na} is close to nullcline and can be considered as slow. Hence in this region, the slow averaged nullcline of h_{NaP} (shown in black in 29) is valid.

For $g_L = 3.54$ (AM spiking), we had a small amplitude periodic cycle in the $h_{NaP} - h_{2Na}$ space that does not intersect the homoclinic curve (See Figure 26C). In case of $g_L = 4$, the amplitude of oscillation in the $h_{NaP} - h_{2Na}$ space (intermediate-slow subsystem) has grown large enough that it intersecting the homoclinic curve (See Figure 29). This causes the oscillations in the top stable periodic branch of the fast subsystem to fall to the lower stable branch, leading to a transition in the activity pattern from spiking to bursting.

3.5.4 $g_L = 4.6$

For $g_L = 4.6$, the model exhibits spiking pattern shown in Figure 30A. Non-dimensionalization (See Appendix and Supplementary Figure 52) shows that for $g_L = 4.6$, the timescale constant of h_{2Na} is comparable to the timescale of the fast variables in the model, particularly for high v values. In this case, we analyze the model as having 6 fast variables and 1 slow variable (h_{NaP}). Figure 30B shows the bifurcation diagram of the fast subsystem (all variables including h_{2Na}) with respect to the slow variable h_{NaP}. Notice that the spiking trajectory corresponds to a stable periodic orbit in the fast subsystem for $h_{NaP} \approx 0.33$ (See Figure 30C).

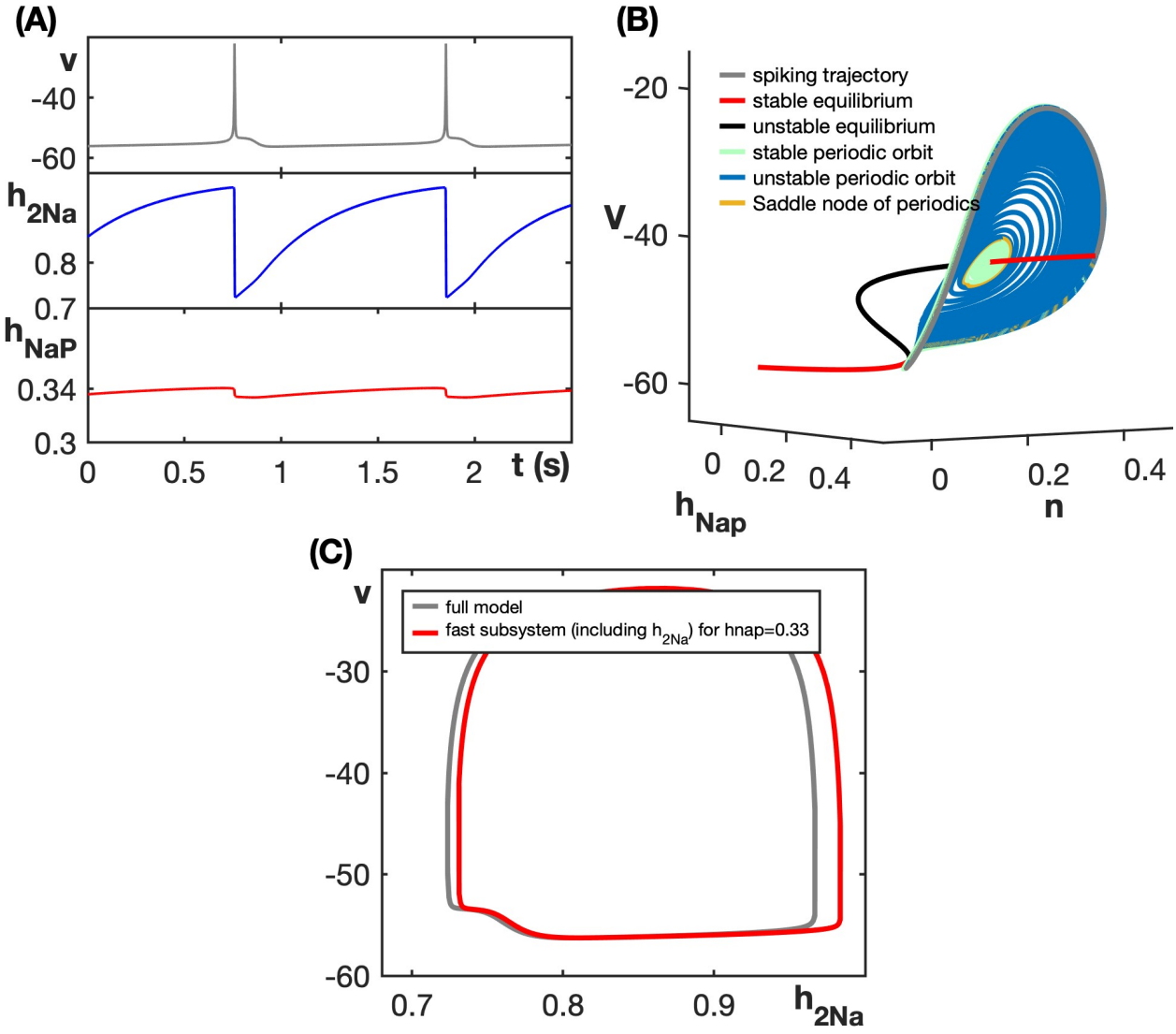

Figure 30: (A) Spiking pattern exhibited by the DSPK model (24), (25) for $g_L = 4.6$. (B) Bifurcation diagram of the fast subsystem (now also including h_{2Na}) with respect to h_{NaP}. The spiking trajectory is overlaid in grey. Notice that the spiking trajectory is a stable periodic orbit in the fast subsystem for for $h_{2Na} = 0.33$ (C) The spiking trajectory exhibited by the model for $g_L = 4.6$ shown in grey whereas the periodic orbit in the fast subsystem with $h_{2Na} = 0.33$ is shown in red.

3.6 Discussion

In this work, we present three models that exhibits ramping bursting pattern. The two phenomenological models explain how adding slow dynamics to the sodium and potassium currents, which are responsible for the upstroke and downstroke of the spikes in the burst, respectively, helps shape the bursting pattern. We then apply this to a more realistic model by adding an additional slow negative feedback to the inward sodium current and see that we get the ramping effect. This is based on experimental evidence that suggest that sodium current may have different inactivation components that evolves at different timescales [68, 56].

Non dimensionalization classifies h_{NaP} as a slow variable and v, h_{Na}, m_{Na}, m_{NaP}, and n as fast variables. The timescale of h_{2Na}, while always faster than h_{NaP}, is more comparable to h_{NaP} when g_L is low. On the other hand, when g_L is higher, the timescale of h_{2Na} becomes more comparable to the timescale of the other fast variables. Hence, we analyzed h_{2Na} as having slow timescale in the first two cases with $g_L = 3.5$ and $g_L = 3.54$, an intermediate timescale when g_L=4, and a fast timescale when $g_L = 4.6$. Numerical simulations in Figure 31 shows that when g_L increases from 3.5 to 3.54, the critical point becomes unstable and there are stable periodic orbits in the h_{2Na}-h_{NaP} space which grow in size as g_L increases. It could be further analyzed to check if this is due to a Hopf bifurcation in the slow subsystem. When the periodic orbit in the slow subsystem grows and starts to intersect the homoclinic curve, like shown in Figure 29, the oscillations which where stabilized in the upper branch of v-nullcline loses stability and falls to the stable lower branch. This marks the transition from AM spiking to bursting. The transition from bursting to the fast spiking when g_L=4.6 is not well defined. We have seen that when g_L=4.6, the h_{2Na} variable has timescale comparable to the other fast variables in the system. We leave the more mathematical analysis of each of the transitions as future direction for further exploration.

Adding potassium concentration dynamics to a bursting model results in ramping bursting pattern as seen in [3]. However, in both the model in [3] as well as the DSPK model (24), (25), the parameter range where the model displays ramping effect is very narrow. A future direction to explore would be to add sodium concentration dynamics to the model. If

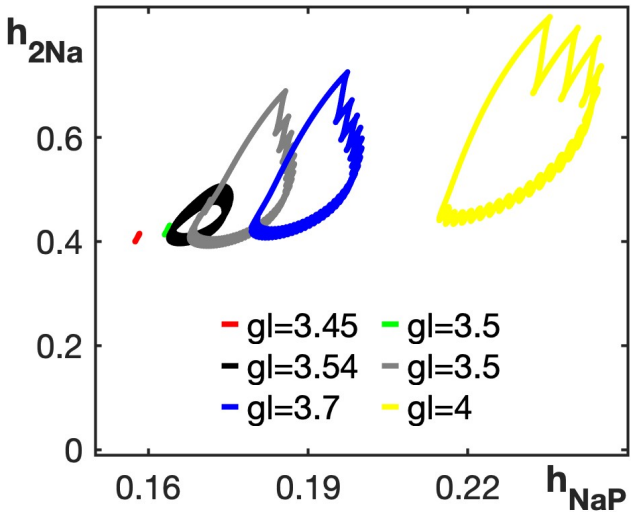

Figure 31: The activity patterns in the $h_{2Na} - h_{NaP}$ space for different values of g_L.

the E_{Na} slowly changes during the burst, it is possible that we may see ramping dynamics. Modeling resurgent Na^+ current is yet another direction to explore in order to get ramping dynamics since it can enhance inward current flow and lead to faster spiking during the burst [52].

4.0 The role of Kölliker-Fuse nucleus in breathing variability [1]

4.1 Introduction

Breathing is an automatic process produced and shaped by the respiratory central pattern generator (rCPG), which comprises several neural structures in the brainstem [79]. Extensive work has characterized the synaptic and ionic mechanisms that generate and regulate the activity of ventromedullary respiratory neurons and how these mechanisms affect breathing rhythm and pattern. This study focuses on a major counterpart to the medullary rCPG: the pontine Kölliker-Fuse nucleus (KF). The KF is part of the parabrachial complex in the dorsolateral pons and is formed by a collection of neurons surrounding the superior cerebellar peduncle [90]. Although it was first described as the inspiratory off-switch center, compelling evidence indicates that the KF activity critically contributes to maintaining the eupneic 3-phase respiratory pattern (inspiration, post-inspiration, and stage 2 of expiration). Moreover, KF neurons are required for the adjusting breathing characteristics across a range of conditions.

Much of this evidence derives from studies featuring significant perturbations in KF activity. For example, lesions of the KF substantially alter the respiratory pattern, introducing augmented variability in frequency and amplitude, or even eliminating the post-inspiratory phase and thus disrupting eupneic breathing [64, 35, 25, 10, 12, 77, 45]. Chemical excitation of KF neurons enhances constrictor activity in upper airway muscles and prolongs the duration of the post-inspiratory phase of the respiratory cycle [25]. In contrast, disruption of GABAergic transmission in the KF induces periodic apneas, respiratory irregularities, and the loss of abdominal expiratory contractions (or active expiration) during exposure to high levels of carbon dioxide [2, 20, 9]. KF neurons are also targets for neuromodulators that modify neuronal excitability and change the breathing pattern and rhythm. In this regard, activating 5-HT_{1A} (serotonin) receptors in the KF reduces spontaneous apneas, while antag-

[1] This chapter is based on work submitted to The Journal of Physiology : John, S., Barnett, W., Abdala, A., Zoccal, D., Rubin, J., & Molkov, Y. (2023). The role of Kölliker-Fuse nucleus in breathing variability. bioRxiv : the preprint server for biology, 2023.06.15.545086. https://doi.org/10.1101/2023.06.15.545086

onizing these receptors can destabilize breathing frequency [20]. Some KF neurons express μ-opioid receptors that, when activated, can cause breathing irregularities and bring about life-threatening apneas, a mechanism associated with opioid-induced respiratory depression [5]. In addition to the control of eupneic breathing, the KF also contributes to the respiratory adjustments related to behaviors such as vocalization, swallowing, and coughing [24, 44, 11], acting as a convergent and integrative synaptic station that relays inputs from suprapontine regions to the rCPG [40]. Despite the evidence showing the critical role of the KF in breathing control, its cellular organization and interaction with other respiratory compartments to adjust the respiratory rhythm and pattern remain uncertain.

There is a long tradition of using mathematical modeling and computational techniques to build theoretical models of the rCPG, develop intuition about how it functions, and test hypotheses on respiratory rhythm and pattern generation [53, 59, 67]. In the past, models were developed integrating a medullary CPG circuit with a pontine component using an established reduced, activity-based mathematical framework [9, 95, 59, 32, 72, 71]. Previous models differed in their assumptions about pontine interactions and intrinsic dynamics, which need to be better characterized experimentally. These models have provided a proof of principle for the proposed central role of the KF in respiratory control and have yielded preliminary predictions about interactions of the KF with other pontine and medullary respiratory areas as well as their contribution to respiratory rhythmicity and pattern formation under a variety of conditions. The details of these predictions, however, depend on the assumptions made about intrinsic properties and activity patterns of KF neurons, synaptic interactions in the circuit, and conditions leading to aberrant KF activity and subsequent perturbations of breathing. To reproduce specific experimental observations, model networks that include the KF have required the presence of specific synaptic pathways, such as from inhibitory neurons in the Bötzinger Complex (BötC) [95] and NTS pump cells [58]. Models have also suggested that KF neurons may have certain intrinsic properties modulating their activity such as endogenous bursting [95]. This capability, however, has never been demonstrated experimentally.

Understanding the mechanisms underlying the control of KF activity is essential to identify its role in breathing pattern formation in eupnea and to determine how changes in

these mechanisms affect the expiratory motor pattern and contribute to inducing stereotyped breathing patterns such as those observed in Rett syndrome [2]. In this study we consider various KF circuit organizations paired with different baseline activity patterns and local input sources to assess which may explain a set of experimental observations not previously addressed. Specifically, each model configuration was tested against the following list of benchmarks based on the literature: (1) reduction of GABA/5-HT_{1A} inhibition in the KF leads to an aberrant respiratory pattern in which breathing is intermittently disrupted by periods of apnea [2, 20]; (2) the duration of apneic periods is relatively constant or increases as the inhibition level to KF decreases [2, 20]; (3) when KF is dysfunctional, a sufficient inchibition of the KF neurons transforms intermittent breathing into eupnea [2, 1]; (4) a further increase in inhibition of the KF neurons causes abdominal expiratory activity during the late part of the E2, or late-E, phase of the respiratory cycle, with a frequency that increases in a step-wise, or quantal, manner as inhibition is strengthened [47]. We discuss two viable model configurations, while presenting evidence against certain others, and formulate experimentally testable implications in each case.

4.2 Methods

To study the contribution of KF activity to the generation and modulation of various respiratory patterns, we developed and analyzed two families of computational models of a respiratory brain stem neuronal circuit. In the first family, which we call the *tonic model*, the KF population is homogeneous with steady, sustained or *tonic* activity under normal conditions. The other family combines two KF populations, one that shows sustained tonic activity (as in the tonic model) and another that is intrinsically silent under normal conditions. Based on the inclusion of the second population, we refer to this as the *silent model*. Schematic diagrams of the models are shown in Figure 32.

The models presented in this work are adapted from previous models for respiratory neurons and circuits [72, 71, 95]. To form these models, we incorporated the KF component into a pre-existing model presented by [71]. Similarly to that model, the models in this

work include the following respiratory populations, which together comprise what we call the *respiratory core*: pre-inspiratory (pre-I) and early-inspiratory (early-I) populations of the pre-Bötzinger Complex (pre-BötC) and post-inspiratory (post-I) and augmenting expiratory (aug-E) populations of the Bötzinger Complex (BötC). The pre-I and early-I populations are active during the inspiratory phase of respiration (I phase), whereas aug-E and post-I are active during the expiratory phase (E phase). The models also include a late-expiratory (late-E) population of the lateral parafacial region (pFL), which remains inactive during resting breathing [16].

All of the synaptic connections between these respiratory populations in the models shown in Figure 32 are either directly shown in, or inferred from, experimental observations [71]. Both models also include a KF sub-population, named KF-t, that is tonically active under normal conditions and helps to maintain eupnea. The silent model includes KF-t and another KF sub-population, named KF-s, that is silent under normal conditions. The interactions of the KF units with the respiratory core in these models occur through excitatory connections from KF-t and KF-s to the post-I population. These connections have been proposed previously [58, 45, 9, 37]. Little is known about sources of inhibition to KF neurons. For exploratory purposes, we considered both tonic inhibition to the KF originating from an unspecified outside source and recurrent inhibitory connections within the KF. We analyze the extent to which each of these inhibition types, within each model, yields outputs consistent with respiratory perturbations seen in Rett syndome (RTT), and we also study the emergence of late-E activity (active expiration). Previous work by [95] introduced a simplified representation of pulmonary stretch receptor feedback related to I phase output. As part of the analysis of the silent model done in the current chapter, we study the primary effect of this pathway by considering what happens if we introduce an additional excitatory connection from post-I to KF-s (shown as a black dashed arrow in Figure 32B). Although this connection would need to run through another inhibitory population and thus be manifested via disynaptic disinhibition in reality, for simplicity we treat it as a monosynaptic excitation in this work.

Each component in these models is described by a single two-dimensional system of Hodgkin-Huxley type equations representing the dynamics of a membrane voltage variable

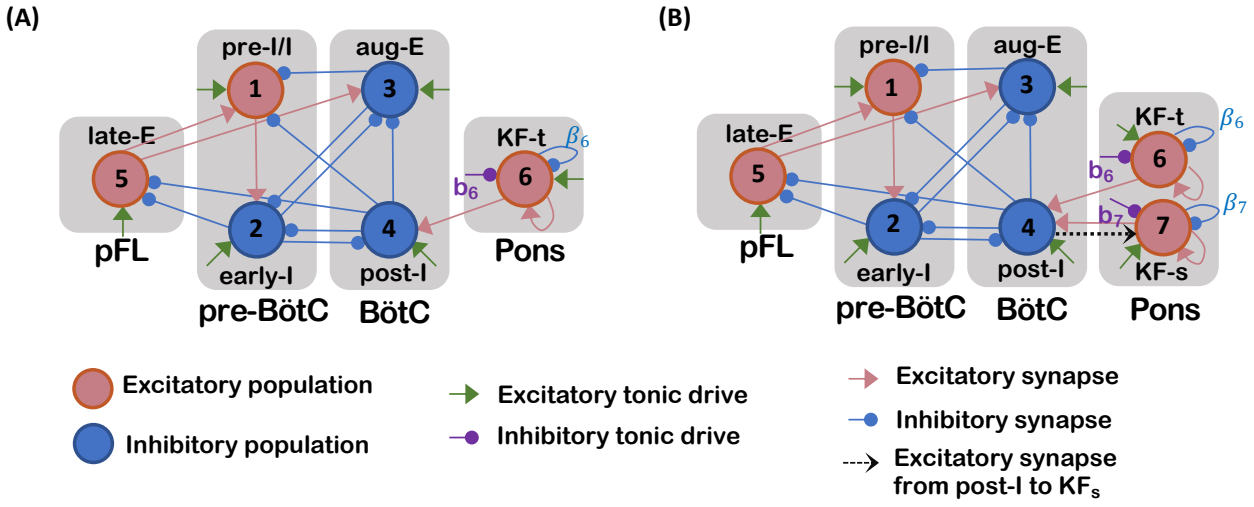

Figure 32: Schematic diagrams for the respiratory network models considered in this work. (A) Tonic model. (B) Silent model. The labels $b_6, b_7, \beta_6, \beta_7$ refer to parameters used to represent the strengths of certain connections explored in the model. Abbreviations referring to neuronal populations and sites are described in the text.

v and a secondary slow variable h or m. We consider this framework as a simplified representation of dynamics in which the activity levels of neurons within each population are synchronized, and the reduction that it provides allows us to use the tools of phase plane analysis to understand model dynamics and the effects of parameter variations. To present the equations for this system, we assign a subscript from 1 to 5 for the pre-I/I, early-I, aug-E, post-I and late-E units, respectively. The Kf-t unit is labeled as 6 and the additional Kf-s unit in the silent models as 7.

The pre-I/I ($i = 1$) and late-E ($i = 5$) units feature a persistent sodium current [18, 71] and hence are represented by the following differential equations:

$$\begin{cases} v_i' &= -(I_{NaP_i} + I_{K_i} + I_{L_i} + I_{syne_i} + I_{syni_i} + W_i)/C, \\ h_i' &= (h_{NaP_i} - h_i)/t_{NaP_i}, \end{cases} \tag{29}$$

where I_{NaP_i} is the persistent sodium current, I_{K_i} represents the delayed rectifier potassium current, I_{L_i} is the leak current, I_{syne_i} and I_{syni_i} are the excitatory and inhibitory synaptic currents, and W_i represents the noise, respectively, for each unit. All of the other units in the model network ($i \in \{2, 3, 4, 6, 7\}$) are modeled as adaptive neurons and obey the following equations:

$$\begin{cases} v_i' &= -(I_{AD_i} + I_{K_i} + I_{L_i} + I_{syne_i} + I_{syni_i} + W_i)/C, \\ m_i' &= (\gamma_i\, f_i(v_i) - m_i)/t_{AD} \quad \text{for } i \in \{2, 3, 4\}, \\ m_i' &= p_i((\alpha_i\, f_i(v_i) - m_i)/t_{AD_i}) \quad \text{for } i \in \{6, 7\}, \end{cases} \tag{30}$$

where I_{AD_i} is a second potassium current causing adaptation during spiking and t_{AD} is a constant shared for all $i \in \{2, 3, 4\}$. Importantly, the parameters t_{NaP_i} from (29) and $1/t_{AD}$ and p_i/t_{AD_i} from (30) are small relative to the timescale of the voltage variables, such that the h_i and m_i evolve relatively slowly.

The various currents in (29) and (30) are defined as follows:

$$\begin{aligned}
I_{NaP_i} &= g_{NaP_i} * m_{NaP}(v_i) * h_i * (v_i - e_{Na}), \\
I_{K_i} &= g_{K_i} * m_k(v_i)^4 * (v_i - e_{K_i}), \\
I_{AD_i} &= g_{AD} * m_i * (v_i - e_{K_i}), \\
I_{L_i} &= g_{L_i} * (v_i - e_{L_i}), \\
I_{syne_i} &= g_{syn_e} * (v_i - e_{syn_e}) * (\alpha_i * f_i(v_i) + a_i + \textstyle\sum_{j=1, j\neq i}^{7} a_{i,j} * f_j(v_j)), \\
I_{syne_e} &= g_{syn_i} * (v_i - e_{syn_i}) * (\beta_i * f_i(v_i) + b_i + \textstyle\sum_{j=1, j\neq i}^{7} b_{i,j} * f_j(v_j)).
\end{aligned} \tag{31}$$

In system (31), we introduce asterisks to indicate multiplication, to avoid confusion relating to the v_i-dependent terms in the first two equations.

The noise term, W_i, in (29) and (30) is

$$W_i = s_i \, \omega_i \sqrt{dt}, \tag{32}$$

where $\omega_i \sim \mathcal{N}(0, 1)$ (i.e., a normally distributed random variable with mean 0 and standard deviation 1) and t is the time variable. For most of the analysis in this work, we turn off the noise by setting $s_i = 0$. We indicate clearly where noise has been turned on when we describe the results. In this case, we perform simulations using the Euler method in XPPAUT [28] with timestep $dt = 0.1$.

The activation functions associated with (29),(30), and (31) are given by:

$$\begin{aligned}
m_{NaP}(v_i) &= (1 + \exp((v_i - v_{m_{NaP}})/k_{m_{NaP}}))^{-1}, \\
h_{NaP}(v_i) &= (1 + \exp((v_i - v_{h_{NaP}})/k_{h_{NaP}}))^{-1}, \\
m_K(v_i) &= (1 + \exp((v_i - v_{m_K})/k_{m_K}))^{-1}, \\
t_{NaP_i} &= t_{NaP} \, (\cosh((v_i - v_{h_{NaP}})/k_{h_{NaP}}))^{-1}, \\
t_{AD_i} &= c_i + n_i/(1 + \cosh((v_i - v_{ADi})/k_{ADi})),
\end{aligned} \tag{33}$$

with the constants c_i, n_i defined for $i \in \{6, 7\}$. The *output function* f_i for $i \in \{1, 2, 3, 4, 5\}$, which appears in both (30) and (31), takes the piecewise linear form

$$f_i(v_i) = \begin{cases} 0 & \text{if} \quad \dfrac{v_i - v_{min}}{v_{max} - v_{min}} \leq 0, \\ \dfrac{v_i - v_{min}}{v_{max} - v_{min}} & \text{if} \;\; 0 < \dfrac{v_i - v_{min}}{v_{max} - v_{min}} < 1, \\ 1 & \text{otherwise,} \end{cases} \tag{34}$$

whereas the output function f_i for $i \in \{6, 7\}$ is given by

$$f_i(v_i) = \begin{cases} 0 & \text{if} \;\; \dfrac{v_i - v_{min}}{v_{max} - v_{min}} \leq 0, \\ \dfrac{v_i - v_{min}}{-v_{min}} & \text{otherwise,} \end{cases} \tag{35}$$

for constants v_{min} and v_{max}. The default values of these constants and all other parameters used in the models appear in Tables 8, 9.

4.3 Results

4.3.1 Tonic Model

4.3.1.1 Transitions from normal breathing to periodic breathing

For the default parameter values given in Table 8, the tonic model generates a eupneic breathing pattern (Figure 33A). Notice that KF-t is assumed to exhibit tonic activity, with a constant non-zero output $f_6(v_6) \approx 0.15$ (pink), which may result from sustained drive from elsewhere in the pons that may potentially be tuned by feedback pathways. The tonic excitatory input from KF-t promotes the long E phase duration compared to the I phase duration during normal breathing activity in the model. Experiments show that a significant reduction of the GABA inhibition to the KF leads to respiratory apneas [2], suggesting the hypothesis that such a reduction underlies respiratory disruptions as seen in RTT. When the level of sustained inhibition to KF-t in the model is reduced, KF-t produces endogenous oscillations, which in turn lead to a prolonged active phase of the post-I population on some cycles that interrupt the normal breathing pattern and would manifest as respiratory apneas in a physiological system (Figure 33B). A comparison of the KF-t output traces between the

Table 8: Default parameter values for the tonic model.

g_{Nap_i}	5.0 nS ($i \neq 5$)	g_{Nap_5}	4.72 nS	g_{K_i}	5.0 nS ($i \neq 6$)
g_{L_i}	2.8 nS ($i \neq 6$)	g_{L_6}	2.5 nS	g_{AD}	10.0 nS
g_{syn_i}	60.0 nS	e_{Na}	50.0 mV	e_{K_i}	-85.0 mV ($i \neq 6$)
e_{L_i}	-60.0 mV ($i \neq 6$)	e_{L_6}	-66.5 mV	e_{syn_e}	0.0 mV
a_1	0.03	a_2	0.875	a_3	0.9
a_5	0.11	a_6	0.15	a_{12}	0.5
a_{53}	0.25	a_{64}	0.95	α_6	1.0
b_{23}	0.42	b_{24}	0.22	b_{25}	0.09
b_{32}	0.1	b_{41}	1.0	b_{42}	0.66
b_{45}	0.101	β_6	0.05	t_{NaP}	4.0×10^3
vm_{NaP}	-40.0 mV	vm_K	-30.0 mV	vh_{NaP}	-55.0 mV
km_{NaP}	-6.0 mV	km_K	-4.0 mV	kh_{NaP}	10.0 mV
c_6	7.0×10^2	n_6	1.0×10^4	v_{AD6}	-42.0 mV
γ_i	1.0 ($i \neq 4$)	γ_4	2.0	s_i	0.0 ($\forall i$)
g_{K_6}	0.0 nS	g_{syn_e}	10.0 nS	e_{K_6}	-90.0 mV
e_{syn_i}	-75.0 mV	a_4	0.6	a_{51}	0.5
b_6	0.001	b_{31}	0.15	b_{43}	0.2
t_{AD}	2.0×10^3	v_{max}	-20.0 mV	v_{min}	-50.0 mV
k_{AD6}	0.9 mV	p_6	0.0286		

Table 9: Default parameter values for the silent model. The other parameter values for the model are as given in Table 8.

a_7	0.1	a_{74}	0.75	α_7	1.0	β_7	0.0
n_7	5.0×10^3	v_{AD7}	-50.0 mV	k_{AD7}	-0.5 mV	p_7	0.02
b_7	0.02	c_7	4.0×10^2				

two panels of Figure 33 shows that while KF-t output is elevated during the active phase of its oscillations relative to its sustained output level in the tonic case, the KF-t output becomes lower than the tonic level during the silent phases, or inter-burst intervals, in the oscillatory case. This difference causes the respiratory cycles that occur in between apneas within periodic breathing (Figure 33B) to be shorter than the normal cycle periods seen in eupneic breathing (Figure 33A), consistent with experimental observations under RTT-like conditions [2].

We used nullcline analysis to better understand which forms of inhibition to KF-t could support the generation of the activity patterns that we expect based on experimental findings and to explain why the tonic KF-t output switches to an oscillatory pattern when inhibition is reduced in a sustained way. We see in Figure 34 that KF-t, as modeled by (30), has a cubic v_6-nullcline (solid blue). The m_6-nullcline (solid red) intersects the active branch of the v_6-nullcline for default parameter values, corresponding to a stable equilibrium point at $v_6 \approx -42$ (solid grey square). Notice in Figure 34A that when we reduce the recurrent or self-inhibition within the KF-t (lower β_6), the slow nullcline intersects the middle branch of the v_6-nullcline, destabilizing the equilibrium point and leading to oscillatory behavior of KF-t. The oscillatory trajectory of the KF-t unit in this regime is overlaid in grey in the figure panel. The trajectory oscillates between the left and right stable branches of the fast v_6-nullcline. The reduction of tonic inhibition (b_6) that comes in from outside to the KF-t, in contrast, does not depend on the output of the KF-t unit and hence shifts the v_6-nullcline vertically, which does not induce a transition in the stability of the equilibrium

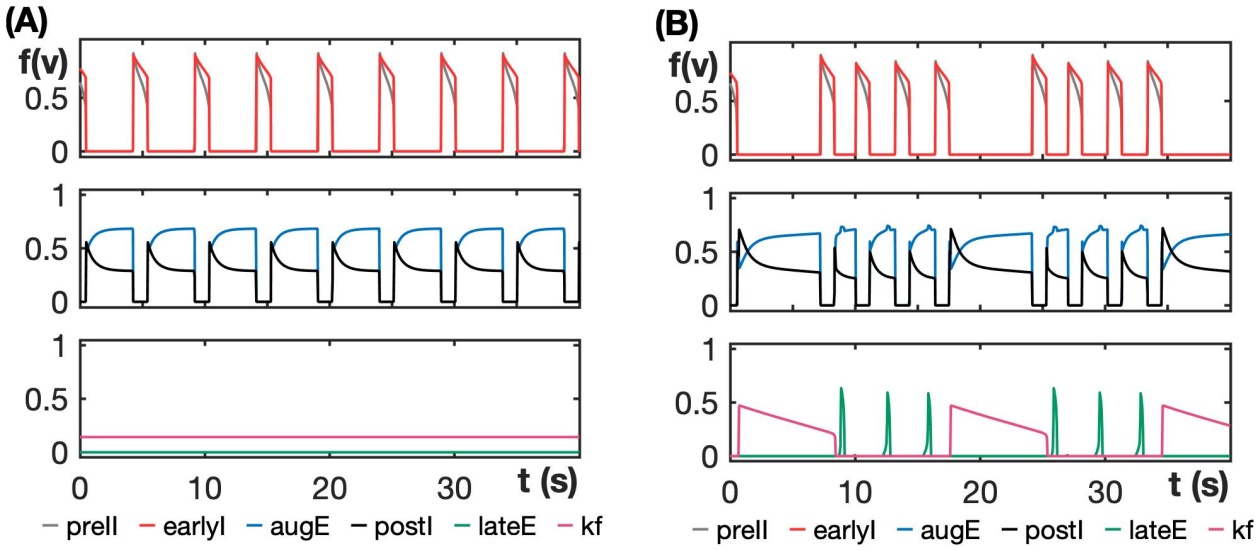

Figure 33: Tonic model output patterns. (A) Normal respiratory rhythm for the default parameter values given in Table 8. (B) Periodic breathing when recurrent inhibition is shut off, $\beta_6 = 0.0$ (simulated RTT). KF engages in slow oscillations (pink trace, bottom subplot) that drive prolonged E phases.

point and hence does not lead to KF-t oscillations (Figure 34B). Thus, we henceforth assume for this model that the recurrent inhibition strength β_6 is non-zero in the eupneic regime and decreases in the RTT condition, which represents a prediction of this work, and for simplicity we assume that the tonic inhibition strength $b_6 = 0$, since this form of inhibition is not necessary to explain experimental observations.

While Figures 33, 34 illustrate the extreme case of full removal of the inhibition to KF-t in the tonic model ($\beta_6 = 0$), Figure 35A,B show the periodic breathing exhibited by the tonic model at the partially reduced inhibition levels $\beta_6 = 0.025$, which is near the value where KF-t transitions from tonic to oscillatory behavior, and $\beta_6 = 0.015$. For these intermediate inhibition levels, although the KF-t equilibrium point lies on the middle branch of the v_6-nullcline and is unstable, its position is in between the two intersection points shown in Figure 34A; that is, it lies closer to the local maximum of the v_6-nullcline. The proximity of the equilibrium and the m_6-nullcline to this maximum means that the trajectory evolves very slowly at the end of the KF-t active phase, resulting in a longer KF-t oscillation period and larger duty cycle for larger β_6. This effect explains the prolonged KF-t oscillations in Figure 35A, B.

Even though the KF oscillations are longer for these transitional values of β_6 than for the simulated RTT condition ($\beta_6 = 0$), notice that the actual apnea durations are relatively short for these values and increase slightly as β_6 decreases (Figure 35C). How can longer KF-t active durations produce shorter apneas when apneas in the model result from KF-t drive to the post-I unit? The key to explaining this outcome is to focus on the level of KF-t output while it is active. Our simulations show that when KF-t output is above about 0.23, it supports prolonged post-I activity corresponding to apneas. When KF-t output falls below this value, closer to levels comparable to the output in the tonic regime with $\beta_6 = 0.05$, the normal respiratory rhythm takes over. For intermediate β_6 near the transition to KF-t oscillations, during each prolonged KF-t active period, KF-t output relatively quickly reaches close to the tonic level and plateaus. Thus, apnea duration is relatively short. When β_6 is reduced from there, although KF-t active phases become shorter, the amplitude of each oscillation increases (see Figure 34A) and it takes longer for KF-t output to decrement to tonic levels. Therefore, even though the KF-t burst duration decreases when inhibition is

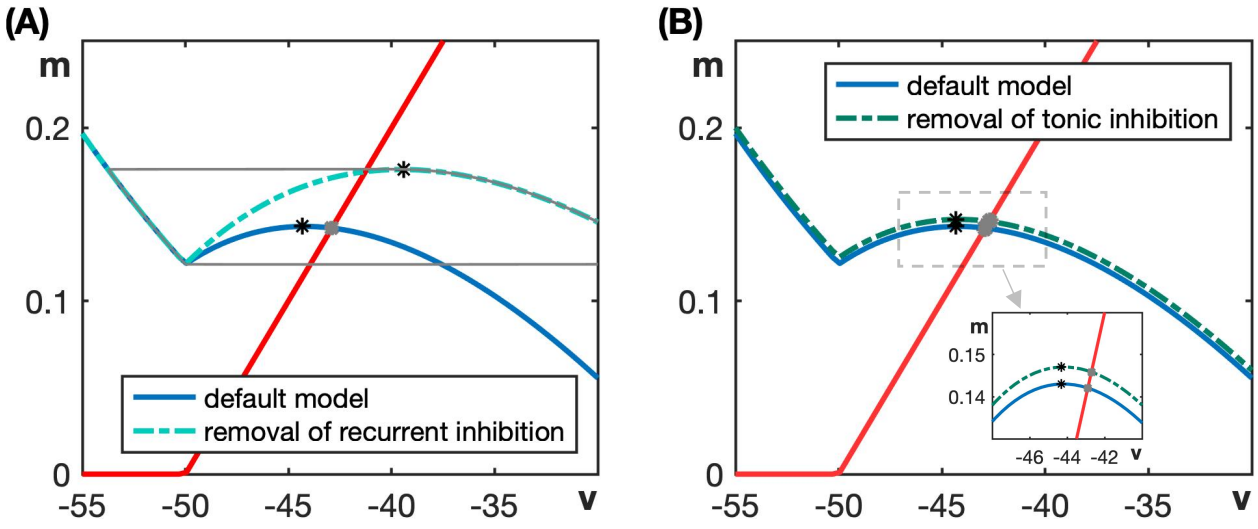

Figure 34: Tonic KF-t model in the phase plane. (A) The default model has a stable equilibrium point with $v_6 \approx -42$ (grey square), corresponding to tonic activity. When the recurrent inhibition to KF-t is removed, the local maximum (black asterisk) of the resulting v_6 nullcline (blue dashed curve) shifts to the right of the slow nullcline (red curve). Oscillations emerge in KF-t in this case (grey orbit). (B) The v_6 nullcline shifts upwards when tonic inhibition is removed as shown by the dashed blue curve. KF-t remains tonic in this case since the local maximum of the v_6 nullcline (black asterisk) remains on the left of the equilibrium point (see also zoomed view in inset).

lowered, the apnea duration increases. As a final subtlety, we note that the actual apnea duration plotted in Figure 35C (green curve) is not monotonic. This non-monotonicty arises because the apnea duration also depends on the phase of post-I activity when KF-t becomes active. Regardless of this phase, post-I stays active for a similar amount of time after KF-t activation occurs, based on the level of KF-t output. Thus, when KF-t activation occurs relatively late within the E phase, the overall apnea will be long, and this phase relation need not vary monotonically with β_6.

Since KF-t output falls to near tonic levels during each KF-t active phase, we only count the first post-I active period within each of these KF-t cycles as an apnea. Thus, the frequency of apneas increases as the recurrent inhibition β_6 is lowered from 0.025 (Figure 35D). These findings match the experimental results reported previously [2, 47].

To further study burst patterning and transitions in activity patterns when recurrent inhibition to KF-t is lowered, we modified the tonic model to include additive Gaussian noise in the voltage equation ($s_i = 1.0$ in (29) and (30)), as described in Section 4.2. Figure 36A,B show the total respiratory duration (i.e., from one E onset to the next) during the $(n+1)^{st}$ burst relative to the duration for the n^{th} burst (T_{n+1} versus T_n) for inhibition levels $\beta_6 = 0.0$ (RTT) and $\beta_6 = 0.025$ (just after the onset of KF-t oscillations) along with the same information for the default value $\beta_6 = 0.05$. During normal breathing (blue dots), this level of noise induces little variability in the respiratory period (which takes values between 4 and $5s$). In the case of RTT (red dots), respiratory periods cluster around two values, one corresponding to long apneas each having a duration of nearly $8s$ and the other to shorter normal breathing periods of approximately $3s$. The reason that the normal, non-apneic respiratory bursts in RTT are shorter than those defined for the default model parameters is that, as we pointed out with respect to Figure 35, the inter-burst KF output level within KF-t oscillations is much lower than its tonic output level at the baseline level of inhibition.

For the sub-normal inhibition level $\beta_6 = 0.025$ (grey dots) considered in Figure 36B, the durations of the longest post-I cycles are generally shorter than the prolonged apneas in the RTT case (Figure 36B, red dots), as discussed above. In the intermediate case, as we have also discussed already, each post-I cycle duration depends on the gradually declining KF-t output level (Figure 35A), and hence there is much more variability in the respiratory cycle

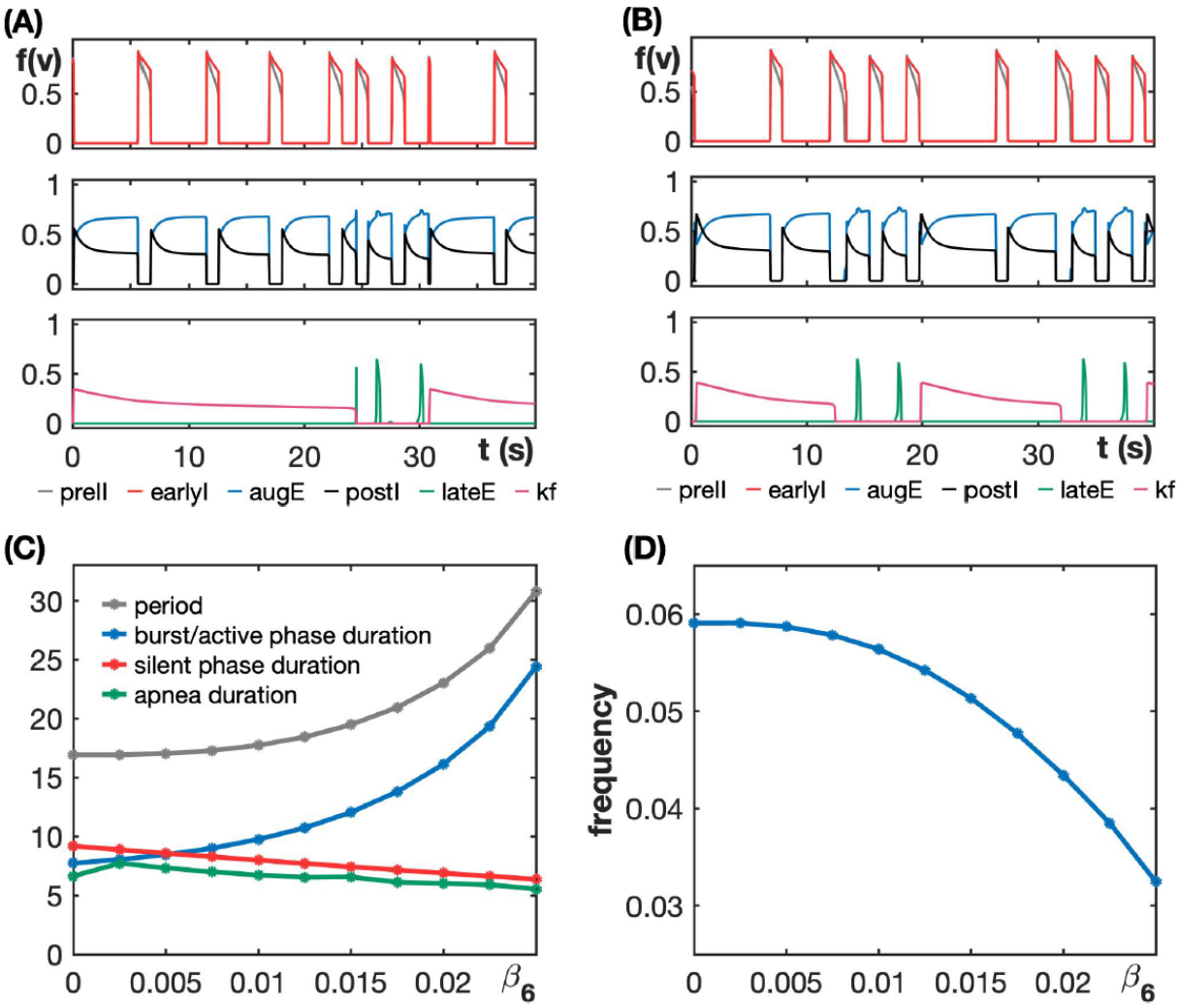

Figure 35: Tonic model output depends on the level of recurrent inhibition within the KF-t population (β_6). (A) Respiratory pattern with a recurrent inhibition strength near the point of transition of KF-t from tonic to oscillatory ($\beta_6 = 0.025$). (B) Respiratory pattern with recurrent inhibition strength $\beta_6 = 0.015$, representing an intermediate case between that shown in (A) and the RTT condition shown in Fig. 33B. (C) When β_6 is decreased, the period of KF-t oscillations and its burst or active phase duration decreases while apnea duration remains roughly the same but slightly increases. (D) Apnea frequency, defined as KF-t burst frequency (i.e., the inverse of the period of oscillations), rises as the inhibition level to KF-t decreases.

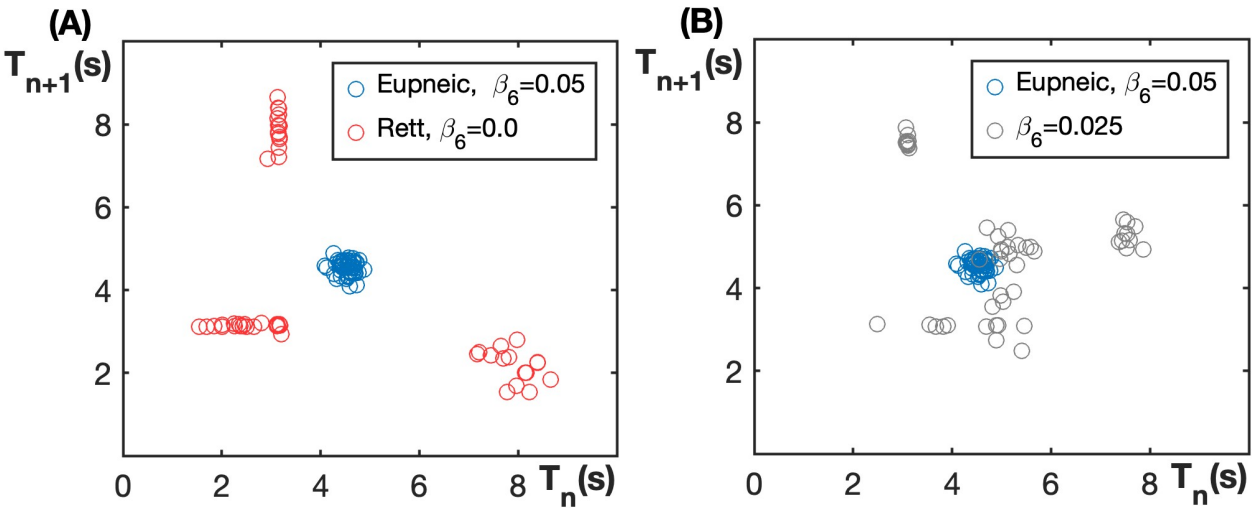

Figure 36: (A) Total respiratory cycle duration during the $(n+1)^{st}$ cycle relative to the n^{th} cycle for the tonic model with noise, $\beta_6 = 0.05$ (default value, blue dots) and $\beta_6 = 0.0$ (RTT, red dots). (B) Total respiratory cycle duration during the $(n+1)^{st}$ cycle relative to the n^{th} cycle for the tonic model with noise, $\beta_6 = 0.05$ (default value, blue dots) and $\beta_6 = 0.025$ (gray dots).

duration, with less of a clear clustering of durations, than for the extreme β_6 values. These results are consistent with the findings in [2]. In particular, Figure 5Cb in [2] shows that the effects of blocking KF $GABA_A$ receptors in wild-type rats are comparable to Figure 36A.

Past literature has shown that a systemic application of various 5-HT_{1A}R agonists can reduce the frequency of spontaneous apneas and restore normal respiratory function to various degrees in the murine model of RTT [1, 20]. These agonists can potentially boost a potassium current and thus enhance tonic inhibition within the KF [51]. They can also facilitate glycinergic neurotransmission [75] or opening of chloride channels [55], each of which may underlie an increase in recurrent inhibition. In Figure 37A, we show nullclines for the KF-t unit, comparing the RTT scenario in which KF-t is oscillatory to a case with increased recurrent inhibition. The slow nullcline (solid red) intersects the middle branch of the v_6-nullcline. This comparison repeats that given in Fig. 34A, showing that if recurrent inhibition to KF-t (β_6) increases, the tonic KF activity is restored, which implies that periodic breathing will switch back to the normal breathing pattern. On the other hand, from the RTT condition, increasing the external tonic inhibition (b_6) to KF-t does not switch the nullcline intersection off of the middle branch (Fig. 37A, dashed v_6-nullcline) and hence maintains the oscillatory KF activity, until with a sufficient increase in b_6 the intersection moves to the left branch of the v_6-nullcline (Fig. 37A, dash-dotted v_6-nullcline) and stabilizes. This stable equilibrium point location implies that KF-t becomes fully inactive and no longer supports normal breathing.

Overall, these simulations indicate that a reduction in the recurrent inhibition to the KF neurons that provide tonic input to the ventromedullary neurons can trigger episodic apneas and drive breathing irregularities. In this scenario, reduction of tonic inhibition to the KF does not produce similar effects. A prediction emerging from this analysis is that drugs that boost endogeneous inhibition would be more efficacious at reversing breathing irregularity than drugs that boost or produce an exogenous tonic inhibitory drive.

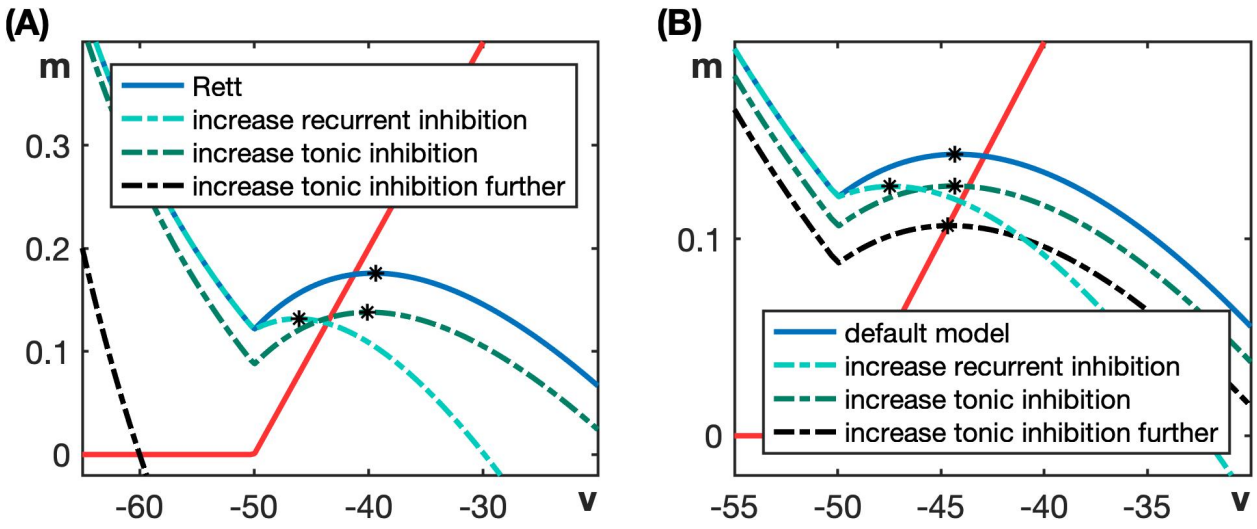

Figure 37: (A) Starting with oscillatory KF-t (RTT), $\beta_6 = 0.0$. When recurrent inhibition, β_6, is increased from 0.0, KF-t becomes tonic. When tonic inhibition, b_6, is increased, KF-t remains oscillatory. When it's increased further, it becomes silent. (B) Tonic model with inhibition increased above baseline. When recurrent inhibition is increased, KF-t remains tonic with its equilibrium point on the right branch of the v_6-nullcline but the point moves to a lower v_6 value, corresponding to less KF output. When tonic inhibition is increased, the equilibrium point moves to the middle branch and destabilizes, and thus a transition from tonic KF output to KF oscillations occurs.

4.3.1.2 Emergence of active expiration

Expiration is a process that becomes active in conditions of increased respiratory drive. Exposure to low oxygen (hypoxia) or high carbon dioxide levels (hypercapnia) triggers active expiration with the recruitment of abdominal muscles during the late part of the E2 phase (i.e., late expiration, or late-E) to improve pulmonary ventilation [8]. Decreased KF activity is known to play a role in the emergence of late-E abdominal activity [45, 9]. Moreover, [47] showed that systemic administration of the 5-HT_{1A}R agonist NLX-101 increases the respiratory drive, elevating the respiratory frequency and causing the appearance of active expiration (late-E activity) under resting conditions.

We first consider the phenomenon of late-E activation. The tonic model has an excitatory synaptic connection from KF-t to post-I and an inhibitory connection from post-I to late-E (see Figure 32A). This architecture suggests that when there is a reduction in KF activity, a decrease in post-I output will result, which in turn will reduce the post-I dependent inhibition to late-E. If KF-t output is reduced sufficently, then late-E should start spiking. This logic leads us to consider the input-related mechanisms by which 5-HT_{1A} agonists may strengthen inhibition in the KF. In Figure 37B, we analyze the effect of increasing each of the two different types of inhibition to KF-t. Initially, the KF-t unit has a stable equilibrium at $v_6 \approx -42$. When we increase recurrent inhibition, the slow nullcline (shown in red) still intersects the modified v_6-nullcline (shown in dashed blue) on its right branch, leading to a stable tonic equilibrium (Figure 37B). In this case, however, the stable equilibrium has a lower v_6 value than originally. Therefore, we see that increasing recurrent inhibition, β_6, reduces the tonic output level $f_6(v_6)$ of KF-t and eventually causes KF-t output to turn off. If we instead turn on and increase tonic inhibition to KF-t ($b_6 > 0$), notice in Figure 37B that at first a small reduction in the v_6-coordinate of the equilibrium point and hence in $f_6(v_6)$ occurs, but this is not sufficient to promote late-E activity. With an additional increase in b_6, the equilibrium point moves to the middle branch of the v_6-nullcline and KF-t becomes oscillatory, leading to continued late-E suppression. Therefore, to see the emergence of late-E spiking in the tonic model, we gradually increased the recurrent inhibition (β_6) to KF-t and kept $b_6 = 0$.

For the parameter values given in Table 8, there is no late-E activation, as seen in Figure 33A. An emergence and quantal acceleration of late-E activity with increasing β_6 are illustrated in Figure 38. When we increase β_6 to 0.3 (Figure 38A), late-E spikes once during every three post-I bursts. For $\beta_6 = 0.6$ (Figure 38B), late-E spikes once during every two post-I bursts. Increasing β_6 to 1.8 (Figure 38C) results in a late-E spike during every post-I burst. The increasing late-E spiking frequency with respect to β_6 is summarized in Figure 38D. This figure plots the ratio of the number of late-E spikes to the number of post-I bursts on the y axis. For example, at $\beta_6 = 1.2$, the ratio is 2/3, corresponding to two late-E spikes during every three post-I bursts.

In the experiments of [47], this increase was largely due to a decrease in the post-I duration while the duration of pre-I oscillations remained roughly the same. Under increases in β_6, our tonic model reproduces these findings; indeed, we can see in Fig. 38 that the E phase becomes shorter as β_6 increases from panel A to panel C (see middle subplots), due to the reduced KF excitation to post-I, while the I phase duration essentially does not change (see top subplots). These results are quantified across a range of β_6 values in Figure 39. Overall, the fact that our model results parallel the data from previous experiments indicates that the assumptions we have made in constructing the tonic model, including the importance of recurrent inhibition within the KF-t populations, are plausible and suggests that our findings may be useful to guide future experiments.

4.3.2 Silent Model

In contrast to the tonic model, the silent model has two KF units: KF-t and KF-s. The values for all of the parameters that appear in both the tonic model and the silent model remain the same as in the tonic model (Table 8), while the values of parameters specific to the silent model are given in Table 9. With these values, KF-t is tonic, with a stable critical point for which $f_6(v_6) \approx 0.15$, and KF-s is silent, with a stable critical point below v_{min} such that its output is zero. Note that the lack of output of the KF-s unit does not reflect an inability to activate; rather, this unit remains quiescent in the baseline model tuning relevant for eupneic rhythm generation, just as the late-E population does. The bursting pattern of

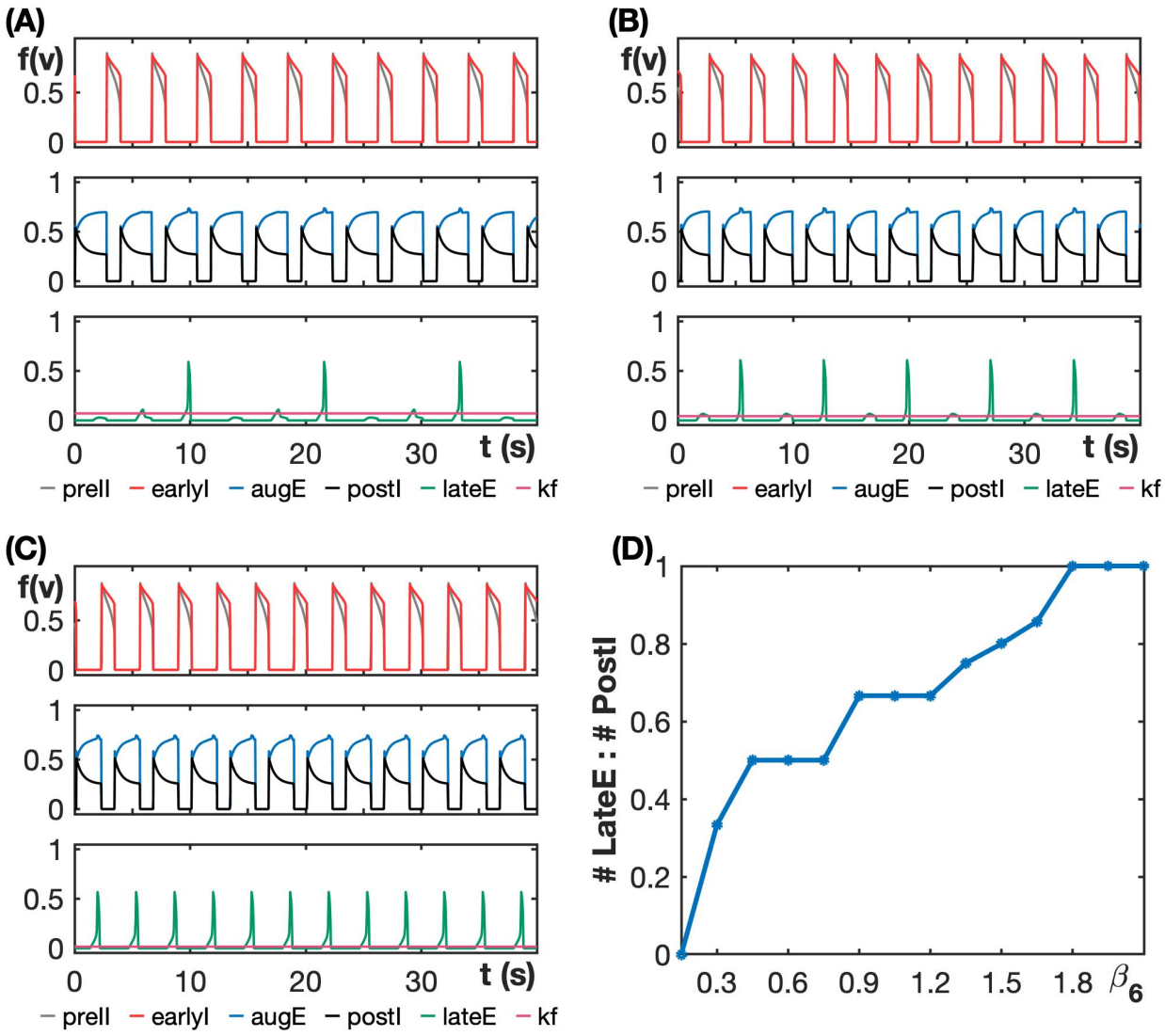

Figure 38: Quantal acceleration of late-E in the tonic model. (A)-(C) Burst patterns exhibited by the tonic model at different inhibition levels. (A) $\beta_6 = 0.3$. (B) $\beta_6 = 0.6$. (C) $\beta_6 = 1.8$. (D) The late-E spiking frequency increases with respect to the recurrent inhibition strength β_6.

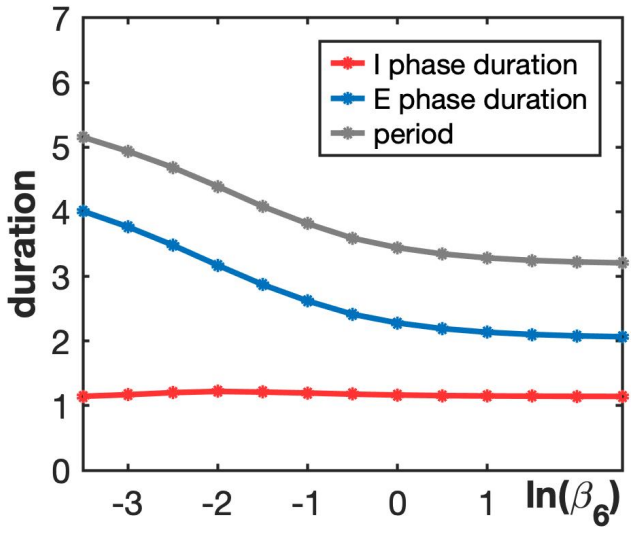

Figure 39: Durations of inspiration and expiration and overall respiratory period vary with $\ln(\beta_6)$ in the tonic model. The gradual decrease in the period with increasing β_6 comes from a drop in the E phase duration, whereas the I phase duration remains roughly constant.

the silent model for the default parameter values naturally matches that of the tonic model since KF-s is silent (Figure 40). Hence, our analysis of the role of KF in active expiration resulting from increases in inhibition within the KF, and the corresponding Figures 37B, 38 and 39, apply for the silent model as well.

As with the tonic model, we consider nullclines for the silent model as a means to determine what forms of inhibition of the KF allow the model to match experimental findings on RTT-like respiratory patterns. Importantly, in the silent model, we assume that if the KF-s population becomes active, then it will provide drive to post-I, and in our analysis, we manipulate the inhibition to KF-s. This approach makes the silent model a distinct alternative to the tonic model. If we instead varied inhibition to the KF-t unit in the context of the silent model, then the KF-s unit would simply remain silent and hence would be irrelevant, so our results would trivially match the previous subsection.

Nullcline analysis shows that for the silent model, KF-s transitions to oscillatory behavior when we reduce the tonic inhibition strength to the KF-s unit, b_7 (Figure 41A), because this

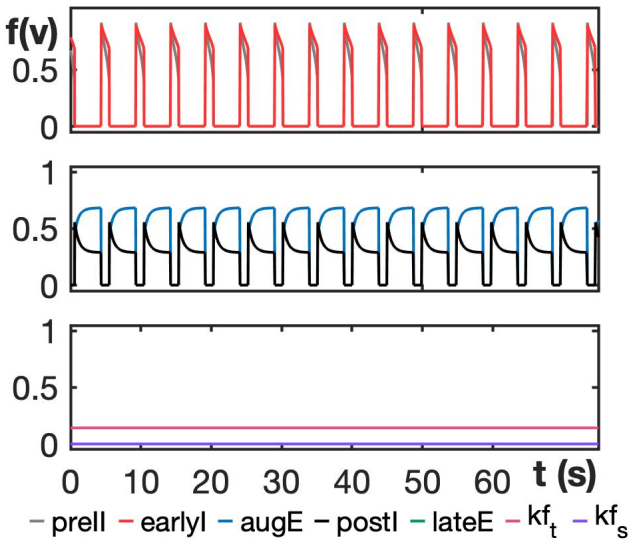

Figure 40: Eupneic respiratory rhythm exhibited by the silent model for default parameter values given in Tables 8, 9.

loss of inhibition causes the model to no longer have a stable fixed point in the silent phase. The same does not happen with recurrent inhibition, since KF-s is initially silent and hence receives no recurrent inhibitory input regardless of β_7; for simplicity, we fix $\beta_7 = 0$ in our default parameter set. In the subsequent subsections, we will consider the effects of reduced tonic inhibition in the silent model.

Before considering effects of reduced inhibition in the silent model, we note that once tonic inhibition is reduced, increasing it restores the normal breathing rhythm (Figure 41B). On the other hand, starting from the case of reduced tonic inhibition and introducing a small amount of recurrent inhibition keeps KF-s in an oscillatory state, and a further increase in β_7 causes the v_7-nullcline to become monotonic. Once this occurs, the KF-s system has a stable critical point at a v_7 level such that $f_7(v_7) > 0$, corresponding to a tonic KF-s output (Figure 41B). Overall, in contrast to the tonic model, which suggests that inhibition within the KF is recurrent and hence depends on KF activity levels, the silent model suggests that inhibition to KF respiratory neurons is sustained and arrives from an outside source. Future experimental determination of the nature of inhibition to KF respiratory neurons will help

to distinguish which, if any, of our models is consistent with the biological reality.

When the tonic inhibition, b_7, to KF-s is reduced in the silent model, KF-s activity transitions from quiescent, with a stable critical point on the left branch of the v_7-nullcline, to oscillatory, with an unstable critical point on the middle branch (Fig. 41A). The oscillations in KF-s provide oscillatory drive to post-I and produce a periodic breathing pattern similar to that observed in RTT. At the minimal value of $b_7 = 0.0$, which we will refer to as our silent model representation of RTT, the apneic breathing pattern exhibited by the model is shown in Figure 42A. Notice that during RTT, the model does not produce late-E activation. This absence contrasts with the tonic model in Figure 33B, where we see late-E spiking during RTT-like apneas. The onset of periodic breathing, as b_7 is reduced in the silent model, occurs at $b_7 \approx 0.015$ and the burst pattern just below this inhibition level is shown in Figure 42B. In Figure 42C,D we plot the period of KF oscillations, the apnea duration and the apnea frequency as the inhibition strength b_7 is varied. The apnea duration remains roughly constant and is non-monotonic in b_7 (shown in green Figure 42C), whereas the apnea frequency increases as b_7 decreases (Figure 42D). These results agree qualitatively with the results for the tonic model (Figure 35C,D).

Recall from Figure 33B and Figure 35A,B that as the inhibition level decreases in the tonic model, the KF-t burst/active phase duration decreases while the silent phase duration remains roughly the same. This causes the period of KF-t oscillations to decrease and apnea frequency to increase. In the silent model, however, we see in Figure 42A,B that the period of KF-s oscillations decreases mainly due to the reduction of silent phase duration of KF-s when b_7 is lowered from 0.015. This effect arises because with less inhibition, the v_7-nullcline in the silent phase moves farther away from the m_7-nullcline (Fig. 41A), which yields less of a delay in the jump-up to the active phase. Therefore, this is another distinction between the tonic and silent models.

To study burst patterning in the silent model, we modified the model by adding Gaussian noise with mean 0 and standard deviation 1 by setting $s_i = 1$ in (29) and (30). Figure 43 shows the total respiratory duration during the $(n+1)^{st}$ burst relative to the duration for the n^{th} burst (T_{n+1} versus T_n) for inhibition levels $b_7 = 0.0$ (RTT) and $b_7 = 0.014$ (just after the onset of KF-s oscillations) and $b_7 = 0.02$, the default value. The model did not show

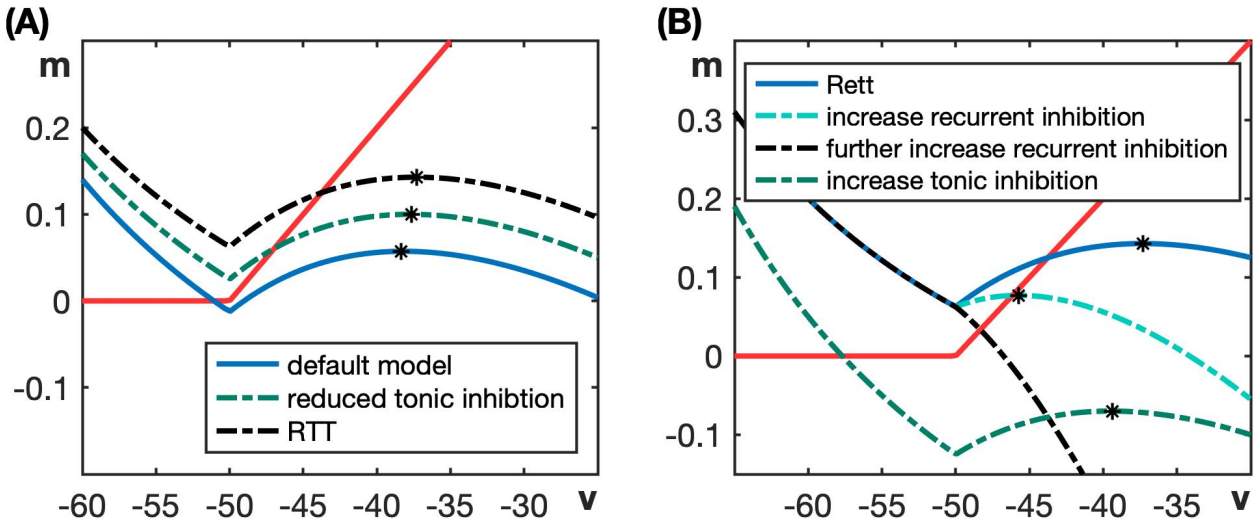

Figure 41: Phase plane analysis of impacts of altered inhibition in the silent model. (A) When the tonic inhibition to KF-s is removed, the slow nullcline (red curve) intersects the middle branch of the resulting v_7-nullcline (green dashed curve). Therefore, oscillations emerge in KF-s in this case. (B) Starting with oscillatory KF-s (RTT scenario), when tonic inhibition is increased, KF-s becomes silent (i.e., nullclines intersect on left branch of dashed green v_7-nullcine). When recurrent inhibition is increased, KF-s remains oscillatory (intersection on middle branch of cyan dashed v_7-nullcline). When it is increased further, KF-s becomes tonic (montonic black v_7-nullcline).

much variability in respiratory periods (blue dots in Figure 43) during normal breathing conditions, as expected. Notice in Figure 42A that during KF-s oscillations, the inter-burst KF-s output matches the KF-s output level (≈ 0) during normal breathing. Therefore, in the RTT regime in this model, we expect that the breathing cycle durations in between apneas will remain the same as in the eupneic case. Aligning with this expectation, in the RTT case, we observe two different respiratory cycle durations (red dots in Figure 43): apneas with duration $\approx$ 9s and normal breathing cycles during the silent phase of each KF-s oscillation, which match the cycle duration with the default model. This perseverance of the normal cycle duration even in the RTT condition differs from the activity in the tonic model since, in the tonic model under RTT conditions, the cycle duration in between apneas is shorter than the default respiratory breathing period.

For an intermediate value of inhibition in the silent model, for example $b_7 = 0.014$, the apneas are shorter compared with the RTT case (Fig. 43). We see in Fig. 42C, however, that apnea duration is clearly non-monotonic in b_7. Notice from Fig. 42A,B that for different levels of b_7, the initial KF-s activation can occur at different phases within the ongoing post-I active phase. For certain intervals of b_7, this phase shift changes smoothly, but as b_7 is decreased through other values, KF-s activation can switch from occurring early in every n^{th} post-I cycle to late in every $(n-1)^{st}$ cycle, yielding increased apnea durations. To avoid this arbitrary phase relation, we next introduced a putative excitatory connection from the post-I unit to the KF-s unit and examined its effects.

Including this excitatory drive does not change the eupneic breathing pattern exhibited by the silent model, since KF-s is silent in this regime (Figure 40). The effects of varying inhibition on the v_7-nullcline and its intersection with the m_7-nullcline also remain unchanged, and thus we focus on effects of varying tonic inhibition to KF-s. As was the case without the drive from post-I to the KF-s unit, when the inhibition strength parameter b_7 is reduced sufficiently, the KF-s unit produces endogenous oscillations, which in turn leads to a perturbation in the normal breathing rhythm (Figure 44A). The transition of KF-s from the silent to the oscillatory state occurs now occurs at $b_7 \approx 0.02$ and the bursting pattern exhibited at this inhibitory level is shown in Figure 44B. Notice that in this case, post-I activation on certain cycles immediately recruits KF-s activation, without any phase lag. This effect

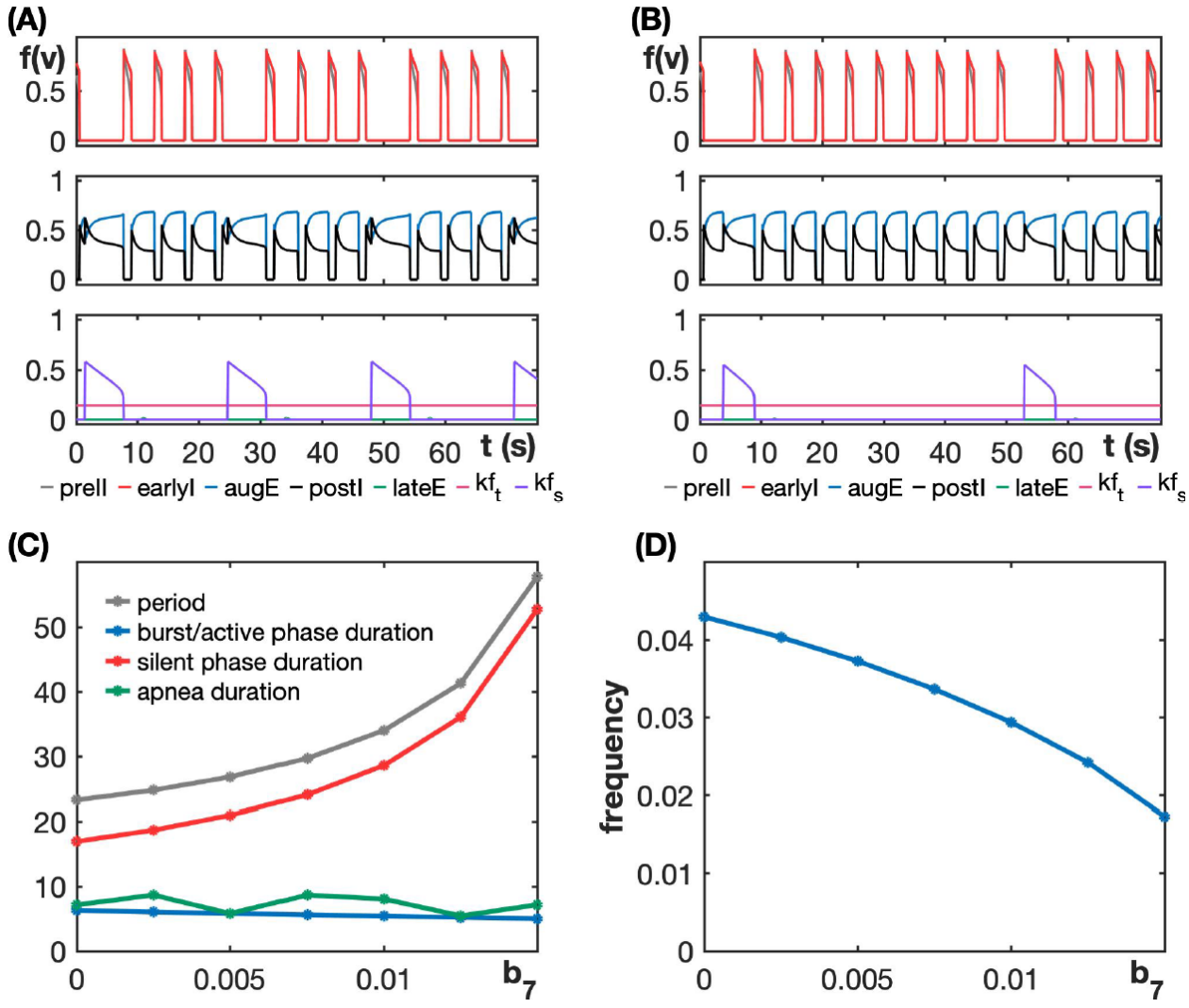

Figure 42: The silent model exhibits apneas, with preservation of normal cycle durations in between them, as tonic inhibition is reduced. (A) Periodic breathing exhibited by the model for $b_7 = 0.0$ (RTT). (B) Respiratory pattern at an inhibition value near the point of transition of KF-s from tonic to oscillatory ($b_7 = 0.014$). (C) The period of KF-s oscillations, KF-s burst/active phase duration, silent phase duration and apnea duration with respect to b_7. (D) Apnea frequency, which is equal to the inverse of the period of KF-s oscillations, increases as the inhibition level to KF-s decreases.

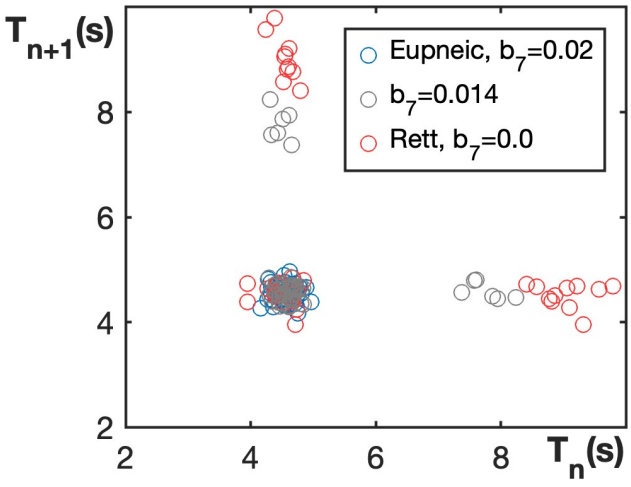

Figure 43: Total respiratory duration during the $(n+1)^{st}$ burst relative to that in the n^{th} burst for silent model 1 with noise with $b_7 = 0.02$ (default value), $b_7 = 0.014$, and $b_7 = 0.0$ (RTT).

smooths out the dependence of apnea duration on b_7 and results in a monotonic relationship.

The results related to apnea duration and frequency (Figure 44C,D) qualitatively agree with those for the tonic model (Figure 35C,D) as well as for the silent model without feedback from post-I to KF-s (Figure 42C,D). The excitatory connection from post-I to KF causes the apnea duration to increase steadily as b_7 is decreased in this augmented model (Figure 44C) and also results in a step-like decline in KF-s period as b_7 decreases. This pattern represents a quantal effect: an approximately constant plateau occurs when KF-s activates once every n post-I cycles for fixed n, and then a step down to a lower period occurs when b_7 becomes low enough that KF-s can activate once every $n-1$ post-I cycles.

Figure 45 shows the burst patterning of the augmented silent model with Gaussian noise. This figure is comparable with Figure 43 in that the cycle durations between apneas carry over from the normal case to the cases with reduced inhibition levels. The new feature here is that the additional synaptic connection makes the cycle durations less variable than they were previously.

Finally, we do not separately consider the emergence of active expiration in the silent

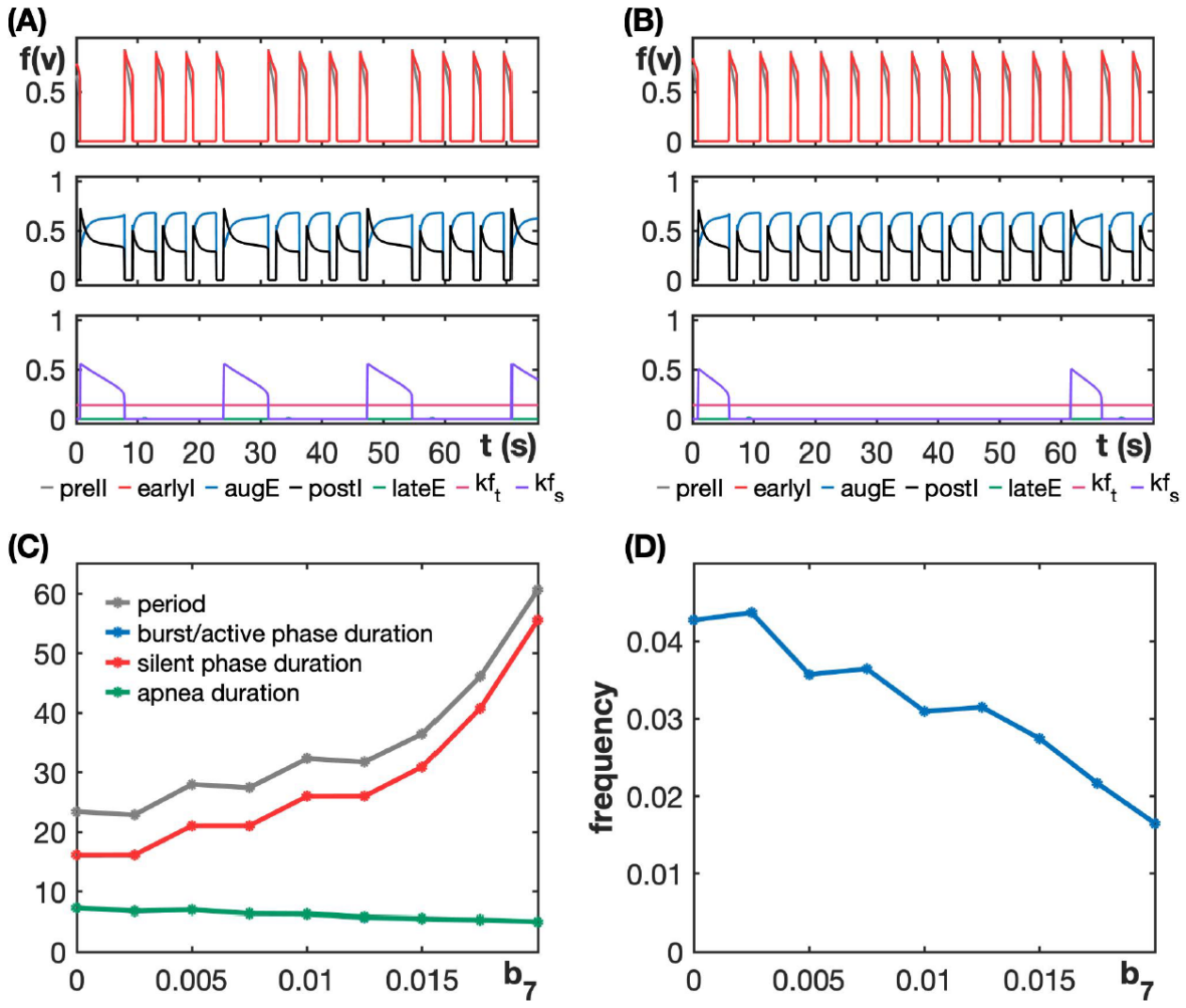

Figure 44: The inclusion of excitatory drive from post-I to KF-s reduces the variability in cycle durations. (A) Periodic breathing exhibited by the model for $b_7 = 0.0$ (RTT). (B) Respiratory pattern at an inhibition value near the point of transition of KF-s from tonic to oscillatory ($b_7 = 0.02$). (C) The period of KF-s oscillations, KF-s burst/active phase duration, KF-s silent phase duration, and apnea duration with respect to b_7. In this case, the blue curve is identical to and completely hidden by the green curve, due to the connection from post-I to KF-s. (D) Apnea frequency increases non-monotonically as the inhibition level to KF-s decreases.

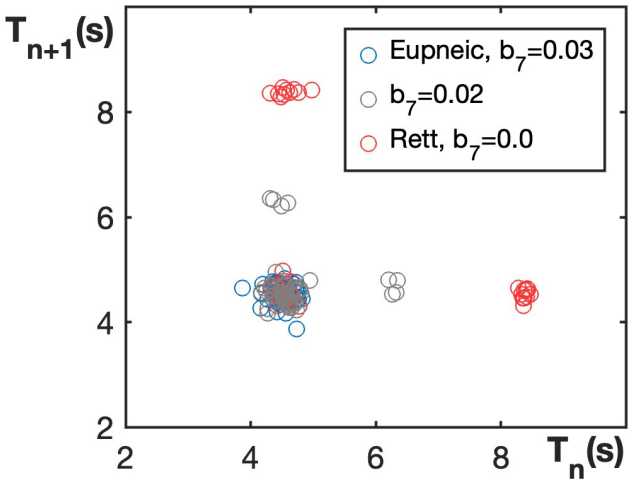

Figure 45: Total respiratory duration during the $(n+1)^{st}$ burst relative to that in the n^{th} burst when noise is included, with $b_7 = 0.03$ (default value), $b_7 = 0.02$ and $b_7 = 0.0$ (RTT).

model. Since the KF-s population is silent by default, increasing the inhibition to KF-s from its baseline state would have no effect, while increasing the inhibition to KF-t with KF-s remaining silent would simply repeat the results that we obtained with the tonic model as described in Section 4.3.1.2.

4.4 Discussion

In this work, we consider a family of respiratory circuit models, which include the KF, designed to be minimal in terms of the complexity of the neural units, endogenous neuronal dynamics, and synaptic connections involved. We show that two of these models capture the central experimental findings on the response of respiratory patterns to manipulations involving the KF: (1) reduction of GABA-mediated inhibition to KF neurons induces periodic or intermittent breathing with apneas [2, 20]; (2) durations of apnea events are maintained or lengthen with reductions in the inhibition level to KF [2, 20]; (3) when intermittent breathing

occurs, increases in KF inhibition can induce eupnea [2, 1]; (4) from the eupneic state, additional increases in KF inhibition causes quantal activation of abdominal late-E activity [47]. Within this computational framework, we identify the synaptic connections that are compatible with the experimental results and obtain predictions about KF properties, circuit organization, and respiratory neuron behaviors under various conditions that could be tested to distinguish the two models and to check their validity. Our work builds on a series of assumptions and logical inferences, supported by the literature, which we now discuss before turning to the predictions that we derive as well as model limitations and future directions.

4.4.1 KF as a source of breathing irregularities

Intermittent breathing, such as observed in RTT, manifests as breathing that is periodically disrupted by apneic episodes. These apneas are accompanied by abnormally strong constrictor activity to the upper airways driven by motor neurons that exhibit a post-inspiratory activity pattern during regular breathing [93, 1, 82]. Post-inspiratory activity strongly depends on excitatory outputs from the KF [79, 25]. Disruption of inhibitory transmission in the KF, causing disinhibition, leads to periodic breathing with periods of excessive post-inspiratory activity to the larynx [20, 2]. These findings provide strong (yet indirect) evidence that intermittent breathing can result from periodic KF overactivation on a time scale slower by an order of magnitude than respiration. Such a slow timescale suggests that the emerging oscillations can originate within the KF, resulting from a combination of intrinsic neuronal properties and synaptic inputs to the region. Our work illustrates some possible mechanisms that could give rise to this patterned KF activity.

4.4.2 Baseline activity in the KF

KF contains a large population of glutamatergic neurons that connects with the rCPG [37]. A recurrent excitatory network endowed with spike frequency adaptation properties (i.e., exhibiting a reduction in firing frequency within ongoing spiking activity) has the capacity to produce population-based rhythmic bursting. Changing parameters can transition such a system to a bursting regime regardless of whether it initially lies in a silent or tonically

active state with a steady activity level. Therefore, we consider two basic KF network configurations. In the first configuration (*tonic model*), KF is represented by a single population with a tonic activity pattern under baseline conditions, which can transition into a bursting regime by relevant perturbations. In the second configuration (*silent model*), KF includes a subpopulation that is quiescent at baseline, either due to a a balance of endogenous currents that is inadequate to induce spiking without boosts in excitatory drive or due to suppression by ongoing inhibition, but starts producing oscillatory activity as parameters change. In the latter case, we assume that there is another population of neurons in the KF that always produces tonic output to provide the necessary excitatory drive to the rCPG. Still, unlike in the tonic model, this population does not become oscillatory under the manipulations that we consider.

4.4.3 Sources of GABA-mediated inhibition

Experiments show that reduced GABAergic inhibition in the KF leads to the emergence of slow oscillations modulating rCPG activity and causing breathing irregularities [2]. Depending on the KF network configuration, we infer different origins of this inhibition. Specifically, in the tonic model, this inhibition appears to be recurrent. Although we implement this recurrence as self-inhibition in our minimal model, this recurrent inhibition is a reduced representation of a scenario in which the KF population excites inhibitory interneurons that in return provide feedback inhibition. The location of these inhibitory interneurons is not specified by our model. One can speculate that these neurons can represent a local inhibitory subpopulation providing negative feedback within the KF for self-regulation. Alternatively, they could be located in another site, such as the BötC or the parabrachial nucleus, proved to have recurrent connectivity with KF [30, 36, 90]. In contrast, in the framework of the silent model, the GABAergic inhibition in KF is predicted to take the form of a tonic or sustained drive, probably originating externally to the KF; for example, the NTS is known to send feedforward inhibitory projections to the KF and hence could represent the source of this input [65, 49].

4.4.4 Mechanisms of 5-HT$_{1A}$ inhibition

Experimental evidence indicates that manipulating 5-HT$_{1A}$ receptors in the KF produces changes in respiratory activity comparable to the changes induced by modulating GABAergic inhibition [20, 2]. Specifically, 5-HT$_{1A}$ antagonists evoke intermittent breathing while 5-HT$_{1A}$ agonists can reduce breathing irregularities or even restore eupnea [20, 15]. While serotonergic inputs originate outside of the KF (e.g., in the raphe nucleus), their functional effects, mediated by 5-HT$_{1A}$ receptors, are compatible with both the recurrent and tonic inhibition scenarios. Specifically, tonic inhibition could be membrane hyperpolarization due to the activation of 5-HT$_{1A}$R-coupled potassium channels [60], which is compatible with the silent model. On the other hand, another known impact of 5-HT$_{1A}$R activation is the enhancement of glycinergic inhibition in neurons that express the GlyR α3 subunit [75]. This mechanism could be involved in altering the recurrent inhibition provided by glycinergic interneurons. Potentially, the interneuron population could coexpress both GABA and glycine and thus could mediate the effects of both GABAergic and serotonin-modulated recurrent inhibition in the tonic model. Finally, our results on the emergence of active expiration (Section 4.3.1.2) suggest that 5-HT$_{1A}$ agonists may strengthen the recurrent inhibition within a tonic population of KF neurons.

4.4.5 Additional predictions and implications

Both the tonic and silent models, with appropriate forms of inhibitory connections, capture the set of benchmarks that we initially imposed. While it is not feasible to use these models for quantitative predictions, our modeling framework can allow us to propose experimental designs that can be deployed to test and select between these models. For starters, the structural differences that distinguish the two models themselves represent predictions. Specifically, the tonic model assumes that the KF would feature prominent recurrent inhibition, through which increased activity in KF neurons strengthens the inhibitory inputs that these neurons receive. In contrast, the silent model predicts an important role for a sustained inhibitory input to KF from an outside source, as well as the presence of a subpopulation of KF neurons that exhibit little or no activity under control states of eupneic respiration.

The network configurations predicted by the two models also have different implications for abdominal activity during periods of intermittent breathing when inhibition in KF is compromised. Indeed, in the tonic model, reduction in recurrent inhibition transforms steady KF activity into an oscillatory regime with periods of overactivity inducing temporary apnea, adaptation to near a normal activity level, and then periods of silence (see Fig. 35A, B). During the latter periods, KF does not provide excitation to post-inspiratory neurons in BötC, which results in a disinhibition of expiratory neurons in pFL and evokes abdominal late-E activity that drives active expiration (Fig. 35A, B). In contrast, in the silent model, oscillations in KF emerge in a previously silent population while the steady activity of the tonic KF subpopulation remains unaltered. Therefore, conditions for the abdominal activity breakthrough are never created (see Fig. 42A, B). Interestingly, some apneic events in some RTT mice are accompanied by abdominal activation without a clearly corresponding late-E activation [1], but this result does not suffice to distinguish the two models, as late-E activity could be present yet phase-shifted by other factors.

Typically, experiments relating to respiration in RTT and under compromised KF inhibition compare across two groups, such as control versus experimental mice or wild-type versus knock-out mice. Using computational models allows us to generate predictions about the effects that we expect from gradual changes that induce states in-between the extreme endpoints. In the tonic model, reductions in inhibition to KF induce a regime of KF oscillations with a long epoch of sustained KF activity within each cycle. In this regime, apneas are interspersed with respiratory cycles with a mix of durations, including some slightly longer and some slightly shorter than those seen under control conditions (Figures 35, 36). Further decreases in inhibition are predicted to shorten the KF active duration and the oscillation period, with a small increase in apnea duration and a regularization of cycle durations in between apneas. The silent model points to a different pattern of changes with progressive decrease in inhibition to KF. In this model, we see that when the onset of apneas occurs, the durations of the cycles in between the apneas are fairly stereotyped and match those seen in control conditions (Figures 42, 43). Decreasing inhibition allows apnea durations to show a net increase, but unlike in the tonic model, this relationship is non-monotonic. If we hypothesize the inclusion of an additional excitatory connection from BötC neurons

to the quiescent KF population, then we recover a more consistent phase relation between expiratory BötC and KF activity, which regularizes the trend in apnea durations (Figures 44, 45).

In summary, the tonic and silent models are both consistent with published experiments but can be differentiated in terms of their predictions about KF activity in baseline conditions, inhibitory pathways that impact KF activity, and alterations in respiratory patterns resulting from decreases as well as increases in inhibition to the KF. Finally, an interesting possibility that should also be kept in mind is that the tonic and silent models may both be valid but in different regimes of respiratory circuit function; for example, changes under vagotomy may alter KF activity in a way that corresponds to switching between these two models. These possibilities require experimental verification to be validated.

4.4.6 Model limitations and future directions

By starting from a minimal modeling framework, we were able to use analytical tools, including analysis of nullclines in certain phase planes, to argue against the presence of specific combinations of KF endogenous dynamics and forms of inhibition to the KF, while also providing a proof of principle that certain other configurations can capture a range of experimental findings and merit further consideration. A natural next computational step would be to address the limitations of this minimal modeling framework by implementing the proposed circuit arrangements in a more complete model featuring populations of spiking neurons with a full complement of known transmembrane ion currents in each of the constituent brain regions as well as more biologically detailed synaptic interactions. Past work has shown that endowing KF neurons with intrinsic bursting capabilities and also assuming the presence of certain synaptic interactions between neurons in the KF, in the parabrachial nucleus (PBN), and in the BötC produces a circuit that also produces eupneic respiratory output and captures the effects of vagotomy as well as periodic breathing following reduction of GABAergic inputs to the KF [95]. Because these ideas were considered previously and represent a specific set of assumptions that go beyond our minimal framework (e.g., involvement of a PBN component), we did not consider these properties in this work. While

the results that we obtained show that endogeneous KF oscillations are not necessary to explain experimental findings, since previous studies have demonstrated the presence of KF neutrons with phasic discharge patterns both with and without vagotomy [61], another natural future direction will be to compare these frameworks directly and to explore possible ways to integrate these models. Of course, future experimental work to directly derive more information about the intrinsic properties of KF neurons, their endogenous dynamics, and the synaptic interactions in which they are involved would be an invaluable complement to computational approaches. Hopefully the findings from this work and other computational studies can guide these experimental investigations in productive directions.

4.4.7 Conclusions

Our modeling results, tuned to capture experimental observations, highlight the importance of the KF neurons in maintaining eupneic breathing and support the hypothesis that disruptions in KF activity can contribute to the emergence of pathological respiratory phenotypes. Our predictions suggest two different possible circuit organizations that may be present within the KF, with neuronal subpopulations displaying distinct intrinsic characteristics and synaptic connections. These new possibilities can foster future experimental and pre-clinical studies examining in detail the proposed features and their involvement in pathological states associated with breathing irregularities, such as RTT.

5.0 Conclusion

Many of the reduced mathematical models that exhibit square-wave bursting yield transitions to an alternative pseudo-plateau bursting pattern with small parameter changes. This susceptibility to activity change could represent a problematic feature in settings where the release events triggered by spike production are necessary for function. In the second chapter, we analyze how model bursting and other activity patterns vary with changes in a timescale associated with the conductance of a fast inward current. Specifically, using numerical simulations and dynamical systems methods, such as fast-slow decomposition and bifurcation and phase-plane analysis, we demonstrate and explain how the presence of a slow negative feedback associated with a gradual reduction of a fast inward current in these models helps to maintain the presence of spikes within the active phases of bursts. Therefore, although such a negative feedback is not necessary for burst production, we find that its presence generates a robustness that may be important for function.

In the following chapter, we aim to develop models that display ramping bursting pattern exhibited by the neurons in the pre-BötC. We first explore two mechanisms that help control the spike frequency and burst shape using phenomenological models : (1) AHP, which controls the strength of hyperpolarization between spikes (2) SPK, which modulates the spike height in the burst. [3] developed a model that considers the biological mechanism corresponding to AHP modulation. Following the SPK mechanism, in this work, we present the dynamic spike height model which exhibits ramping dynamics. Furthermore, we study the robustness of the ramping pattern and analyze its transitions to other activity patterns with parameter changes. Some of the parameters in the model, including the extra cellular potassium concentration and the sodium conductance, may change during the development of mammals. A future direction would be to more broadly explore how changes to these parameters affect the bursting pattern.

In last project, we study the dynamics of the Kölliker-Fuse nucleus (KF), which is part of the parabrachial complex. KF participates in the generation of eupnea under resting conditions and the control of active abdominal expiration when increased ventilation is required.

Moreover, dysfunctions in KF neuronal activity are believed to play a role in the emergence of respiratory abnormalities seen in Rett syndrome (RTT), a progressive neurodevelopmental disorder associated with an irregular breathing pattern and frequent apneas. Relatively little is known, however, about the intrinsic dynamics of neurons within the KF and how their synaptic connections affect breathing pattern control and contribute to breathing irregularities. In the fourth chapter, we use a reduced computational model to consider several dynamical regimes of KF activity paired with different input sources to determine which combinations are compatible with known experimental observations. We further build on these findings to identify possible interactions between the KF and other components of the respiratory neural circuitry. Specifically, we present two models that both simulate eupneic as well as RTT-like breathing phenotypes. Using nullcline analysis, we identify the types of inhibitory inputs to the KF leading to RTT-like respiratory patterns and suggest possible KF local circuit organizations. When the identified properties are present, the two models also exhibit quantal acceleration of late-expiratory activity, a hallmark of active expiration featuring forced exhalation, with increasing inhibition to KF, as reported experimentally. Hence, these models instantiate plausible hypotheses about possible KF dynamics and forms of local network interactions, thus providing a general framework as well as specific predictions for future experimental testing.

This work displays a variety of bursting activity exhibited by the respiratory neurons in mammalian brainstem. In the second chapter, we present square wave and pseudo-plateau bursting patterns, while third chapter introduces the ramping dynamics, all of which are observed in pre-BötC neurons. The final project introduces the respiratory rhythm and also explores the longer than normal expiratory phase activity seen in RTT mice. In this work, geometric singular perturbation theory serves as the primary tool for analyzing all the models used to study these distinct activity patterns, as they are multiple-timescale models. We also use dynamical systems methods such as bifurcation analysis and nullcline analysis to further analyze the robustness of the bursting patterns with respect to parameter changes. Notice, however, that in all the models, with the exception for the dynamic spike height model in chapter 3, there was clear division of timescales into fast and slow components which made the analysis easier. It was trickier to analyze the timescale of h_{2Na} in the dynamic spike

height model as the timescale division was less clear.

It is important to realize that, unlike the standard fast-slow models, biological models can have more than two timescales in them and have components that evolve at different timescale in different regions of the phase space. All the reduced mathematical models analyzed in the second chapter have clear separation of variables into fast and slow variables. However, we show that having an additional inactivation variable that evolves at a particular rate could improve robustness. The dynamic spike height model in chapter 3 which exhibits ramping bursts have components varying at three timescales, and the second inactivation gate associated with the sodium current changes timescale at different burst instances. This model is also an example where the timescale of a variable changes with parameter variations. These results demonstrate that when we take into account the additional timescale features in these models, deviating from the standard fast-slow systems, we observe more interesting and biologically realistic bursting patterns.

Appendix A Non-dimensionalization

Non-dimensionalization of a model is a form of scaling that expresses the rate of change of each model variable as the product of a dimensionless speed and a function of constrained magnitude. The dimensionless speeds are appropriate to compare across all variables to evaluate their relative rates of change. In this process, each original variable is represented as a fraction of a nominal value, often taken to be the maximum of the range over which that variable is observed to evolve in the dynamics of interest. The equations are then expressed in terms of these non-dimensional fractions and the magnitudes of the corresponding unitless speeds represent their timescale constants; note that gating variables are already non-dimensional fractions with maximal values of one, so no scaling is needed for their equations. We derive the scaled equations in detail for the generic endocrine model (6)–(7); a similar derivation leads to the scaled equations for all the other models in this work, which are merely stated for reference.

A.1 Generic endocrine model

Note that the variable n for the generic endocrine model (6)–(7) is a gating variable. Hence, we represent the other two variables v and c as $v = V\,Q_v$ and $c = C\,Q_c$, with dimensionless variables V and C, respectively. Here, Q_v and Q_c are constants, representing the nominal values of v and c, respectively. We now derive differential equations for V and C using that $V' = \frac{1}{Q_v}\,v'$ and $C' = \frac{1}{Q_c}\,c'$. We start with the equation for V':

$$
\begin{aligned}
V' &= \tfrac{1}{Q_v}\, v' \\
&= -\tfrac{1}{Q_v\, c_m}\, \big(I_{Ca}(v) + I_K(v,n) \\
&\qquad + I_{K(Ca)}(v,c)\big) \\
&= -\tfrac{1}{Q_v\, c_m}\, \Big(g_{ca}\, m_\infty^2(v)\, (v - e_{ca}) \\
&\qquad + g_k\, n\, (v - e_k) \\
&\qquad + g_{kca}\, \frac{c^4}{c^4 + k_s^4}\, (v - e_k)\Big) \\
&= -\tfrac{1}{c_m}\, \Big(g_{ca}\, m_\infty^2(V\, Q_v)\, (V - \bar{e}_{ca}) \\
&\qquad + g_k\, n\, (V - \bar{e}_k) \\
&\qquad + g_{kca}\, \frac{C^4}{C^4 + \bar{k}_s^4}\, (V - \bar{e}_k)\Big),
\end{aligned}
$$

where $\bar{e}_{ca} = \frac{1}{Q_v}\, e_{ca}$, $\bar{e}_k = \frac{1}{Q_v}\, e_k$, and $\bar{k}_s = \frac{1}{Q_c}\, k_s$. We now define $g_{\max} = \max\,(g_{ca},\, g_k,\, g_{kca})$, so that the rescaled equation for V becomes

$$
\begin{aligned}
V' &= -\tfrac{g_{\max}}{c_m}\, \Big(\tfrac{g_{ca}}{g_{\max}}\, m_\infty^2(V\, Q_v)\, (V - \bar{e}_{ca}) \\
&\qquad + \tfrac{g_k}{g_{\max}}\, n\, (V - \bar{e}_k) \\
&\qquad + \tfrac{g_{kca}}{g_{\max}}\, \frac{C^4}{C^4 + \bar{k}_s^4}\, (V - \bar{e}_k)\Big),
\end{aligned}
$$

which is of the form

$$
V' = R_v\, f(V, n, C),
$$

with f an $\mathcal{O}(1)$ function, because at least one of the ratios $\frac{g_{ca}}{g_{\max}}$, $\frac{g_k}{g_{\max}}$, and $\frac{g_{kca}}{g_{\max}}$ equals 1; indeed, the form of $m_\infty(V\, Q_v)$, defined in (7), does not significantly affect the speed associated with the calcium current as it is a function on the unit interval. Hence, $R_v = g_{\max}/c_m$ is the constant that represents the timescale on which V evolves. We apply similar steps to the other two equations so that we obtain dimensionless model equations of the form

$$
\begin{cases}
V' &= R_v\, f(V, n, C), \\
n' &= R_n\, g(V, n, C), \\
C' &= R_c\, h(V, n, C),
\end{cases}
$$

where the functions f, g and h are all $\mathcal{O}(1)$.

Recall that n is already in non-dimensional form and it has timescale constant $R_n = 1/\tau_n$; using the same arguments as for $m_\infty(V\,Q_v)$, the expression $n_\infty(V\,Q_v)$ (also defined in (7)) has a negligible effect on the order of the right-hand side for n.

The non-dimensonalization process for the C'-equation is less straightforward. Applying similar steps, however, we find:

$$\begin{aligned} C' &= \tfrac{1}{Q_c}\,c' \\ &= -\tfrac{f_c}{Q_c}\,(\alpha\,I_{Ca}(v) + k_p\,c) \\ &= -\tfrac{f_c}{Q_c}\,(\alpha\,g_{ca}\,m_\infty^2(V\,Q_v)\,(V\,Q_v - e_{ca}) \\ &\qquad + k_p\,C\,Q_c) \\ &= -\tfrac{f_c\,\alpha\,Q_v\,g_{ca}}{Q_c}\,\Big(m_\infty^2(V\,Q_v)\,(V - \bar{e}_{ca}) \\ &\qquad + \tfrac{k_p\,Q_c}{\alpha\,Q_v\,g_{ca}}\,C\Big)\,. \end{aligned}$$

The right-hand side of this equation suggests $R_c = f_c\,\alpha\,Q_v\,g_{ca}/Q_c$, but this is only true if the two components in the brackets sum to an $\mathcal{O}(1)$ function. We again use the form of $m_\infty(V\,Q_v)$ to claim that the first component is $\mathcal{O}(1)$. Note that the second component is linear in C with coefficient $f_c\,k_p/R_c = 0.015/R_c$ for the default parameters given in Table 1. Hence, as long as R_c is at least of order 10^{-2}, this coefficient is at most 1, as required.

During the analysis, we find that $v \in [-65, 10]$ and $c \in [0, 2]$. Therefore, we choose nominal values $Q_v = 100$ and $Q_c = 2$ for the variables v and c, respectively. the default parameters from Table 1 then give:

$$\begin{aligned} R_v &= \frac{\max\,(g_{ca},\,g_k,\,g_{kca})}{c_m} \approx 716, \\ R_n &= \tau_n^{-1} \approx 33, \\ R_c &= \frac{f_c\,\alpha\,Q_v\,g_{ca}}{Q_c} \approx 1.7 \end{aligned} \tag{36}$$

Note that R_c is sufficiently large to justify the factorization for the C'-equation.

A.2 Sodium-potassium minimal model

Using the same calculations as done for the generic endocrine model above, we obtain the dimensionless sodium-potassium minimal model (8)–(9). Since both n and s are gating variables in this model, only the equation for v needs to be scaled. Again setting $v = V\,Q_v$, we find

$$\begin{cases} V' &= -\frac{g_{\max}}{c_m}\left(\frac{g_L}{g_{\max}}\,(V-\bar{e}_L)\right. \\ &\qquad + \frac{g_{na}}{g_{\max}}\,m_\infty(V\,Q_v)\,(V-\bar{e}_{na}) \\ &\qquad + \frac{g_k}{g_{\max}}\,n\,(V-\bar{e}_k) \\ &\qquad + \frac{g_{km}}{g_{\max}}\,s\,(V-\bar{e}_k) \\ &\qquad \left. - \frac{1}{g_{\max}\,Q_v}\,I\right), \\ n' &= \frac{1}{\tau_n}\,(n_\infty(V\,Q_v)-n)\,, \\ s' &= \frac{1}{\tau_s}\,(s_\infty(V\,Q_v)-s)\,, \end{cases}$$

where $\bar{e}_L = \frac{1}{Q_v}\,e_L$, $\bar{e}_{na} = \frac{1}{Q_v}\,e_{na}$, $\bar{e}_k = \frac{1}{Q_v}\,e_k$, and $g_{\max} = \max(g_L, g_{na}, g_k, g_{km})$. Note that the actual timescale constants for the sodium-potassium minimal model do not depend on the chosen value for Q_v; indeed, $m_\infty(V\,Q_v)$ as defined in (9) has no significant effect for the same reasons as in the generic endocrine model, and we can assume Q_v is chosen such that $1/(g_{\max}\,Q_v) \leq 1$. By setting all parameters to their default values given in Table 2, we find timescale constants

$$\begin{aligned} R_v &= \frac{\max(g_L, g_{na}, g_k, g_{km})}{c_m} &&\approx 20.0, \\ R_n &= \tau_n^{-1} &&\approx 6.6, \\ R_s &= \tau_s^{-1} &&\approx 0.005, \end{aligned}$$

which represent the relative speeds of v, n and s, respectively.

A.3 Minimal Chay–Keizer model

The equations in terms of dimensionless variables for the minimal Chay–Keizer model (10)–(11) are derived in complete analogy to the other derivations. The only difference is that the time constant in the equation for the gating variable n is a function of v, denoted $\tau_n(v)$. Hence the timescale constant for n depends on v in this case. Since $v \in [-65, 0]$ and $c \in [0, 6]$, we choose nominal values $Q_v = 100$ for $V = \frac{1}{Q_v}\, v$ and $Q_c = 6$ for $C = \frac{1}{Q_c}\, c$. Observing from the analysis that $\tau_n(v) = \tau_n(V\, Q_v) \in [10,\, 20]$, we find for the default parameters given in Table 3:

$$\begin{aligned} R_v &= \frac{\max\left(g_{ca},\, g_k,\, g_{kca}\right)}{c_m} &&\approx\quad 1.8, \\ R_n &= \frac{1}{\tau_n(V\, Q_v)} &&\in\quad [0.05,\, 0.1], \\ R_c &= \frac{f_c\, \alpha\, Q_v\, g_{ca}}{Q_c} &&\approx\quad 0.004. \end{aligned}$$

Note that the timescale constant R_c for the slow variable c requires $f_c\, k_p / R_c \leq 1$, but with $f_c = 0.0058$ and $k_p = 0.00513\,\mathrm{ms}^{-1}$ in Table 3, this is certainly satisfied if R_c is of order 10^{-3}.

A.4 Butera model

Again in complete analogy to the earlier models, we find timescale constants representing the relative speeds for the variables v, n, and p in the Butera model (12)–(13). Based on the default parameters values given in Table 4, we find timescale constants:

$$\begin{aligned} R_v &= \frac{\max\left(g_L,\, g_{na},\, g_k,\, g_{nap},\, g_{ton}\right)}{c_m} &&\approx\quad 1.33, \\ R_n &= \tau_n^{-1} &&\approx\quad 0.17, \\ R_p &= \frac{1}{\tau_p(V\, Q_v)} &&\in\quad [10^{-4},\, 10^{-3}]. \end{aligned}$$

A.5 AHP model

We find timescale constants representing the relative speeds for the variables v, h_{Na}, m_{Na}, h_{NaP}, m_{NaP}, n, h_{AHP} and m_{AHP} in the AHP model 19-21. Based on the default parameters values given in Table 6, we find timescale constants:

$$
\begin{aligned}
R_v &= \frac{\max\left(g_{Na},\, g_{NaP},\, g_{AHP},\, g_K,\, g_L,\, g_{syn}\right)}{c_m} &&\approx\ 6.11,\\
R_{h_{Na}} &= \frac{1}{\tau_{h_{Na}}(V\,Q_v)} &&\in\ [0.157,\, 3.06]\\
R_{m_{Na}} &= \frac{1}{\tau_{m_{Na}}(V\,Q_v)} &&\in\ [4.00,\, 13.88]\\
R_{h_{NaP}} &= \frac{1}{\tau_{h_{NaP}}(V\,Q_v)} &&\in\ [10^{-4},\, 0.012]\\
R_{m_{NaP}} &= \frac{1}{\tau_{m_{NaP}}(V\,Q_v)} &&\in\ [1.00,\, 64.46]\\
R_n &= \frac{1}{\tau_n(V\,Q_v)} &&\in\ [0.049,\, 0.796]\\
R_{h_{AHP}} &= \frac{1}{\tau_{h_{AHP}}(V\,Q_v)} &&\in\ [0.001,\, 0.082]\\
R_{m_{AHP}} &= t^{-1}_{m_{AHP}} &&\approx\ 0.2
\end{aligned}
$$

A.6 SPK model

We find timescale constants representing the relative speeds for the variables v, h_{Na}, m_{Na}, h_{NaP}, m_{NaP}, n, h_{SPK}, h_{2SPK} and m_{SPK} in the AHP model 22, 23. Based on the default parameters values given in Table 5, we find timescale constants:

$$
\begin{aligned}
R_v &= \frac{\max\left(g_{Na},\, g_{NaP},\, g_{AHP},\, g_K,\, g_L,\, g_{syn}\right)}{c_m} &&\approx 6.11, \\
R_{h_{Na}} &= \frac{1}{\tau_{h_{Na}}(V\,Q_v)} &&\in [0.156,\, 4.59] \\
R_{m_{Na}} &= \frac{1}{\tau_{m_{Na}}(V\,Q_v)} &&\in [4.0,\, 19.89] \\
R_{h_{NaP}} &= \frac{1}{\tau_{h_{NaP}}(V\,Q_v)} &&\in [10^{-4},\, 0.021] \\
R_{m_{NaP}} &= \frac{1}{\tau_{m_{NaP}}(V\,Q_v)} &&\in [1.0,\, 148.89] \\
R_n &= \frac{1}{\tau_n(V\,Q_v)} &&\in [0.048,\, 0.841] \\
R_{h_{SPK}} &= t^{-1}_{h_{SPK}} &&\approx 2.0 \\
R_{h_{2SPK}} &= \frac{1}{\tau_{h_{2SPK}}(V\,Q_v)} &&\in [0.001,\, 0.144] \\
R_{m_{SPK}} &= t^{-1}_{m_{SPK}} &&\approx 2.0
\end{aligned}
$$

A.7 DSPK model

We find timescale constants representing the relative speeds for the variables v, h_{Na}, h_{2Na}, m_{Na}, h_{NaP}, m_{NaP} and n in the DSPK model 24, 25. Based on the default parameters values given in Table 7, we find timescale constants.

When $g_L = 3.5$, timescale constants are :

$$\begin{aligned}
R_v &= \frac{\max\left(g_{Na},\, g_{NaP},\, g_{AHP},\, g_K,\, g_L,\, g_{syn}\right)}{c_m} \approx 6.94, \\
R_{h_{Na}} &= \frac{1}{\tau_{h_{Na}}(V\,Q_v)} \in [0.24,\, 0.744] \\
R_{h_{2Na}} &= \frac{1}{\tau_{h_{2Na}}(V\,Q_v)} \in [10^{-4},\, 0.011] \\
R_{m_{Na}} &= \frac{1}{\tau_{m_{Na}}(V\,Q_v)} \in [4.0,\, 4.78] \\
R_{h_{NaP}} &= \frac{1}{\tau_{h_{NaP}}(V\,Q_v)} \in [10^{-4},\, 0.002] \\
R_{m_{NaP}} &= \frac{1}{\tau_{m_{NaP}}(V\,Q_v)} \in [1.0,\, 3.5] \\
R_n &= \frac{1}{\tau_n(V\,Q_v)} \in [0.13,\, 0.49]
\end{aligned}$$

When $g_L = 4$, timescale constants are :

$$\begin{aligned}
R_v &= \frac{\max\left(g_{Na},\, g_{NaP},\, g_{AHP},\, g_K,\, g_L),\, g_{syn}\right)}{c_m} \approx 6.94, \\
R_{h_{Na}} &= \frac{1}{\tau_{h_{Na}}(V\,Q_v)} \in [0.167,\, 1.7] \\
R_{h_{2Na}} &= \frac{1}{\tau_{h_{2Na}}(V\,Q_v)} \in [10^{-4},\, 0.11] \\
R_{m_{Na}} &= \frac{1}{\tau_{m_{Na}}(V\,Q_v)} \in [4.0,\, 8.45] \\
R_{h_{NaP}} &= \frac{1}{\tau_{h_{NaP}}(V\,Q_v)} \in [10^{-4},\, 0.006] \\
R_{m_{NaP}} &= \frac{1}{\tau_{m_{NaP}}(V\,Q_v)} \in [1.0,\, 19.20] \\
R_n &= \frac{1}{\tau_n(V\,Q_v)} \in [0.06,\, 0.7]
\end{aligned}$$

When $g_L = 4.6$, timescale constants are :

$$
\begin{aligned}
R_v &= \frac{\max\left(g_{Na},\, g_{NaP},\, g_{AHP},\, g_K,\, g_L\right),\, g_{syn}\right)}{c_m} &&\approx 6.94, \\
R_{h_{Na}} &= \frac{1}{\tau_{h_{Na}}(V\,Q_v)} &&\in [0.166,\, 2.07] \\
R_{h_{2Na}} &= \frac{1}{\tau_{h_{2Na}}(V\,Q_v)} &&\in [10^{-4},\, 0.2] \\
R_{m_{Na}} &= \frac{1}{\tau_{m_{Na}}(V\,Q_v)} &&\in [4,\, 9.94] \\
R_{h_{NaP}} &= \frac{1}{\tau_{h_{NaP}}(V\,Q_v)} &&\in [10^{-4},\, 0.0079] \\
R_{m_{NaP}} &= \frac{1}{\tau_{m_{NaP}}(V\,Q_v)} &&\in [1.0,\, 28.84] \\
R_n &= \frac{1}{\tau_n(V\,Q_v)} &&\in [0.058,\, 0.739]
\end{aligned}
$$

Appendix B Supplementary Figures

Supplementary figures for Chapter 2 and 3.

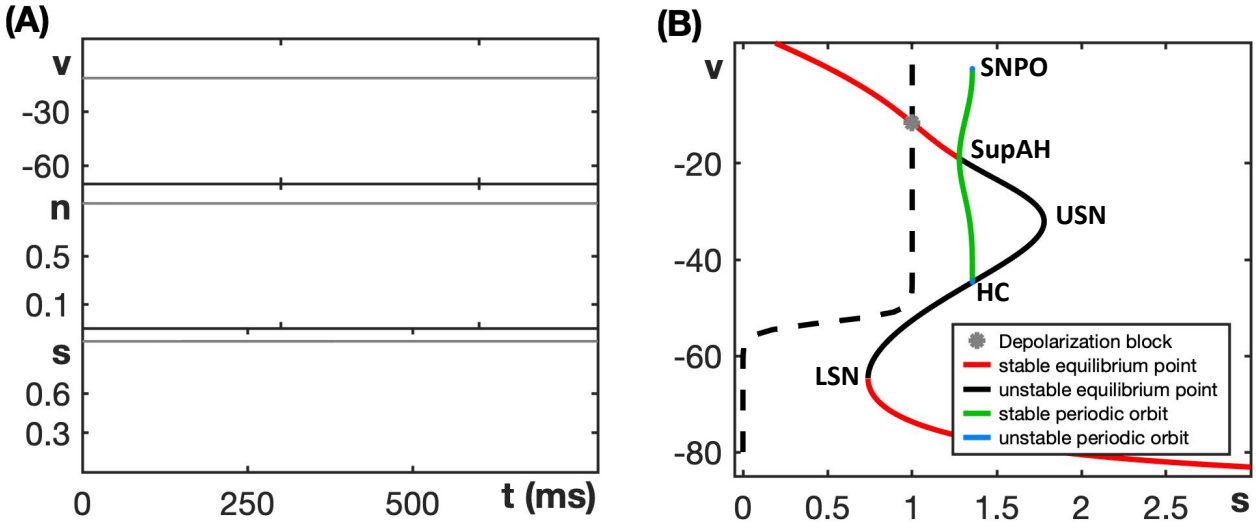

Figure 46: (A) Depolarization block exhibited by the sodium-potassium minimal model (8)-(9) resulting from a full-system stable steady state $(v, n, s) \approx (-11.5, 0.93, 1.0)$ at elevated voltage for $g_{na} = 35$. (B) Bifurcation diagram of the model's fast system associated with (A). The stable steady state lies where the fast subsystem equilibrium curve intersects the s-nullcline (dashed black).

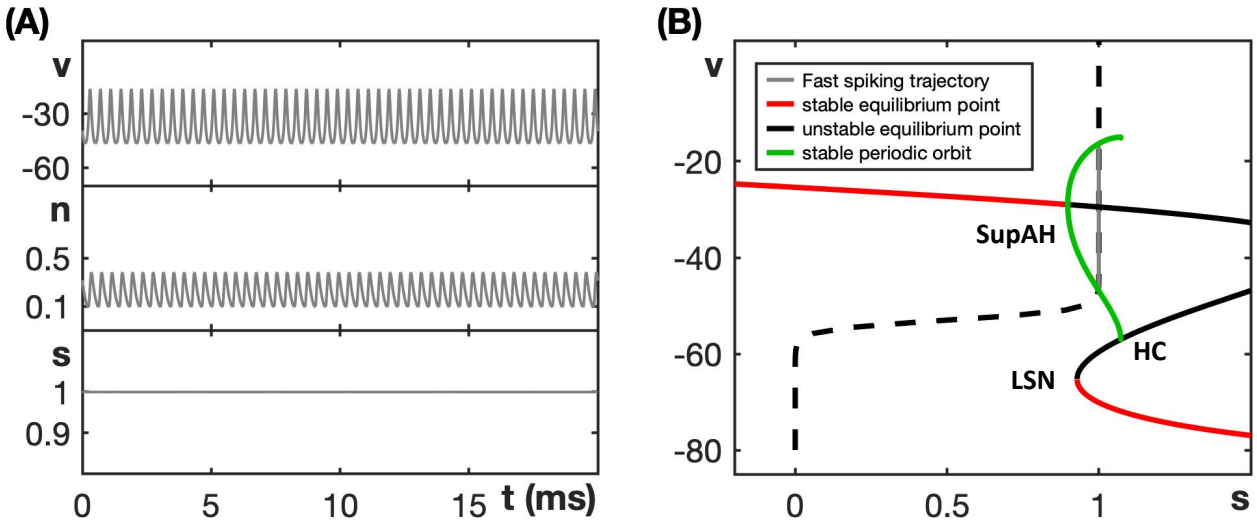

Figure 47: (A) Fast spiking exhibited by the modified sodium-potassium minimal model (8)-(9), (15)-(16) resulting from a full-system stable periodic orbit with $s \approx 1.0$ for $g_{na} = 39$ and $1/\tau_h = 13$. (B) Bifurcation diagram of the model's fast system associated with (A).

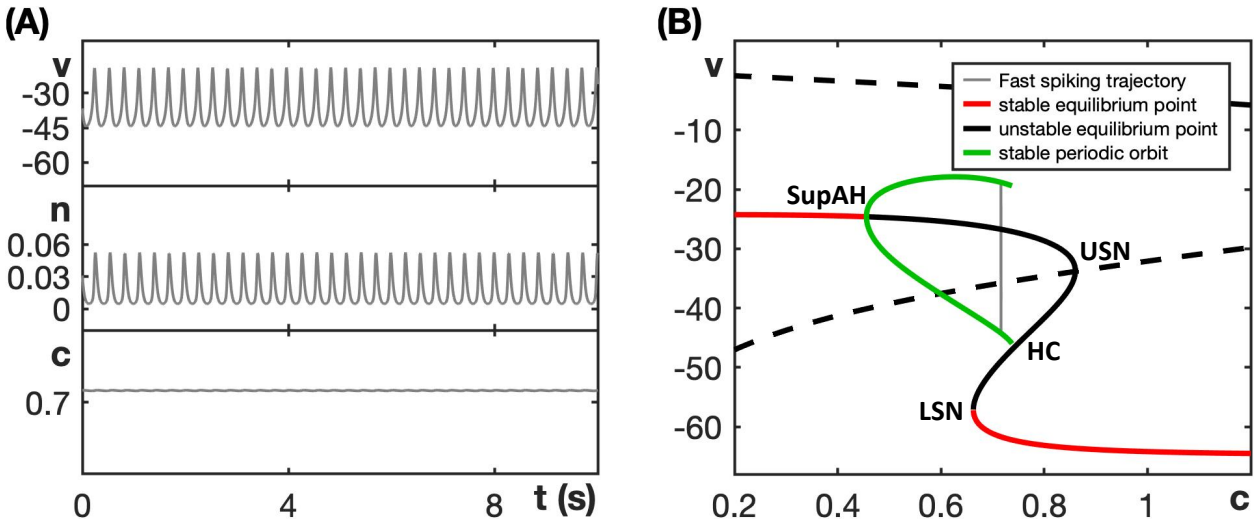

Figure 48: Fast spiking exhibited by the generic endocrine model (6)-(7) resulting from a full-system stable periodic orbit with $c \approx 0.7$ for $g_{ca} = 0.81$ and $\alpha = 2$. (B) Bifurcation diagram of the model's fast system associated with (A).

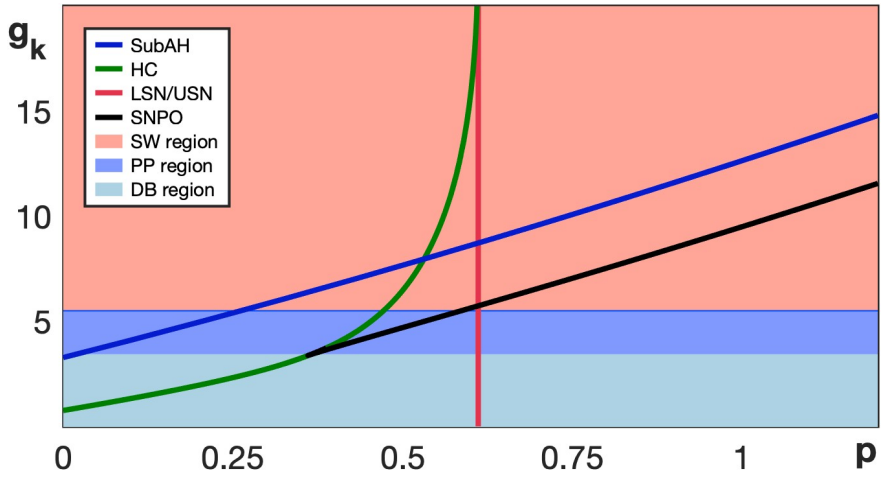

Figure 49: Two-parameter bifurcation diagram of the butera model (12)-(13) with respect to g_k.

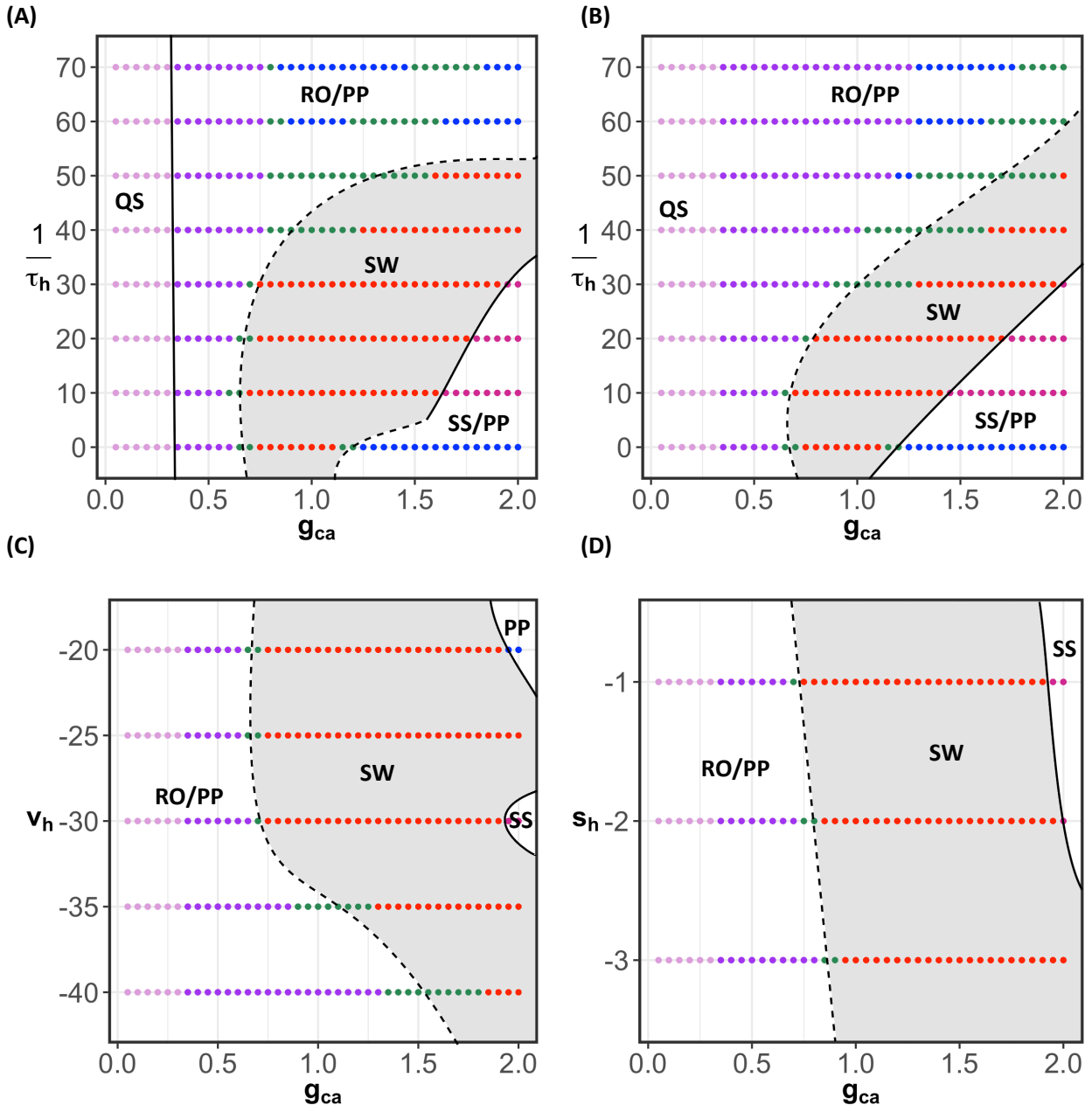

Figure 50: Two-parameter bifurcation diagrams of the modified generic endocrine model (6)-(7) and (14),(16), with respect to (A) g_{ca} and $1/\tau_h$ for $v_h = -30$ and $s_h = -1$; (B) g_{ca} and $1/\tau_h$ for $v_h = -35$ and $s_h = -1$; (C) v_h and g_{ca} for $1/\tau_h = 30$ and $s_h = -1$; (D) s_h and g_{ca} for $v_h = -30$ and $1/\tau_h = 30$.

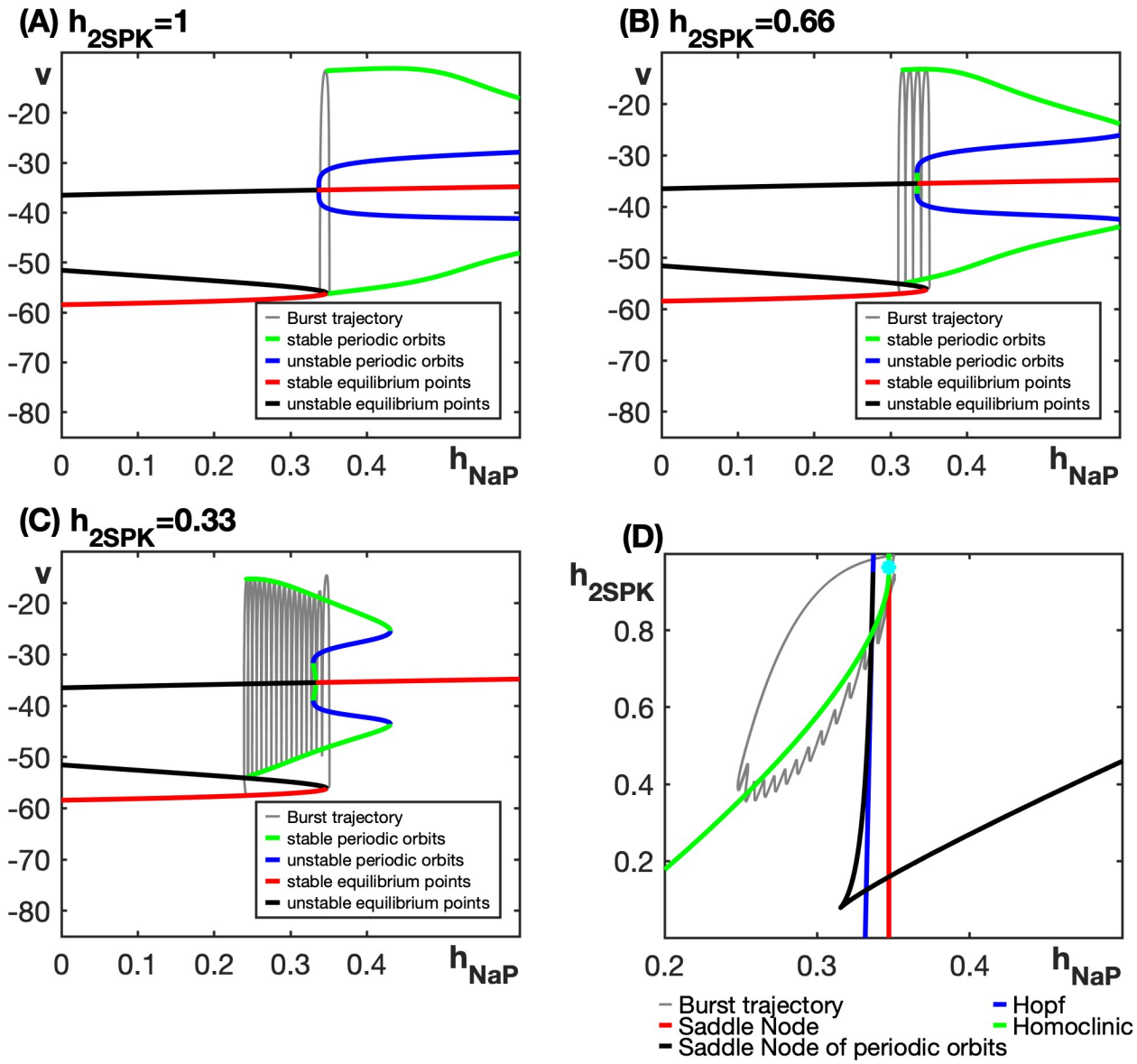

Figure 51: (A)-(C) Bifurcation diagrams of fast subsystem of the SPK model (22), (23) with respect to h_{NaP} for different values of h_{SPK}. (A) h_{SPK}=1 (B) $h_{SPK} = 0.66$ (C) $h_{SPK} = 0.33$ (D) The two-parameter bifurcation diagram of fast subsystem of the SPK model (22), (23) with respect to h_{NaP} and h_{SPK}.

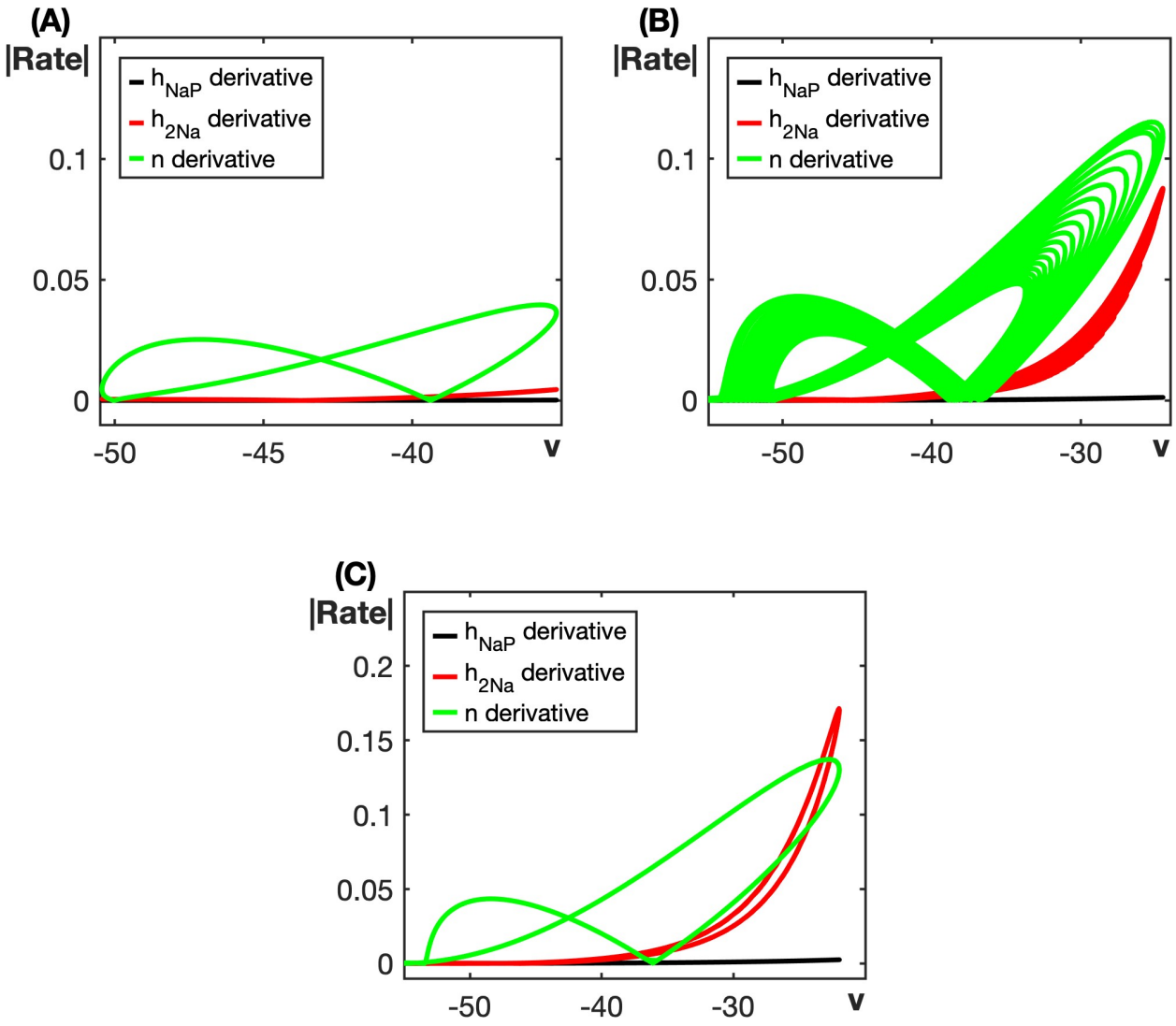

Figure 52: The absolute value of the derivatives of h_{NaP} (slowest variable), h_{2Na} and n (slowest variable among in the fast subsystem) in the DSPK model (24), (25) for different values of g_L (A) g_L=3.5 (B) g_L=4 (C) g_L=4.6

Bibliography

[1] A. P. Abdala, M. Dutschmann, J. M. Bissonnette, and Julian F. R. Paton. Correction of respiratory disorders in a mouse model of Rett syndrome. *Proceedings of the National Academy of Sciences*, 107(42):18208–18213, 2010.

[2] A. P. Abdala, M. A. Toward, M. Dutschmann, J. M. Bissonnette, and J. F. Paton. Deficiency of gabaergic synaptic inhibition in the kolliker-fuse area underlies respiratory dysrhythmia in a mouse model of rett syndrome. *J Physiol*, 594(1):223–37, 2016.

[3] M. U. Abdulla, R. S. Phillips, and J. E. Rubin. Dynamics of ramping bursts in a respiratory neuron model. *Journal of computational neuroscience*, 50(2):161–180, 2022.

[4] B. J. Bacak, J. Segaran, and Y. Molkov. Modeling the effects of extracellular potassium on bursting properties in pre-bötzinger complex neurons. *Journal of computational neuroscience*, 40(2):231–245, 2016.

[5] I. Bachmutsky, X. P. Wei, E. Kish, and K. Yackle. Opioids depress breathing through two small brainstem sites. *Elife*, 9:e52694, 2020.

[6] S. M. Baer, T. Erneux, and J. Rinzel. The slow passage through a Hopf bifurcation: Delay, memory effects, and resonance. *SIAM J. Appl. Math.*, 49(1):55–71, 1989.

[7] S. M. Baer and E. M. Gaekel. Slow acceleration and deacceleration through a Hopf bifurcation: power ramps, target nucleation, and elliptic bursting. *Phys. Rev. E*, 78, 2008.

[8] N. A. Baertsch and J. M. Ramirez. Insights into the dynamic control of breathing revealed through cell-type-specific responses to substance p. *Elife*, 8:e51350, 2019.

[9] W. H. Barnett, S. E. M. Jenkin, W. K. Milsom, J. F. R. Paton, A. P. Abdala, Y. I. Molkov, and D. B. Zoccal. The kölliker-fuse nucleus orchestrates the timing of expiratory abdominal nerve bursting. *Journal of neurophysiology*, 119(2):410–412, 2018.

[10] T. G. Bautista and M. Dutschmann. Inhibition of the pontine kolliker-fuse nucleus abolishes eupneic inspiratory hypoglossal motor discharge in rat. *Neuroscience*, 267:22–9, 2014.

[11] T. G. Bautista and M. Dutschmann. Ponto-medullary nuclei involved in the generation of sequential pharyngeal swallowing and concomitant protective laryngeal adduction in situ. *J Physiol*, 592(12):2605–23, 2014.

[12] T. G. Bautista, A. Y. Fong, and M. Dutschmann. Spontaneous swallowing occurs during autoresuscitation in the in situ brainstem preparation of rat. *Respir Physiol Neurobiol*, 202:35–43, 2014.

[13] R. Bertram, M. J. Butte, T. Kiemel, and A. Sherman. Topological and phenomenological classification of bursting oscillations. *Bulletin of Mathematical Biology*, 57(3):413–439, 1995.

[14] R. Bertram and J. E. Rubin. Multi-timescale systems and fast-slow analysis. *Mathematical Biosciences*, 287:105–121, 2017.

[15] S. Besnard, H. Khemiri, F. Masse, P. Denise, M. Verdaguer, and C. Gestreau. Differential respiratory control of the upper airway and diaphragm muscles induced by 5-ht1a receptor ligands. *Sleep breathing = Schlaf Atmung*, 16(1):135–147, 2012.

[16] A. L. Bianchi, M. Denavit-Saubié, and J. Champagnat. Central control of breathing in mammals: neuronal circuitry, membrane properties, and neurotransmitters. *Physiological Reviews*, 75(1):1–45, 1995.

[17] D. Bucher, G. Haspel, J. Golowasch, and F. Nadim. Central pattern generators. *eLS*, pages 1–12, 2015.

[18] R. J. Butera, J. Rinzel, and J. C. Smith. Models of respiratory rhythm generation in the pre-botzinger complex. i. bursting pacemaker neurons. *Journal of neurophysiology*, 82(1):382–397, 1999.

[19] R. R. Dhingra, T. E. Dick, W. I. Furuya, R. F. Galán, and M. Dutschmann. Volumetric mapping of the functional neuroanatomy of the respiratory network in the perfused brainstem preparation of rats. *The Journal of physiology*, 598(11):2061–2079, 2020.

[20] R. R. Dhingra, M. Dutschmann, and T. E. Dick. Blockade of dorsolateral pontine 5HT1A receptors destabilizes the respiratory rhythm in C57BL6/J wild-type mice. *Respiratory Physiology & Neurobiology*, 226:110–114, 2016. Brain and breathing.

[21] A. Dhooge, W. Govaerts, and Y. A. Kuznetsov. MATCONT: a MATLAB package for numerical bifurcation analysis of ODEs. *ACM Transactions on Mathematical Software (TOMS)*, 29(2):141–164, 2003.

[22] M. T. H. Do and B. P. Bean. Subthreshold sodium currents and pacemaking of subthalamic neurons: modulation by slow inactivation. *Neuron*, 39(1):109–120, 2003.

[23] F. Dumortier and R. Roussarie. Geometric singular perturbation theory beyond normal hyperbolicity. In Christopher K. R. T. Jones and Alexander I. Khibnik, editors, *Multiple-Time-Scale Dynamical Systems*, pages 29–63, New York, NY, 2001. Springer New York.

[24] M. Dutschmann and T. E. Dick. Pontine mechanisms of respiratory control. *Compr Physiol*, 2(4):2443–69, 2012.

[25] M. Dutschmann and H. Herbert. The kolliker-fuse nucleus gates the postinspiratory phase of the respiratory cycle to control inspiratory off-switch and upper airway resistance in rat. *European Journal of Neuroscience*, 24(4):1071–1084, 2006. 076TETimes Cited:30Cited References Count:64.

[26] R. Eckert and J. E. Chad. Inactivation of ca channels. *Progress in biophysics and molecular biology*, 44(3):215–267, 1984.

[27] B. Ermentrout. Type I membranes, phase resetting curves, and synchrony. *Neural Computation*, 8(5):979–1001, 1996.

[28] B. Ermentrout. *XPPAUT5.41 – the differential equations tool.* 2003.

[29] B. Ermentrout and D. H. Terman. *Mathematical Foundations of Neuroscience.* Interdisciplinary Applied Mathematics (IAM), Vol. 35. Springer, New York, NY, 2010.

[30] K. Ezure, I. Tanaka, and Y. Saito. Brainstem and spinal projections of augmenting expiratory neurons in the rat. *Neuroscience research*, 45(1):41–51, 2003.

[31] N. Fenichel. Geometric singular perturbation theory for ordinary differential equations. 31:53–98, 1979.

[32] K. C. Flor, W. H. Barnett, M. Karlen-Amarante, Y. I. Molkov, and D. B. Zoccal. Inhibitory control of active expiration by the botzinger complex in rats. *J Physiol*, 2020.

[33] A. Franci, G. Drion, and R. Sepulchre. Robust and tunable bursting requires slow positive feedback. *Journal of Neurophysiology*, 119(3):1222–1234, 2018.

[34] A. Franci, G. Drion, V. Seutin, and R. Sepulchre. A balance equation determines a switch in neuronal excitability. *PLoS Computational Biology*, 9(5):e1003040, 2013.

[35] M. L. Fung and W. M. St John. The functional expression of a pontine pneumotaxic centre in neonatal rats. *J Physiol*, 489 (Pt 2):579–91, 1995.

[36] S. P. Gaytán, F. Calero, P. A. Núñez-Abades, A. M. Morillo, and R. Pásaro. Pontomedullary efferent projections of the ventral respiratory neuronal subsets of the rat. *Brain research bulletin*, 42(4):323–334, 1997.

[37] J. C. Geerling, S. Yokota, I. Rukhadze, D. Roe, and N. L. Chamberlin. Kolliker-fuse gabaergic and glutamatergic neurons project to distinct targets. *J Comp Neurol*, 525(8):1844–1860, 2017.

[38] M.S. Goldman, J. Golowasch, E. Marder, and L.F. Abbott. Global structure, robustness, and modulation of neuronal models. *Journal of Neuroscience*, 21(4):5229–5238, 2001.

[39] M. Golubitsky, K. Josic, and T. J. Kaper. An unfolding theory approach to bursting in fast-slow systems. *Global analysis of dynamical systems*, pages 277–308, 2001.

[40] L. F. Hayward, M. Castellanos, and P. W. Davenport. Parabrachial neurons mediate dorsal periaqueductal gray evoked respiratory responses in the rat. *J Appl Physiol (1985)*, 96(3):1146–54, 2004.

[41] A. L. Hodgkin and A. F. Huxley. A quantitative description of membrane current and its application to conduction and excitation in nerve. *The Journal of Physiology*, 117(4):500–544, 1952.

[42] E. M. Izhikevich. Neural excitability, spiking and bursting. *International Journal of Bifurcation and Chaos*, 10(6):1171–1266, 2000.

[43] E. M. Izhikevich. *Dynamical systems in neuroscience*. MIT press, 2007.

[44] J. Jakus, I. Poliacek, E. Halasova, P. Murin, J. Knocikova, Z. Tomori, and D. C. Bolser. Brainstem circuitry of tracheal-bronchial cough: c-fos study in anesthetized cats. *Respir Physiol Neurobiol*, 160(3):289–300, 2008.

[45] S. E. M. Jenkin, W. K. Milsom, and D. B. Zoccal. The kölliker–fuse nucleus acts as a timekeeper for late-expiratory abdominal activity. *Neuroscience*, 348:63–72, 2017.

[46] C. K. R. T. Jones. *Geometric singular perturbation theory*, pages 44–118. Springer Berlin Heidelberg, Berlin, Heidelberg, 1995.

[47] L. A. E. Koolen. Effects of serotonin 1a receptor transmission on neural control of respiration, 6 2021.

[48] B. Krauskopf and H. M. Osinga. A codimension-four singularity with potential for action. In Bourama Toni, editor, *Mathematical Sciences with Multidisciplinary Applications*, pages 253–268, Cham, 2016. Springer International Publishing.

[49] L. Kubin, G. F. Alheid, E. J. Zuperku, and D. R. McCrimmon. Central pathways of pulmonary and lower airway vagal afferents. *Journal of applied physiology (Bethesda, Md. : 1985)*, 101(2):618–627, 2006.

[50] S. Kubota and J. E. Rubin. Nmda-induced burst firing in a model subthalamic nucleus neuron. *Journal of neurophysiology*, 106(2):527–537, 2011.

[51] E. S. Levitt, B. J. Hunnicutt, S. J. Knopp, J. T. Williams, and J. M. Bissonnette. A selective 5-ht1a receptor agonist improves respiration in a mouse model of rett syndrome. *Journal of Applied Physiology*, 115(11):1626–1633, 2013.

[52] A. H. Lewis and I. M. Raman. Resurgent current of voltage-gated na(+) channels. *The Journal of physiology*, 592(22):4825–4838, 2014.

[53] B. G. Lindsey, I. A. Rybak, and J. C. Smith. Computational models and emergent properties of respiratory neural networks. *Compr Physiol*, 2(3):1619–70, 2012.

[54] A. J. Loucif, G. L. Woodhall, U. S. Sehirli, and I. M. Stanford. Depolarisation and suppression of burst firing activity in the mouse subthalamic nucleus by dopamine d1/d5 receptor activation of a cyclic-nucleotide gated non-specific cation conductance. *Neuropharmacology*, 55(1):94–105, 2008.

[55] T. Manzke, M. Niebert, U. R. Koch, A. Caley, S. Vogelgesang, S. Hülsmann, E. Ponimaskin, U. Müller, T. G. Smart, R. J. Harvey, et al. Serotonin receptor 1a–modulated phosphorylation of glycine receptor α3 controls breathing in mice. *The Journal of Clinical Investigation*, 120(11):4118–4128, 2010.

[56] L. S. Milescu, B. P. Bean, and J. C. Smith. Isolation of somatic na+ currents by selective inactivation of axonal channels with a voltage prepulse. *The Journal of neuroscience : the official journal of the Society for Neuroscience*, 30(22):7740–7748, 2010.

[57] L. S. Milescu, T. Yamanishi, K. Ptak, and J. C. Smith. Kinetic properties and functional dynamics of sodium channels during repetitive spiking in a slow pacemaker neuron. *Journal of Neuroscience*, 30(36):12113–12127, 2010.

[58] Y. I. Molkov, B. J. Bacak, T. E. Dick, and I. A. Rybak. Control of breathing by interacting pontine and pulmonary feedback loops. *Front Neural Circuits*, 7:16, 2013.

[59] Y. I. Molkov, J. E. Rubin, I. A. Rybak, and J. C. Smith. Computational models of the neural control of breathing. *Wiley Interdiscip Rev Syst Biol Med*, 9(2), 2017.

[60] A. Montalbano, R. Corradetti, and B. Mlinar. Pharmacological characterization of 5-ht1a autoreceptor-coupled girk channels in rat dorsal raphe 5-ht neurons. *PloS one*, 10(10):e0140369, 2015.

[61] M. Mörschel and M. Dutschmann. Pontine respiratory activity involved in inspiratory/expiratory phase transition. *Philosophical Transactions of the Royal Society B: Biological Sciences*, 364(1529):2517–2526, 2009.

[62] A.I. Neishtadt. Persistence of stability loss for dynamical bifurcations. I. *Differ. Uravn.*, 23:2060–2067, 1987.

[63] A.I. Neishtadt. Persistence of stability loss for dynamical bifurcations. II. *Differ. Uravn.*, 24:226–233, 1988.

[64] Y. Oku and T. E. Dick. Phase resetting of the respiratory cycle before and after unilateral pontine lesion in cat. *J Appl Physiol (1985)*, 72(2):721–30, 1992.

[65] K. Otake, K. Ezure, J. Lipski, and R. B. Wong She. Projections from the commissural subnucleus of the nucleus of the solitary tract: an anterograde tracing study in the cat. *The Journal of comparative neurology*, 324(3):365–378, 1992.

[66] R. S Phillips, T. T. John, H. Koizumi, Y. I. Molkov, and J. C Smith. Biophysical mechanisms in the mammalian respiratory oscillator re-examined with a new data-driven computational model. *Elife*, 8:e41555, 2019.

[67] R. S. Phillips and J. E Rubin. Putting the theory into 'burstlet theory'with a biophysical model of burstlets and bursts in the respiratory prebötzinger complex. *Elife*, 11:e75713, 2022.

[68] J. L. Ransdell, J. D. Moreno, D. Bhagavan, J. R. Silva, and J. M. Nerbonne. Intrinsic mechanisms in the gating of resurgent na+ currents. *Elife*, 11:e70173, 2022.

[69] J. Rinzel. A formal classification of bursting mechanisms in excitable systems. *Proceedings of the International Congress of Mathematicians, Berkeley, California*, 1986.

[70] J. Rinzel and Y. S. Lee. On different mechanisms for membrane potential bursting, nonlinear oscillations in biology and chemistry (H. G. Othmer, editor). *Lecture Notes in Biomath., Springer-Verlag, New York*, 66(1):19–33, 1986.

[71] J. E. Rubin, B. J. Bacak, Y. I. Molkov, N. A. Shevtsova, J. C. Smith, and I. A. Rybak. Interacting oscillations in neural control of breathing: modeling and qualitative analysis. *Journal of computational neuroscience*, 30(3):607–632, 2011.

[72] J. E. Rubin, N. A. Shevtsova, G. B. Ermentrout, J. C. Smith, and I. A. Rybak. Multiple rhythmic states in a model of the respiratory central pattern generator. *Journal of neurophysiology*, 101(4):2146–2165, 2009.

[73] J. E. Rubin and J. C. Smith. Robustness of respiratory rhythm generation across dynamic regimes. *PLoS Computational Biology*, 15(7):e1006860, 2019.

[74] A. A. Sharp, F. K. Skinner, and E. Marder. Mechanisms of oscillation in dynamic clamp constructed two-cell half-center circuits. *Journal of Neurophysiology*, 76(2):867–883, 1996.

[75] N. A. Shevtsova, T. Manzke, Y. I. Molkov, A. Bischoff, J. C. Smith, I. A. Rybak, and D. W. Richter. Computational modelling of 5-ht receptor-mediated reorganization of the brainstem respiratory network. *Eur J Neurosci*, 34(8):1276–91, 2011.

[76] R. G. Shulman, D. L. Rothman, K. L. Behar, and F Hyder. Energetic basis of brain activity: implications for neuroimaging. *Trends in neurosciences*, 27(8):489–495, 2004.

[77] J. N. Silva, E. V. Lucena, T. M. Silva, R. S. Damasceno, A. C. Takakura, and T. S. Moreira. Inhibition of the pontine kolliker-fuse nucleus reduces genioglossal activity elicited by stimulation of the retrotrapezoid chemoreceptor neurons. *Neuroscience*, 328:9–21, 2016.

[78] J. C. Smith, A. P. Abdala, A. Borgmann, I. A. Rybak, and J. F. Paton. Brainstem respiratory networks: building blocks and microcircuits. *Trends in neurosciences*, 36(3):152–162, 2013.

[79] J. C. Smith, A. P. Abdala, H. Koizumi, I. A. Rybak, and J. F. Paton. Spatial and functional architecture of the mammalian brain stem respiratory network: a hierarchy of three oscillatory mechanisms. *J Neurophysiol*, 98(6):3370–87, 2007.

[80] L. Sokoloff. Energetics of functional activation in neural tissues. *Neurochemical research*, 24(2):321–329, 1999.

[81] C. Städele and W. Stein. Neuromodulation enables temperature robustness and coupling between fast and slow oscillator circuits. *Frontiers in cellular neuroscience*, 16:849160, 2022.

[82] G. M. Stettner, P. Huppke, C. Brendel, D. W. Richter, J. Gärtner, and M. Dutschmann. Breathing dysfunctions associated with impaired control of postinspiratory activity in mecp2-/y knockout mice. *The Journal of physiology*, 579(Pt 3):863–876, 2007.

[83] J. Tabak, J. Rinzel, and R. Bertram. Quantifying the relative contributions of divisive and subtractive feedback to rhythm generation. *PLoS Computational Biology*, 7(4):e1001124, 2011.

[84] J. Tabak, N. Toporikova, M. E. Freeman, and R. Bertram. Low dose of dopamine may stimulate prolactin secretion by increasing fast potassium currents. *J Comput Neurosci.*, 22(2):211–22, 2007.

[85] W. Teka, J. Tabak, T. Vo, M. Wechselberger, and R. Bertram. The dynamics underlying pseudo-plateau bursting in a pituitary cell model. *J. Math. Neurosc.*, 1(12), 2011.

[86] W. Teka, K. Tsaneva-Atanasova, R. Bertram, and J. Tabak. From plateau to pseudo-plateau bursting: Making the transition. *Bull Math. Biol.*, 73(6):1292–1311, 2011.

[87] A. K. Tryba, F. Peña, and J. M. Ramirez. Stabilization of bursting in respiratory pacemaker neurons. *The Journal of neuroscience : the official journal of the Society for Neuroscience*, 23(8):3538–3546, 2003.

[88] K. Tsaneva-Atanasova, H. M. Osinga, T. Rie, and A. Sherman. Full system bifurcation analysis of endocrine bursting models. *J Theor Biol.*, 264(4):1133–1146, 2010.

[89] K. Tsaneva-Atanasova, H. M. Osinga, T. Rie, and A. Sherman. Cross-currents between biology and mathematics: The codimension of pseudo-plateau bursting. *Discrete Contin. Dyn. Syst. Ser. A.*, 32(8):2853–2877, 2012.

[90] A. G. Varga, S. N. Maletz, J. T. Bateman, B. T. Reid, and E. S. Levitt. Neurochemistry of the kolliker-fuse nucleus from a respiratory perspective. *J Neurochem*, 2020.

[91] T. Vo, R. Bertram, and M. Wechselberger. Multiple geometric viewpoints of mixed mode dynamics associated with pseudo-plateau bursting. *SIAM Journal on Applied Dynamical Systems*, 12(2):789–830, 2013.

[92] T. Vo, J. Tabak, R. Bertram, and M. Wechselberger. A geometric understanding of how fast activating potassium channels promote bursting in pituitary cells. *Journal of Computational Neuroscience*, 36(2):259–278, 2014.

[93] N. Voituron, C. Menuet, M. Dutschmann, and G. Hilaire. Physiological definition of upper airway obstructions in mouse model for rett syndrome. *Respiratory physiology neurobiology*, 173(2):146–156, 2010.

[94] M. Wechselberger. *Geometric Singular Perturbation Theory Beyond the Standard Form*. Frontiers in Applied Dynamical Systems: Reviews and Tutorials, Vol. 6., Springer Cham, Springer Nature Switzerland AG., 2020.

[95] S. Wittman, A. P. Abdala, and J. E. Rubin. Reduced computational modelling of Kölliker-Fuse contributions to breathing patterns in Rett syndrome. *The Journal of Physiology*, 597(10):2651–2672, 2019.

[96] J. F. Zhang, P. T. Ellinor, R. W. Aldrich, and R. W. Tsien. Molecular determinants of voltage-dependent inactivation in calcium channels. *Nature*, 372(6501):97–100, 1994.